Theoretical Studies of Ultracold Dipolar Molecules

by

Brendan Patrick Abolins

A dissertation submitted in partial satisfaction of the
requirements for the degree of
Doctor of Philosophy

in

Chemistry

in the

Graduate Division

of the

University of California, Berkeley

Committee in charge:

Professor K. Birgitta Whaley, Chair
Professor William H. Miller
Professor Dmitry Budker

Fall 2014

Theoretical Studies of Ultracold Dipolar Molecules

Abstract

Theoretical Studies of Ultracold Dipolar Molecules

by

Brendan Patrick Abolins

Doctor of Philosophy in Chemistry

University of California, Berkeley

Professor K. Birgitta Whaley, Chair

Strongly interacting ultracold dipolar molecules are a rich platform for quantum information and quantum simulation of phenomena relevant to condensed matter systems. This dissertation presents novel theoretical and computational studies of ultracold dipolar molecules relevant to these areas in three broad categories.

First, the path integral ground state quantum Monte Carlo method is extended to simulations with both translational and rotational degrees of freedom, including the development of a novel estimator of the elementary excitation energies of a system with these degrees of freedom based on the well known Feynman-Bijl approximation. This is then used to study dipolar molecular ensembles confined to one-dimensional optical lattices. The ground state phase diagram is characterized with both a mean-field method and the aforementioned quantum Monte Carlo method. A quantum phase transition is found for very short optical lattice spacings or very large dipole moments. The prospects for experimentally realizing a system which exhibits this phase transition are discussed.

Second, the path integral ground state quantum Monte Carlo method is utilized to study the ground state of dipole molecules confined to two-dimensional optical lattices. On square lattices a crossover from a weakly interacting disordered phase to a strongly interacting striped phase is found for short lattice spacings or large dipole moments. On triangular lattices a crossover between a disordered phase and a completely polarized phase is found, also for short lattice spacings or large dipole moments. The relevance of such simulations to self-assembled dipolar crystals in two dimensions is discussed and simulation results of these systems are presented. Simulations of polarized and harmonically confined molecular systems in two dimensions with translations and rotations are also presented and a realistic interaction potential using highly accurate *ab initio* quantum chemistry techniques is calculated for LiH–LiH interactions as a preliminary step toward developing a high quality trial wave function for the simulation of systems possessing both translational and rotational degrees of freedom.

Finally, several novel applications for dipolar molecules confined to optical lattices are proposed. An experimental realization of a topological phase using $^2\Sigma$ ground state molecules with applied near resonant microwave fields and transverse magnetic fields is proposed. A

method to create an array of dipole-coupled two-level molecules exhibiting superradiance and possessing novel spectroscopic properties using $^1\Sigma$ ground state molecules in the combination of a far off-resonant laser field and a moderate magnetic field is proposed. Additionally, a method to create entangled pairs of molecules using closed-shell dipolar molecules immersed in an intense far off-resonant laser field is reviewed and an extension in which parallel optical lattices are merged and molecules are allowed to collide in the presence of a far off-resonant laser field is proposed. Simulation results are presented indicating that a significant amount of entanglement may be generated in such a way in realistic molecular systems.

To my grandfather, Thomas “Les” Van Zandt,

Whose example inspired me and whose love and support made this possible.

Contents

List of Figures

Acknowledgments

There are numerous people need to thank for their help and support. This work would not have been possible without the guidance of my research advisor, K. Birgitta Whaley, with whom I feel very fortunate to have worked with. Always encouraging and with helpful advice, she made this work much easier than it otherwise would have been. Robert Zillich was also instrumental in my course of study, I would not know most of what I learned about quantum Monte Carlo without his instruction, advice, and examples. He practically served as my second adviser, even from another continent, and for this I am grateful. I'd like to thank the Austrian Marshall Plan Foundation for a Marshall Plan Scholarship to study at Johannes Kepler Universität Linz, in Linz, Austria during the 2009 — 2010 school year, which made academic collaboration with Robert Zillich that much easier.

The members of the Whaley group during my time here at Berkeley deserve recognition as well. They were great office mates and group mates and provided interesting and useful conversation and were a source of research ideas. In particular I have to thank Joel Corbo, with whom I had many an enlightening conversation on the topics of science and education and who helped me develop my own teaching philosophy. I also have to thank Chris Herdman and Loren Greenman, who provided invaluable guidance on any number of topics in Monte Carlo studies and computational science. I am thankful to have worked with Daniel Freeman, for all his helpful office conversations. Thanks goes to Felipe Herrera for many helpful discussions about the physics of molecules in intense laser fields. Special thanks go to Diana Hufnagl for many helpful discussions, as well as for being an overall great officemate, making my time in Linz much better than it would have otherwise been. Thanks goes to Sergei Alyabyshev for a great many useful conversations about ultracold polar molecules. Special thanks goes to Sally Jeon and Christiaan Khurana for their eagerness to learn.

In addition I have to thank my classmates, without whom I would have had a much harder time getting through those first years of graduate school. In particular I must thank Adam Hill, in particular, for all of the stimulating and enlightening lunch hour conversations we had. I am eternally grateful for the love, support, and encouragement of Allison Pymer, without which graduate school would have seemed nearly impossible.

I would be remiss if I did not thank my professors, undergraduate advisers, and peers while I attended Western Washington University. In particular, thanks goes to Gary Lampman, who put the idea of pursuing a Ph.D. in my head. Christopher Daley deserves special recognition for giving me my first taste of life in an academic research laboratory, teaching me a great deal about chemical synthesis, and further encouraging me to pursue an advanced degree. Special thanks goes to Elizabeth "Betsy" Raymond, for being such a great mentor and encouraging me during a very rough year at WWU, and for exposing me to the wonders of quantum mechanics. Special recognition also goes to Dustin Titus for being the best study partner through a difficult year of physical chemistry and even better friend above and beyond that.

Finally, I need to thank all of my family and friends throughout the journey, without whom this would ultimately never have happened. My loving parents, Alice and Karlis

Abolins, and grandparents, Les and Patty Van Zandt, especially deserve recognition for always loving me and encouraging me to go further. They always supported me through all of my endeavors be it emotionally, intellectually, or financially. Without my mother or grandfather's example as professional chemists I probably would have never thought to study chemistry. Thanks goes to my brother, Devin Abolins, for always being there and giving me a reason to achieve, for being a terrific source of inspiration, and for being the all-around coolest little brother possible. I couldn't have possibly hoped for a better family and extended family and I would not have been able to write this without their influence, love, and support.

Chapter 1

Introduction

The molecular physics of ultracold samples of heteronuclear diatomic molecules is currently one of the most exciting fields of study in chemical physics [1]. The discoveries being made in this field have far reaching consequences – from how we understand the laws of nature, all the way to how we solve complex computational problems. This is all made possible because of the way in which these molecules, which possess a permanent electric dipole moment, interact with each other via the dipole-dipole interaction potential [2]

$$V_{\rm dd}(\boldsymbol{\mu}_1, \boldsymbol{\mu}_2, \mathbf{r}) = \frac{1}{4\pi\epsilon_0}\left(\frac{\boldsymbol{\mu}_1 \cdot \boldsymbol{\mu}_2}{r^3} - \frac{3(\boldsymbol{\mu}_1 \cdot \mathbf{r})(\boldsymbol{\mu}_2 \cdot \mathbf{r})}{r^5}\right). \tag{1.1}$$

Here $\boldsymbol{\mu}_i$ is the electric dipole moment of molecule i and $\mathbf{r}$ is the intermolecular separation vector connecting the centers of mass of the two interacting molecules, as well as with external electric and magnetic fields. The dipole-dipole interaction potential is relatively long-ranged, as compared to ultracold atomic systems that interact via relatively short ranged van der Waals interactions [1] which vary with distance as $1/r^6$. Especially important is the way in which the careful application of external electric and magnetic fields can modify the interactions between polar molecules [3, 4].

Assuming the intermolecular separation vector, $\mathbf{r}$, lies along the z-axis and expressing the directions of the dipole orientations in spherical polar coordinates, shown in figure 1, eq. (1.1) can also be written as

$$V_{\rm dd}(r, \theta_A, \theta_B, \phi) = -\frac{\mu^2}{4\pi\epsilon_0 r^3}(2\cos\theta_A\cos\theta_B - \sin\theta_A\sin\theta_B\cos\phi), \tag{1.2}$$

where $\phi = \phi_A - \phi_B$ is the dihedral angle between the two orientations. Examining plots of the dipole-dipole potential (see, *e.g.*, figures 1 and 1) at a fixed distance for a variety of relative orientations reveals another salient feature of this interaction potential, namely that it is strongly anisotropic. In figure 1 $V_{\rm dd}(r, \theta_A, \theta_B, \phi)$ is plotted against θ_A and ϕ, for $\theta_B = \pi/2$. This reveals that when both molecules are aligned perpendicular to the intermolecular axis (figure 1 (a)), the potential is attractive when they are oriented anti-parallel to one another, and repulsive when they are oriented parallel to one another. Figure 1

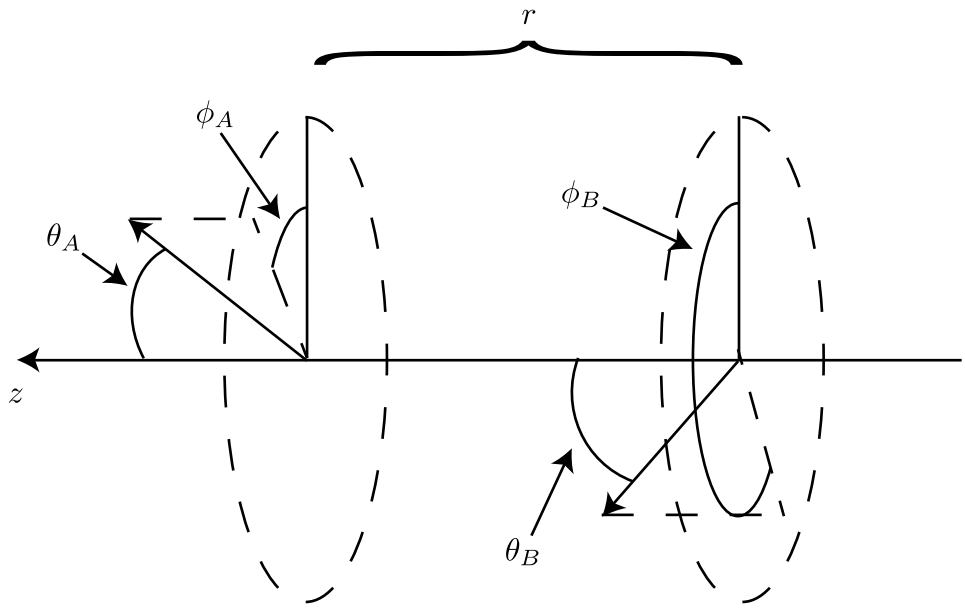

Figure 1.1: The coordinates of a pair of dipoles in spherical polar coordinates with the intermolecular axis along the z-axis.

shows $V_{\rm dd}(r, \theta_A, \theta_B, \phi)$ plotted against θ_A and θ_B, for $\phi = 0$ (top panel) and $\phi = \pi/2$ (bottom panel). From this figure it is evident that the global potential minimum (at fixed r) occurs when both molecules are parallel to the intermolecular axis and to each other, the "tip-to-tail" configuration (figure 1 (b)). When both dipoles are aligned with the intermolecular axis but oriented anti-parallel to one another represents the global potential energy maximum, at a fixed r. It is this anisotropy that allows a one dimensional system of dipoles to exhibit an order-disorder phase transition, explored in chapter 5. The anisotropy of the dipole-dipole interaction potential also plays a defining role in the types of orderings considered in two dimensional lattice systems, discussed in chapter 6.

On the fundamental physics end, polar molecules have been used to make incredibly sensitive measurements to put a bound on the magnitude of the electron electric dipole moment [5–7], helping to rule out models of physics beyond the standard model of particle physics using tabletop experiments rather than large particle colliders. Recent progress in cooling polar molecules to the millikelvin temperature regime and below [8, 9] have the potential to push these limits further, as well as to make possible other measurements of novel physical phenomena such as the variation of fundamental physical constants [10, 11]. In addition, polar molecules confined to optical lattices have been proposed as a platform for the simulation of phenomena relevant to condensed matter systems [3, 12–25], providing a route to study models of superconductivity and energy transfer, among other topics, in a

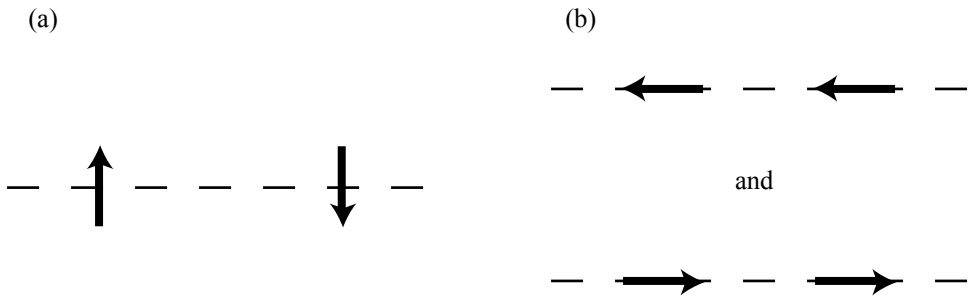

Figure 1.2: The important low energy configurations of a pair of dipoles. On the left, (a) a local minimum of the dipole-dipole potential in eq. (1.1) when $\theta_A = \theta_B = \pi/2$ and $\phi = \pi$ (see figure 1), and on the right (b) the two degenerate global minima when $\theta_A = \theta_B = 0$ (top) and $\theta_A = \theta_B = \pi$ (bottom), connected via inversion through the origin centered at the center of the two dipoles, of the dipole-dipole potential.

highly controllable way.

Quantum information processing is another field in which polar molecules trapped in optical lattices are poised to make an impact. Once again it is the tunability and extended range of the interactions, as well as the way in which molecular properties can be manipulated with external fields, that makes polar molecules an enticing platform for quantum information [1]. Interactions with external electric fields can provide single-site addressability in optical lattices [26], important for modification of the the state of individual qubits, and the dipole-dipole interaction can be used to generate entanglement between multiple molecules [27–31]. Progress toward the simulation of topological phases with dipolar molecules [17, 24] may even lead to the realization of topologically protected qubits [32] which are naturally resilient to local noise and experimental imperfections.

In the majority of these cases it is the molecular dipole moment, and the relatively strong, long ranged, and anisotropic interactions which this enables, which makes diatomic molecules enticing objects of study. This is the key theme that is developed throughout this dissertation.

1.1 Overview

The remainder of this dissertation is organized into three main sections. The first section includes chapters 2, 3 and 4 and describes the theoretical underpinnings of the rest of the dissertation. Chapter 2 is a discussion of selected topics in the physics of polar diatomic molecules, in particular an overview of the rigid rotor approximation for the rotations of molecules and the interactions of polar molecules with far off resonant laser fields. Chapter 3

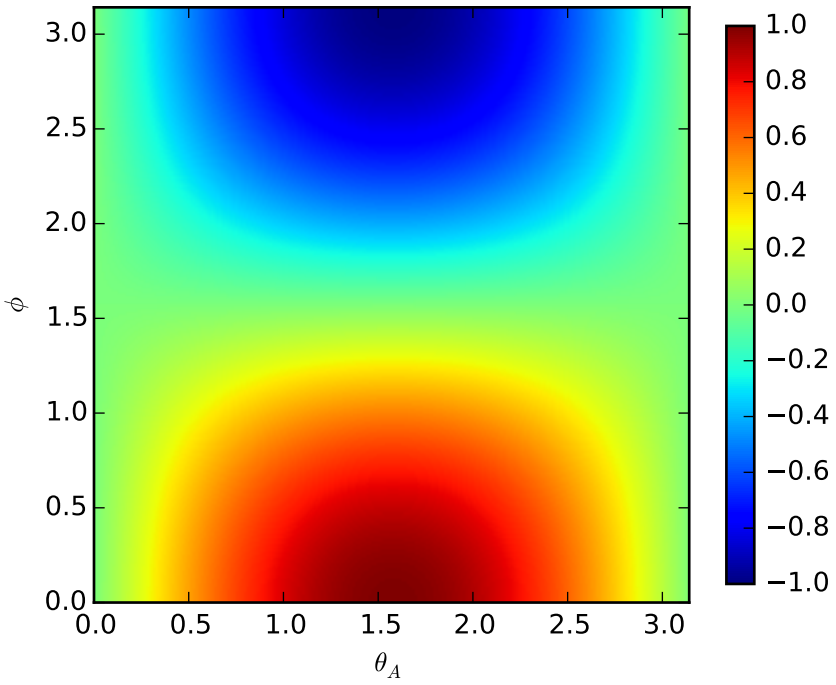

Figure 1.3: The dipole-dipole potential in eq. (1.2) plotted as a function of θ_A and ϕ for $\theta_B = \pi/2$. The attractive lobe at $\theta_A = \pi/2$ and $\phi = \pi$ is a local minimum at fixed r, corresponding to an configuration where both polar molecules are oriented perpendicular to the z-axis and anti-parallel to one another, shown in figure 1 (a).

contains an overview of the path integral ground state quantum Monte Carlo (PIGS) method and its extension to ensembles of polar molecules. Chapter 4 contains a brief derivation of an extension of the well-known Feynman-Bijl approximation to the elementary excitation spectrum [33, 34] of dipolar fluids with rotational degrees of freedom.

The second section is composed of chapters 5 and 6 and describes the study of the phase diagram of polar diatomic molecules confined to deep optical lattices in one and two spatial dimensions, as well as preliminary studies of dipolar systems without such confinement, using a PIGS code for simultaneously rotating and translating molecules that has been developed by the author. The final section is entirely contained in the final chapter, chapter 7, and describes miscellaneous work on proposals for quantum simulation and quantum information

processing using polar diatomic molecules.

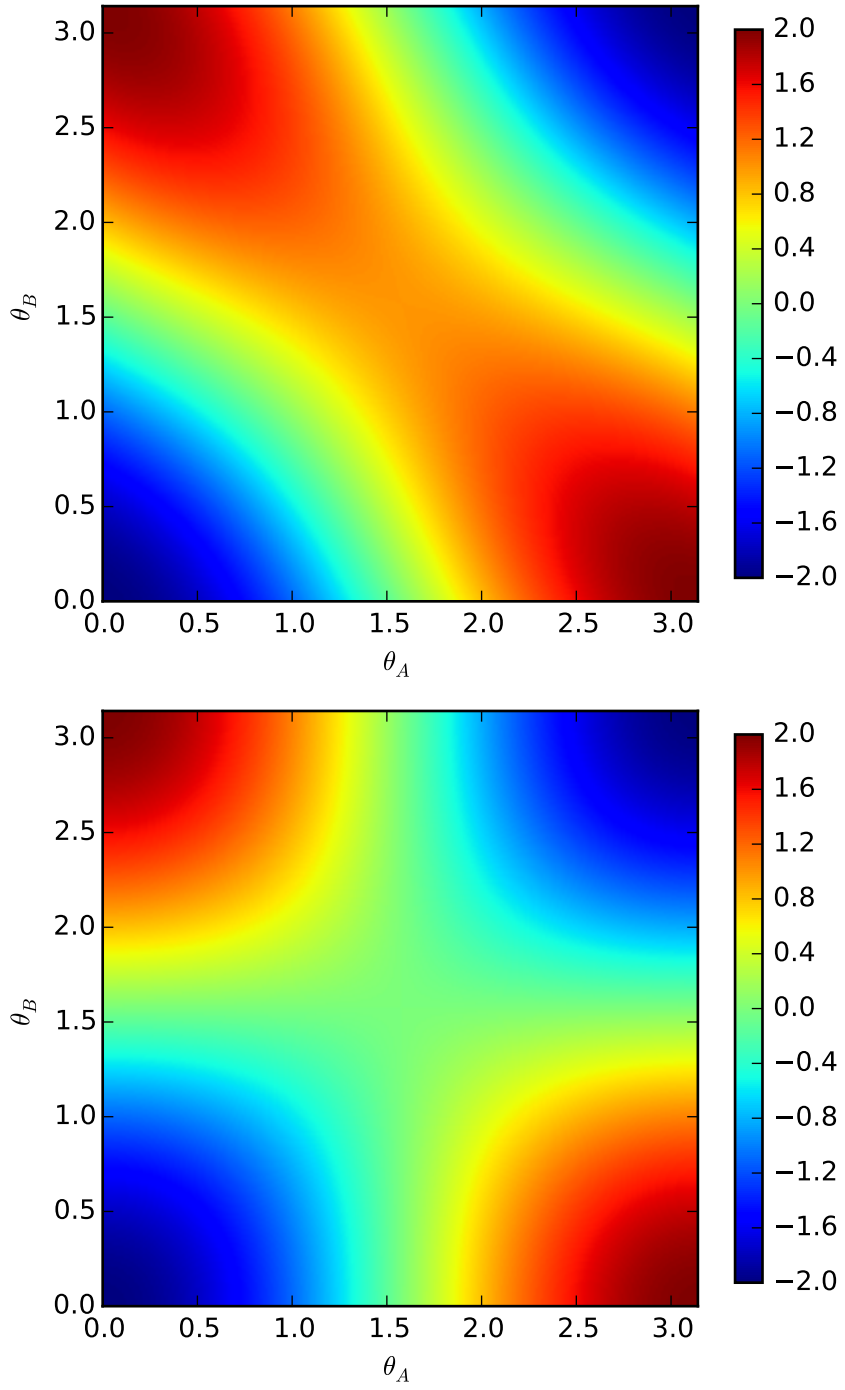

Figure 1.4: The dipole-dipole potential in eq. (1.2) plotted as a function of θ_A and θ_B for $\phi = 0$ (top panel) and $\phi = \pi/2$ (bottom panel). Both panels exhibit the same minima, the degenerate global minima of the dipole-dipole potential when $\theta_A = \theta_B = 0$ and $\theta_A = \theta_B = \pi$, corresponding to the situation where the orientations of both molecular dipoles are parallel to the intermolecular axis, depicted in figure 1 (b).

Chapter 2

Physics of diatomic molecules

2.1 The molecular Hamiltonian

The Hamiltonian for a closed shell diatomic molecule, neglecting spin, is

$$\begin{aligned} H = &\sum_{A=1}^{2} \frac{\mathbf{P}_A^2}{2M_A} + \sum_{i=1}^{n} \frac{\mathbf{p}_i^2}{2m_e} \\ &- \sum_{A,i} \frac{Z_A e^2}{4\pi\epsilon_0 |\mathbf{R}_A - \mathbf{r}_i|} + \sum_{B<A} \frac{Z_A Z_B e^2}{4\pi\epsilon_0 |\mathbf{R}_A - \mathbf{R}_B|} + \sum_{j<i} \frac{e^2}{4\pi\epsilon_0 |\mathbf{r}_i - \mathbf{r}_j|} \qquad (2.1) \\ = &\, T_n + T_e + V_{en} + V_{nn} + V_{ee}, \qquad (2.2) \end{aligned}$$

where $\mathbf{P}_A$, $\mathbf{R}_A$, M_A, and Z_A are the momentum, position, mass, and nuclear charge of the Ath nucleus and $\mathbf{p}_i$ and $\mathbf{r}_i$ are the momentum and position of the ith electron. To treat this problem completely rigorously would require treating the motion of the nuclei and the motion of the electrons on equal footing, but for present purposes this represents unnecessary effort as there exists a natural separation of energy scales for nuclear and electronic motion stemming from the fact that $M_A \gg m_e$. By utilizing this fact and neglecting the nuclear kinetic energy, essentially neglecting nuclear motion, one arrives at an approximate Hamiltonian for the electronic degrees of freedom only

$$\begin{aligned} H_{\text{elec}} = &\sum_{i=1}^{n} \frac{\mathbf{p}_i^2}{2m_e} - \sum_{A,i} \frac{Z_A e^2}{4\pi\epsilon_0 |\mathbf{R}_A - \mathbf{r}_i|} + \sum_{B<A} \frac{Z_A Z_B e^2}{4\pi\epsilon_0 |\mathbf{R}_A - \mathbf{R}_B|} + \sum_{j<i} \frac{e^2}{4\pi\epsilon_0 |\mathbf{r}_i - \mathbf{r}_j|} \qquad (2.3) \\ = &\, T_{\text{e}} + V_{en} + V_{nn} + V_{ee}, \qquad (2.4) \end{aligned}$$

in which the positions of the nuclei are considered to be parameters. Within this approximation the eigenstates and energies of Hamiltonian (2.4) are given by

$$H_{\text{elec}}(\mathbf{R}_1, \mathbf{R}_2)\Phi_i(\mathbf{r}_1, \ldots, \mathbf{r}_n; \mathbf{R}_1, \mathbf{R}_2) = U_i(\mathbf{R}_1, \mathbf{R}_2)\Phi_i(\mathbf{r}_1, \ldots, \mathbf{r}_n; \mathbf{R}_1, \mathbf{R}_2), \qquad (2.5)$$

where the energies and states depend parametrically on the positions of the nuclei.

Formally, the eigenstates of Hamiltonian (2.2) can be written in the form

$$\Psi_i(\mathbf{R}_1, \mathbf{R}_2, \mathbf{r}_1, \ldots, \mathbf{r}_n) = \sum_{k=1}^{\infty} X_k(\mathbf{R}_1, \mathbf{R}_2)\Phi_k(\mathbf{r}_1, \ldots, \mathbf{r}_n; \mathbf{R}_1, \mathbf{R}_2). \tag{2.6}$$

Invoking the Born-Oppenheimer approximation [35] amounts to assuming that the states, assuming non-degenerate electronic energies, may be approximated as

$$\Psi_i(\mathbf{R}_1, \mathbf{R}_2, \mathbf{r}_1, \ldots, \mathbf{r}_n) \approx X_k(\mathbf{R}_1, \mathbf{R}_2)\Phi_k(\mathbf{r}_1, \ldots, \mathbf{r}_n; \mathbf{R}_1, \mathbf{R}_2), \tag{2.7}$$

a simple product of a nuclear wave function and an electronic wave function. Under the Born-Oppenheimer approximation the nuclear wave functions satisfy an approximate Schrödinger equation

$$H_{\text{nuc}}X_i(\mathbf{R}_1, \mathbf{R}_2) = [T_n + U_i(\mathbf{R}_1, \mathbf{R}_2)]\, X_i(\mathbf{R}_1, \mathbf{R}_2) = E_i X_i(\mathbf{R}_1, \mathbf{R}_2) \tag{2.8}$$

showing that under this approximation the electronic energies constitute a potential energy surface governing the nuclear motion.

2.2 The rigid rotor-harmonic oscillator approximation

Further simplification can be obtained by making the rigid rotor-harmonic oscillator approximation. In the absence of external fields the potential U_i depends only on the distance between the nuclei and not their absolute positions. This lends itself to transforming the problem to one that depends not on $\mathbf{R}_1$ and $\mathbf{R}_2$ but on the relative coordinates, $\mathbf{r}_{\text{rel}} = \mathbf{R}_1 - \mathbf{R}_2$, and the coordinates of the center of mass, $\mathbf{R}_{\text{cm}} = (M_1/M)\mathbf{R}_1 + (M_2/M)\mathbf{R}_2$ with the total molecular mass $M = M_1 + M_2$. The corresponding momenta can be found as they are in classical mechanics, $\mathbf{P}_{\text{cm}} = \mathbf{P}_1 + \mathbf{P}_2$ and $\mathbf{p}_{\text{rel}} = (M_2/M)\mathbf{P}_1 - (M_1/M)\mathbf{P}_2$ so that the transformed Hamiltonian (2.8) is

$$\left[\frac{\mathbf{P}_{\text{cm}}^2}{2M} + \frac{\mathbf{p}_{\text{rel}}^2}{2\mu} + U_i(\mathbf{r}_{\text{rel}})\right] X_i(\mathbf{R}_{\text{cm}}, \mathbf{r}_{\text{rel}}) = E_i X_i(\mathbf{R}_{\text{cm}}, \mathbf{r}_{\text{rel}}), \tag{2.9}$$

where $\mu = M_1M_2/M$ is the reduced mass. Since the potential only depends on the relative coordinates, this Hamiltonian can then be split into a Hamiltonian for the center of mass motion only and the relative motion only, *i.e.* $H_{\text{nuc}} = H_{\text{cm}} + H_{\text{rel}}$, with

$$H_{\text{cm}} = \frac{\mathbf{P}_{\text{cm}}^2}{2M}, \tag{2.10}$$

$$H_{\text{rel}} = \frac{\mathbf{p}_{\text{rel}}^2}{2\mu} + U_i(\mathbf{r}_{\text{rel}}). \tag{2.11}$$

Focusing on the relative coordinates and in the absence of external fields, the relative Hamiltonian can be further simplified by realizing that the potential only depends on the

magnitude of the distance between the nuclei and not on their orientations. Since the Hamiltonian (2.11) in the center of mass frame is obviously symmetric under arbitrary rotations, it is most convenient to proceed in spherical polar coordinates

$$x_{\rm rel} = r\cos\phi\sin\theta, \tag{2.12}$$
$$y_{\rm rel} = r\sin\phi\sin\theta, \tag{2.13}$$
$$z_{\rm rel} = r\cos\theta, \tag{2.14}$$

with $r = |\mathbf{r}_{\rm rel}|$. In these coordinates Hamiltonian (2.11) is

$$\begin{aligned} H_{\rm rel} &= -\frac{\hbar^2}{2\mu}\left(\frac{1}{r^2}\frac{\partial}{\partial r}r^2\frac{\partial}{\partial r} + \frac{1}{r^2\sin\theta}\frac{\partial}{\partial\theta}\sin\theta\frac{\partial}{\partial\theta} + \frac{1}{r^2\sin^2\theta}\frac{\partial^2}{\partial\phi^2}\right) + U_i(r) \\ &= -\frac{\hbar^2}{2\mu r^2}\left(\frac{\partial}{\partial r}r^2\frac{\partial}{\partial r} + \mathbf{L}^2\right) + U_i(r), \end{aligned} \tag{2.15}$$

where $\mathbf{L}$ is the angular momentum operator. The form of eq. (2.15) is instantly recognizable as that of a particle in a central potential and is separable into an angular and radial portions. The eigenstates of eq. (2.15) can be written in the form $\psi_{ijlm}(r,\theta,\phi) = (\chi_{ijl}(r)/r)Y_l^m(\theta,\phi)$, where $\chi_{ijl}(r)$ satisfies the radial Schrödinger equation

$$\left[-\frac{\hbar^2}{2\mu}\frac{\partial^2}{\partial r^2} + \frac{\hbar^2}{2\mu}\frac{l(l+1)}{r^2} + U_i(r)\right]\chi_{ijl}(r) = E_{ijl}\chi_{ijl}(r). \tag{2.16}$$

In order to proceed it is convenient to expand the potential $U_i(r)$ in a power series about the potential minimum, $r_{{\rm eq},i}$, as

$$U_i(r) = U_i(r_{{\rm eq},i}) + U_i'(r_{{\rm eq},i})(r - r_{{\rm eq},i}) + \frac{1}{2}U_i''(r_{{\rm eq},i})(r - r_{{\rm eq},i})^2 + O(r^3), \tag{2.17}$$

where $U_i'(r_{{\rm eq},i}) = 0$ at the equilibrium distance. The expansion above truncated to second order generally suffices for potentials that are not strongly anharmonic and so the radial Schrödinger equation in eq. (2.16) can be approximated well by

$$\left[-\frac{\hbar^2}{2\mu}\frac{\partial^2}{\partial r^2} + \frac{\hbar^2}{2\mu}\frac{l(l+1)}{r^2} + \frac{1}{2}k_i(r - r_{{\rm eq},i})^2\right]\chi_{ijl}(r) = (E_{ijl} - U_i(r_{{\rm eq},i}))\chi_{ijl}(r), \tag{2.18}$$

where $k_i = U_i''(r_{{\rm eq},i})$ can be identified as the spring constant, through which it is possible to define the vibrational frequency, $\omega_i = \sqrt{k_i/\mu}$. For a typical molecule the rotational frequency $h/(\mu r_{{\rm eq},i}^2) \ll \omega_i$ and so over the time scale of a single rotational period the molecule will undergo very many vibrations about the equilibrium displacement, $r_{{\rm eq},i}$, and to a first approximation in the rotational kinetic energy term r can then be replaced with the equilibrium value. The resulting Hamiltonian is that of the simple one-dimensional harmonic oscillator

$$\left[-\frac{\hbar^2}{2\mu}\frac{\partial^2}{\partial r^2} + \frac{1}{2}\mu\omega_i^2(r - r_{{\rm eq},i})^2\right]\chi_{{\rm vib},in}(r) = E_{{\rm vib},in}\chi_{{\rm vib},in}(r), \tag{2.19}$$

with $E_{\mathrm{vib},in} = E_{inl} - U_i(r_{\mathrm{eq},i}) - hB_i l(l+1) = \hbar\omega_i(n+1/2)$ and $hB_i = \hbar^2/(2\mu r_{\mathrm{eq},i}^2) = \hbar^2/(2I_i)$. Under these approximations, which constitute the rigid rotor-harmonic oscillator approximation, the Hamiltonian for the nuclear coordinates in a particular electronic state may be written as

$$H_{\mathrm{nuc}} = H_{\mathrm{rot}} + H_{\mathrm{vib}} = \frac{\mathbf{L}^2}{2I} + \left(\frac{p^2}{2\mu} + \frac{1}{2}\mu\omega^2 r^2\right), \tag{2.20}$$

where H_{rot} is the usual rigid rotor Hamiltonian with eigenstates

$$H_{\mathrm{rot}}|lm\rangle = \frac{\mathbf{L}^2}{2I}|lm\rangle = hBl(l+1)|lm\rangle \tag{2.21}$$

and H_{vib} is the usual harmonic oscillator Hamiltonian with corresponding eigenstates

$$H_{\mathrm{vib}}|n\rangle = \left(\frac{p^2}{2\mu} + \frac{1}{2}\mu\omega^2 r^2\right)|n\rangle = \hbar\omega\left(n+\frac{1}{2}\right)|n\rangle. \tag{2.22}$$

The eigenstates of the nuclear Hamiltonian within this approximation are then of the form $|n\rangle|lm\rangle$, with corresponding energies $E_{nlm} = \hbar\omega(n+1/2) + hBl(l+1)$. This approximation neglects many of the effects that affect the spectra of real molecules (see, for example, refs. [36, 37] for a more complete discussion of the spectra of real diatomic molecules) but is reasonable for closed shell molecules at very low temperatures and forms the basic theoretical model used in the rest of the present work.

2.3 Molecules in off-resonant laser fields

The time-dependent Schrödinger equation for a molecule in a time-varying electro-magnetic field far from resonance is

$$i\hbar\frac{d}{dt}|\Psi(t)\rangle = \left[H_{\mathrm{mol}} - \mathbf{d}\cdot\mathbf{E}(\mathbf{r},t)\right]|\Psi(t)\rangle, \tag{2.23}$$

where H_{mol} is the molecular Hamiltonian with eigenvalues

$$H_{\mathrm{mol}}|\Psi_i\rangle = E_i|\Psi_i\rangle, \tag{2.24}$$

the electric field is $\mathbf{E}(\mathbf{r},t) = \boldsymbol{\mathcal{E}}(\mathbf{r},t)e^{-i\omega t}/2 + \mathrm{h.c.}$ and ω is the frequency of the monochromatic radiation, assumed to be far from any molecular resonances. By writing the state

$$|\Psi(t)\rangle = \sum_i c_i(t)e^{-i\omega_i t}|\Psi_i\rangle, \tag{2.25}$$

with $E_i/\hbar = \omega_i$, and projecting eq. (2.23) onto state $\langle\Psi_j|$ one arrives at the set of coupled differential equations for the expansion coefficients

$$i\hbar\frac{d}{dt}c_j(t) = -\frac{1}{2}\sum_i c_i(t)\mathbf{d}_{ji}\cdot\left(\boldsymbol{\mathcal{E}}(\mathbf{r},t)e^{i(\omega_{ji}-\omega)t} + \boldsymbol{\mathcal{E}}^*(\mathbf{r},t)e^{i(\omega_{ji}+\omega)t}\right), \tag{2.26}$$

where $\mathbf{d}_{ji} = \langle \Psi_j | \mathbf{d} | \Psi_i \rangle$ and $\omega_{ji} = \omega_j - \omega_i$.

The system of coupled differential equations for the evolution of the coefficients $c_i(t)$, or equivalently for the evolution of the state $|\Psi(t)\rangle$, given in eq. (2.26) is exact but impossible to solve without introducing some approximations. First, the method of essential states [38], that is splitting the set of all states into a set of essential and non-essential states as

$$\begin{aligned} i\hbar \frac{d}{dt} c_j(t) = &-\frac{1}{2} \sum_k c_k(t) \mathbf{d}_{jk} \cdot \left(\boldsymbol{\mathcal{E}}(\mathbf{r},t) e^{i(\omega_{jk}-\omega)t} + \boldsymbol{\mathcal{E}}^*(\mathbf{r},t) e^{i(\omega_{jk}+\omega)t} \right) \\ &- \frac{1}{2} \sum_m c_m(t) \mathbf{d}_{jm} \cdot \left(\boldsymbol{\mathcal{E}}(\mathbf{r},t) e^{i(\omega_{jm}-\omega)t} + \boldsymbol{\mathcal{E}}^*(\mathbf{r},t) e^{i(\omega_{jm}+\omega)t} \right), \end{aligned} \tag{2.27}$$

where state j is assumed to be an essential state and the non-essential states are the set of states in the second sum, with coefficients $c_m(t)$. The non-essential states are further assumed to be uncoupled among themselves (*i.e.*, there are no dipole matrix elements between pairs of non-essential states) and to be initially unpopulated. The time evolution of each of the essential states is then governed by an equation analogous to eq. (2.27) while the non-essential states are governed by a much simpler equation

$$i\hbar \frac{d}{dt} c_m(t) = -\frac{1}{2} \sum_k c_k(t) \mathbf{d}_{mk} \cdot \left(\boldsymbol{\mathcal{E}}(\mathbf{r},t) e^{i(\omega_{mk}-\omega)t} + \boldsymbol{\mathcal{E}}^*(\mathbf{r},t) e^{i(\omega_{mk}+\omega)t} \right). \tag{2.28}$$

The idea behind partitioning the states of the system in this way is that in general only a subset of the states of the system are of interest. For example in this work it is generally the rotational states of a particular vibronic manifold which is of interest. It is then generally desirable to integrate out the contributions from the irrelevant "non-essential" states, which are generally well-separated energetically from the interesting "essential" states. Under these assumptions the solutions to eq. (2.28) for the non-essential states are

$$c_m(t) = -\frac{1}{2i\hbar} \int_{-\infty}^{t} dt' \sum_k c_k(t') \mathbf{d}_{mk} \cdot \left(\boldsymbol{\mathcal{E}}(\mathbf{r},t') e^{i(\omega_{mk}-\omega)t'} + \boldsymbol{\mathcal{E}}^*(\mathbf{r},t') e^{i(\omega_{mk}+\omega)t'} \right), \tag{2.29}$$

where the sum is over only the essential states. These solutions can be further simplified by assuming that $\boldsymbol{\mathcal{E}}(\mathbf{r},t) c_k(t)$ is a very slowly varying function of time, so that it can be taken outside of the integral, resulting in

$$c_m(t) = \frac{1}{2} \sum_k c_k(t) \left(\frac{\mathbf{d}_{mk} \cdot \boldsymbol{\mathcal{E}}(\mathbf{r},t) e^{i(\omega_{mk}-\omega)t}}{E_m - E_k - \hbar\omega} + \frac{\mathbf{d}_{mk} \cdot \boldsymbol{\mathcal{E}}^*(\mathbf{r},t) e^{i(\omega_{mk}+\omega)t}}{E_m - E_k + \hbar\omega} \right). \tag{2.30}$$

Substituting these solutions for the time evolution of the non-essential states into the differential equation for the coefficients $c_j(t)$ and taking the rotating wave approximation, which

neglects terms oscillating at frequencies $\pm 2\omega$, yields

$$\begin{aligned} i\hbar\frac{d}{dt}c_j(t) &= -\frac{1}{2}\sum_k c_k(t)e^{i\omega_{jk}t}\mathbf{d}_{jk}\cdot\left(\boldsymbol{\mathcal{E}}(\mathbf{r},t)e^{-i\omega t}+\text{h.c.}\right) \\ &\quad -\frac{1}{4}\sum_k\sum_m c_k(t)e^{i\omega_{jk}t}\left(\frac{\boldsymbol{\mathcal{E}}^*(\mathrm{r},t)\cdot\mathbf{d}_{jm}\,\mathbf{d}_{mk}\cdot\boldsymbol{\mathcal{E}}(\mathbf{r},t)}{E_m-E_k-\hbar\omega}+\frac{\boldsymbol{\mathcal{E}}(\mathrm{r},t)\cdot\mathbf{d}_{jm}\,\mathbf{d}_{mk}\cdot\boldsymbol{\mathcal{E}}^*(\mathbf{r},t)}{E_m-E_k+\hbar\omega}\right) \\ &= \sum_k c_k(t)e^{i\omega_{jk}t}\langle\Psi_j|H_{\text{dipole}}(\mathbf{r},t)+H_{\text{AC}}(\mathbf{r},t)|\Psi_k\rangle. \end{aligned} \tag{2.31}$$

This is recognizable as the time-dependent Schrödinger equation in the interaction picture defined by H_{mol} for the essential states, under a new Hamiltonian

$$H = H_{\text{mol}} + H_{\text{dipole}}(\mathbf{r},t) + H_{\text{AC}}(\mathbf{r},t) \tag{2.32}$$

$$= H_{\text{mol}} - \mathbf{d}\cdot\mathbf{E}(\mathbf{r},t) - \frac{1}{4}\boldsymbol{\mathcal{E}}^*(\mathbf{r},t)\cdot\alpha(\omega)\cdot\boldsymbol{\mathcal{E}}(\mathbf{r},t), \tag{2.33}$$

where $H_{\text{AC}}(\mathbf{r},t)$ is the AC Stark effect Hamiltonian and $\alpha(\omega)$ is the molecular polarizability

$$\langle\Psi_j|\alpha(\omega)|\Psi_i\rangle = \sum_m\langle\Psi_j|\mathbf{d}|\Psi_m\rangle\langle\Psi_m|\mathbf{d}|\Psi_i\rangle\left(\frac{1}{E_m-E_i-\hbar\omega}+\frac{1}{E_m-E_i+\hbar\omega}\right), \tag{2.34}$$

where the sum is over the non-essential states.

In the molecular body-fixed frame, with the internuclear axis along the z-axis, the polarizability tensor of a molecule can be written as [38]

$$\alpha'(\omega) = \begin{pmatrix} \alpha'_{xx}(\omega) & 0 & 0 \\ 0 & \alpha'_{yy}(\omega) & 0 \\ 0 & 0 & \alpha'_{zz}(\omega) \end{pmatrix}, \tag{2.35}$$

where for diatomic molecules $\alpha'_{xx}(\omega) = \alpha'_{yy}(\omega) \equiv \alpha_\perp(\omega)$ and $\alpha'_{zz}(\omega) \equiv \alpha_\parallel(\omega)$ because of symmetry. However, the applied laser field is defined in the laboratory frame and so either the electric field must be transformed to the molecular frame or the polarizability tensor must be transformed to the laboratory frame in order to perform calculations; the latter is much more common and that is what will be done here. This transformation, which amounts to applying a rotation in order to bring the molecular frame and the laboratory frame into coincidence, is easiest in a spherical basis and so the first step is to express the spherical tensor, $\alpha'^{(k)}_q(\omega)$, in terms of the Cartesian tensor elements, $\alpha'_{ij}(\omega)$. The spherical irreducible tensor elements are related to the Cartesian components through [36]

$$\alpha'^{(k)}_q(\omega) = \sum_{i=1}^{3}\sum_{j=1}^{3} c^{ij}_{kq}\alpha'_{ij}(\omega), \tag{2.36}$$

with

$$c^{ij}_{kq} = \sum_m \langle 1\,m, 1\,q-m|k\,q\rangle \mathbf{U}_{mi}\mathbf{U}_{q-mj}, \tag{2.37}$$

where $\mathbf{U}$ is the unitary transformation between the Cartesian and spherical bases, defined so that

$$v_1^{(1)} = -\frac{v_1 + iv_2}{\sqrt{2}} \tag{2.38}$$

$$v_0^{(1)} = v_3 \tag{2.39}$$

$$v_{-1}^{(1)} = \frac{v_1 - iv_2}{\sqrt{2}}, \tag{2.40}$$

where $v_1 \equiv v_x$, $v_2 \equiv v_y$, and $v_3 \equiv v_z$. Through this transformation the non-vanishing irreducible tensor elements are seen to be

$$\alpha_0'^{(0)}(\omega) = -\frac{1}{\sqrt{3}}\left(\alpha_\parallel(\omega) + 2\alpha_\perp(\omega)\right) \tag{2.41}$$

and

$$\alpha_0'^{(2)}(\omega) = \sqrt{\frac{2}{3}}\left(\alpha_\parallel(\omega) - \alpha_\perp(\omega)\right). \tag{2.42}$$

These spherical irreducible tensor components in the molecular frame are connected to the spherical irreducible tensor components in the laboratory frame through a rotation through angles $\Omega \equiv \{\phi, \theta, \chi\}$, which can be expressed as

$$\alpha_p^{(k)}(\omega) = \sum_q D_{pq}^{k*}(\Omega)\alpha_q'^{(k)}(\omega) \tag{2.43}$$

using the Wigner D-matrices, $D_{pq}^k(\Omega)$ [36]. Now in the laboratory frame, the expression for $H_{\mathrm{AC}}(\mathbf{r}, t)$ is found by first forming the tensor product of the laser envelope function with its complex conjugate, $\mathbf{I}(\mathbf{r}, t) = \boldsymbol{\mathcal{E}}(\mathbf{r}, t) \otimes \boldsymbol{\mathcal{E}}^*(\mathbf{r}, t)$. This is then contracted with the polarizability tensor in the space fixed frame, yielding [36]

$$H_{\mathrm{AC}}(\mathbf{r}, t) = -\frac{1}{4}\boldsymbol{\mathcal{E}}^*(\mathbf{r}, t) \cdot \alpha(\omega) \cdot \boldsymbol{\mathcal{E}}(\mathbf{r}, t) = -\frac{1}{4}\sum_k \sum_q (-1)^{k-q}\alpha_q^{(k)}(\omega)\mathbf{I}_{-q}^{(k)}(\mathbf{r}, t). \tag{2.44}$$

In the case of linearly polarized light polarized along the laboratory z-axis, $\boldsymbol{\mathcal{E}}(\mathbf{r}, t) = \mathbf{e}_0\mathcal{E}_0(\mathbf{r}, t)$, this gives

$$\begin{aligned} H_{\mathrm{AC}}(\mathbf{r}, t) &= -\frac{1}{4}\left|\mathcal{E}_0(\mathbf{r}, t)\right|^2 \left(\frac{1}{3}(\alpha_\parallel(\omega) + 2\alpha_\perp(\omega))D_{00}^{0*}(\Omega) + \frac{2}{3}(\alpha_\parallel(\omega) - \alpha_\perp(\omega))D_{00}^{2*}(\Omega)\right) \\ &= -\frac{1}{4}\left|\mathcal{E}_0(\mathbf{r}, t)\right|^2 \left(\alpha_{\mathrm{avg}}(\omega) + \frac{2}{3}\Delta\alpha(\omega)C_0^2(\theta, \phi)\right), \end{aligned} \tag{2.45}$$

where

$$C_q^k(\theta, \phi) = \sqrt{\frac{4\pi}{2k+1}}Y_k^q(\theta, \phi) \tag{2.46}$$

are the Racah normalized spherical harmonics, related to the Wigner D-matrices through [36]

$$D_{q0}^{k*}(\phi, \theta, \chi) = C_q^k(\theta, \phi). \tag{2.47}$$

2.4 Optical lattices

Within the lowest vibronic band, the effective Hamiltonian for a closed shell diatomic molecule in the presence of intense laser fields is

$$H = \frac{\mathbf{L}^2}{2I} - \frac{1}{4}\left|\mathcal{E}_0(\mathbf{r},t)\right|^2\left(\alpha_{\text{avg}}(\omega) + \frac{2}{3}\Delta\alpha(\omega)C_0^2(\theta,\phi)\right), \tag{2.48}$$

the matrix elements of which are found through the Wigner-Eckart theorem [36]

$$\begin{aligned}\langle(\Phi_i n)lm|H|(\Phi_i n)l'm'\rangle = &\left(hBl(l+1) - \frac{1}{4}\left|\mathcal{E}_0(\mathbf{r},t)\right|^2\alpha_{\text{avg}}(\omega)\right)\delta_{ll'}\delta_{mm'} \\ &- \frac{1}{6}\left|\mathcal{E}_0(\mathbf{r},t)\right|^2\Delta\alpha(\omega)(-1)^{-m}\sqrt{(2l+1)(2l'+1)}\begin{pmatrix} l & 2 & l' \\ 0 & 0 & 0\end{pmatrix}\begin{pmatrix} l & 2 & l' \\ -m & 0 & m'\end{pmatrix}. \end{aligned}\tag{2.49}$$

Calculating the shifts of the ground state, $|(\Phi_i n)00\rangle$, to first order in perturbation theory yields the so-called dynamic or AC Stark Shift [39]

$$\Delta E_{\text{scalar}} = -\frac{1}{4}\left|\mathcal{E}_0(\mathbf{r},t)\right|^2\alpha_{\text{avg}}(\omega), \tag{2.50}$$

which demonstrates that the shift of the energy is proportional to the intensity of the applied laser field. With the addition of a term of the form

$$\Delta E_{lm} = -\frac{1}{6}\left|\mathcal{E}_0(\mathbf{r},t)\right|^2\Delta\alpha(\omega)(-1)^{-m}(2l+1)\begin{pmatrix} l & 2 & l \\ 0 & 0 & 0\end{pmatrix}\begin{pmatrix} l & 2 & l \\ -m & 0 & m\end{pmatrix}, \tag{2.51}$$

this is also true for excited rotational states. Experimentally this difference in shifts for different states may be compensated for by the application of other external fields [3, 25].

In the case that two continuous wave (CW) laser fields counter propagate along the x-axis, creating a standing wave, the time averaged square magnitude of the electric field at the center of the beams gives rise to a position-dependent AC Stark shift [39]

$$\begin{aligned}V(x) &= -\frac{1}{4}\left\langle\left|\mathcal{E}_0(\mathbf{r},t)\right|^2\right\rangle\alpha_{\text{avg}}(\omega) = -\frac{1}{4}\left\langle\left|2E_0\cos(k_L x)\cos(\omega t)\right|^2\right\rangle\alpha_{\text{avg}}(\omega) \\ &= -\frac{1}{2}\left|E_0\right|^2\alpha_{\text{avg}}(\omega)\cos^2(k_L x) = -\frac{1}{2}V_0\cos^2(k_L x),\end{aligned}\tag{2.52}$$

where $k_L = 2\pi/\lambda$ is the wave vector of the laser light. This can be used to create artificial lattices for atoms and molecules, with higher dimensional lattices created by adding pairs of CW lasers traveling along the y- and z-axes [25, 39]. Near the minima of this optically generated potential energy landscape, the potential energy varies approximately as

$$V(x) \approx -\frac{V_0}{2} + \frac{1}{2}V_0 k_L^2 x^2 + O(x^4), \tag{2.53}$$

which is roughly harmonic with a spring constant of $k = V_0 k_L^2$. Using $\omega_{\mathrm{HO}} = \sqrt{k/M} = \sqrt{2V_0 E_r}/\hbar$, where $E_r = \hbar^2 k_L^2/(2M)$ is the recoil energy, a convenient energy scale for lattice confined molecules [25, 39], the root mean squared width of the ground state of a single molecule trapped in the ground state of one of the wells is then approximately

$$\sigma_x \approx \sqrt{\frac{\hbar}{M\omega_{\mathrm{HO}}}}. \tag{2.54}$$

For KRb molecules trapped in a lattice with $\lambda = 1064$ nm and the moderate potential depth of 40 E_r [25] this yields a width of ≈ 80 nm, considerably less than the distance between minima, $\lambda/2 = 532$ nm. This means that to a first approximation, at very low temperatures the molecules may be considered stationary at the minima of the lattice sites. However, Depending on the application, it may be necessary to take the distribution of positions, *i.e.* the translational motion, into account, and for significantly shallower lattices or significantly closer lattice spacings the motion of the molecules should be considered explicitly.

Chapter 3

Path integral ground state Monte Carlo

The study of many-Boson quantum mechanical systems is generally a very challenging task. Except in very simple cases, such many-body problems do not admit analytical solutions and generally must be attacked through approximation methods such as mean-field methods or through clever computational techniques. The path integral ground state Monte Carlo (PIGS) method falls into the latter camp, providing a way to calculate ground state expectation values of time-independent Hamiltonians that can be made to be, in principle, exact by numerically convergent techniques.

PIGS has been used extensively to study quantum many-body systems. This includes van der Waals complexes [40], liquid and solid helium [40, 41], and more recently the approximate elementary excitation spectrum [42] and phase diagram [43] of systems of fully polarized dipoles in two dimensions, with polarization tilted with respect to the normal of the plane of translation. The related reptation Monte Carlo method has been used to study approximate rotational and translational dynamics of single small molecules in ^{4}He clusters [44]. The PIGS method is quite general and has many nice properties. Although it is computationally quite demanding, it scales favorably with particle number, in particular scaling only quadratically with particle number for a pairwise potential. The few necessary approximations are controllable and although a trial wave function is one of the few inputs to the method, very little knowledge of the solution is required to get good results; in fact it is possible to get good results using a trivial constant trial wave function, $\Psi_{\text{trial}}(\mathbf{X}) = C$ [41]. The only limitations to the PIGS method are that it is restricted to the ground state of systems with time-independent Hamiltonians. System dynamics are accessible only through approximate methods which relate dynamical properties to ground state expectation values, *e.g.* the well-known Feynman-Bijl approximation to the elementary excitation spectrum [33, 34] which relates the low energy excitation spectrum to the static structure factor, or the projection operator imaginary time spectral evolution (POITSE) [45] or path integral correlation function (PICF) [46] methods.

3.1 A brief derivation

This method takes two inputs. First, a time-independent N-body Hamiltonian, often of the form

$$H = T + V = \sum_{i=1}^{N} T_i + V_{\text{ext}}(\mathbf{x}_i) + \sum_{j<i} V_{\text{int}}(\mathbf{x}_i, \mathbf{x}_j), \tag{3.1}$$

where T_i is the total kinetic energy operator of particle i and V_{ext} and V_{int} are the applied potential and interaction potential, respectively, is required. Second, an N-body trial state $|\Psi_{\text{trial}}\rangle$, must be supplied. In this context $\mathbf{x}_i$ denotes all of the coordinates of particle i, which could include translational coordinates as well as rotational coordinates, and $\mathbf{X} \equiv \{\mathbf{x}_1, \ldots, \mathbf{x}_N\}$ denotes all of the coordinates of all N particles. In the eigenbasis of the Hamiltonian H,

$$H|\Phi_i\rangle = E_i|\Phi_i\rangle, \tag{3.2}$$

the trial wave function may be expressed as

$$|\Psi_{\text{trial}}\rangle = \sum_k c_k|\Phi_k\rangle. \tag{3.3}$$

The time-evolution of the system is given by

$$G(t, t_0)|\Psi_{\text{trial}}\rangle = \sum_k c_k e^{-iE_k(t-t_0)/\hbar}|\Phi_k\rangle, \tag{3.4}$$

where $G(t, t_0) = G(t - t_0) = e^{-iH(t-t_0)/\hbar}$ is the time-evolution operator or propagator. Using a Wick rotation, this same evolution in imaginary time ($\beta = it$) is given by

$$G(\beta)|\Psi_{\text{trial}}\rangle = \sum_k c_k e^{-E_k\beta/\hbar}|\Phi_k\rangle, \tag{3.5}$$

so that the oscillatory phase factors of eq. (3.4) become decaying exponentials. As long as the trial wave function satisfies

$$\langle\Phi_0|\Psi_{\text{trial}}\rangle = c_0 \neq 0, \tag{3.6}$$

which is to say the overlap with the ground state ($|\Phi_0\rangle$) is non-vanishing, then in the limit

$$\lim_{\beta\to\infty} \frac{G(\beta/2)|\Psi_{\text{trial}}\rangle}{\sqrt{\langle\Psi_{\text{trial}}|G(\beta)|\Psi_{\text{trial}}\rangle}} = |\Phi_0\rangle \tag{3.7}$$

the trial wave function decays to the ground state wave function. This can be used to calculate ground state expectation values as

$$\langle O\rangle = \lim_{\beta\to\infty} \frac{\langle\Psi_{\text{trial}}|G(\beta/2)OG(\beta/2)|\Psi_{\text{trial}}\rangle}{\langle\Psi_{\text{trial}}|G(\beta)|\Psi_{\text{trial}}\rangle} = \frac{\langle\Phi_0|O|\Phi_0\rangle}{\langle\Phi_0|\Phi_0\rangle}, \tag{3.8}$$

which requires knowledge only of the form of the Hamiltonian and the ability to construct a suitable trial state.

While it seems that this offers a simple way to exactly solve the quantum many-body problem, there is, however, a catch: exactly computing the imaginary-time propagator

$$G(\beta) = \sum_i e^{-E_i \beta/\hbar} |\Psi_i\rangle\langle\Psi_i| \tag{3.9}$$

is just as hard as determining all of the eigenstates of the Hamiltonian. In order to make any progress it is then necessary to introduce some approximations. To begin it is useful to use the fact that the a propagation interval can, without approximation, be broken up into many smaller propagation intervals $\tau = \beta/M$ as

$$G(\beta) = G(M\tau) = \left(G(\tau)\right)^M, \tag{3.10}$$

which directly follows from the definition of the propagator.

Then having broken the propagator up into a product of propagators over shorter intervals, it is possible to make approximations to the propagator which are valid only for short times, *i.e.* replace $G(\tau)$ with $G_n(\tau) = G(\tau) + O(\tau^{n+1})$, which is accurate to nth order in the small time step, τ, (see section 3.3). The expression for expectation values becomes

$$\langle O\rangle = \lim_{\beta\to\infty} \lim_{M\to\infty} \frac{\langle\Psi_{\rm trial}| \left(G_n(\beta/M)\right)^{M/2} O \left(G_n(\beta/M)\right)^{M/2} |\Psi_{\rm trial}\rangle}{\langle\Psi_{\rm trial}| \left(G_n(\beta/M)\right)^{M} |\Psi_{\rm trial}\rangle}, \tag{3.11}$$

showing that if it is possible to evaluate the short time propagator in some basis and the extrapolation to infinite path length can be performed, then it is possible to calculate ground-state expectation values that can be made to be arbitrarily close to the exact values.

In what follows it is most convenient to work in the position representation. Transforming into this representation is accomplished simply through insertions of factors of the identity, $\mathbb{I} = \int_{\rm all} d\mathbf{X}\ |\mathbf{X}\rangle\langle\mathbf{X}|$, where the integral is understood to be taken over all space for all of the coordinates for both translational and rotational degrees of freedom of all N of the particles, into eq. (3.11). The expression for the expectation value of an operator, O, which is diagonal in the position representation, is

$$\begin{aligned}\langle O\rangle = \lim_{\beta\to\infty} \lim_{M\to\infty} & \frac{1}{N(\beta,M)} \\ & \times \int_{\rm all} d^M\mathbf{X}\ \left[\Psi^*_{\rm trial}(\mathbf{X}_1) \left(\prod_{i=1}^{M-1} G_n(\mathbf{X}_i, \mathbf{X}_{i+1}, \tau)\right) \Psi_{\rm trial}(\mathbf{X}_M)\right] O(\mathbf{X}_{\lfloor M/2\rfloor+1}),\end{aligned} \tag{3.12}$$

where the normalization is

$$N(\beta,M) = \int_{\rm all} d^M\mathbf{X}\ \Psi^*_{\rm trial}(\mathbf{X}_1) \left(\prod_{i=1}^{M-1} G_n(\mathbf{X}_i, \mathbf{X}_{i+1}, \tau)\right) \Psi_{\rm trial}(\mathbf{X}_M). \tag{3.13}$$

Here, and in the rest of the present work, the convention that the index $i = 1, \ldots, M$ in eq. (3.12) and eq. (3.13) starts from 1, which slightly modifies the definition of τ in a trivial way so that $\tau = \beta/(M-1)$, is adopted. Here $\mathbf{X}_j$ (where $j = 1, \cdots, M$) is the set of all coordinates of all molecules at imaginary time $(j-1)\tau$ so that when $j = \lfloor M/2 \rfloor + 1$ ($\lfloor i \rfloor \equiv \text{floor}(i)$) the system has evolved through the imaginary time interval $\beta/2$, $G_n(\mathbf{X}, \mathbf{X}', \tau) = \langle \mathbf{X}|G_n(\tau)|\mathbf{X}'\rangle$, and $\Psi_{\text{trial}}(\mathbf{X}) = \langle \mathbf{X}|\Psi_{\text{trial}}\rangle$. At first glance eq. (3.12) does not appear to be more useful than eq. (3.8) because it still requires the evaluation of the limit as $\beta \to \infty$ to compute ground state expectation values without contamination from excited states, and adds the complexity of evaluating an infinite dimensional integral (since it is only exact in the limit that $M \to \infty$). However, this equation provides a way to systematically improve estimates of ground state expectation values by evaluating this expression for finite but progressively larger values of β and M until convergence of all expectation value estimates of interest,

$$\langle O \rangle \approx \frac{1}{N(\beta, M)} \int_{\text{all}} d^M \mathbf{X} \left[\Psi^*_{\text{trial}}(\mathbf{X}_1) \left(\prod_{i=1}^{M-1} G_n(\mathbf{X}_i, \mathbf{X}_{i+1}, \tau) \right) \Psi_{\text{trial}}(\mathbf{X}_M) \right] O(\mathbf{X}_{\lfloor M/2 \rfloor + 1}), \tag{3.14}$$

with finite β and M, is found with respect to β and M (or equivalently with respect to β and τ since $\beta = (M-1)\tau$). It should be noted that the estimates of expectation values of different operators may converge with respect to β and M at different rates.

Convergence of expectation value estimates with respect to M is governed by the accuracy of the short-time approximation to the propagator, $G_n(\tau)$, which goes approximately as $\tau^n \propto 1/M^n$ for fixed β. The time step, τ, required for a given simulation is largely determined by the Hamiltonian, H, and how weakly the particles interact, either with one-another or with an external field, since the most popular approximations to $G(\tau)$ become exact in the limit of free (non-interacting) particles. The convergence with respect to β depends on the Hamiltonian, through the gap between the ground state and excited state energies (see eq. (3.5)), and also on the choice of trial wave function, through the overlap between the ground state wave function and the trial wave function. In the limit of long imaginary path lengths, β, eq. (3.5) implies that estimates of expectation values will converge approximately as $c_0 e^{-(E_1 - E_0)\beta/2\hbar}$.

More than this, the particular form of eq. (3.12) also suggests an algorithm for evaluating such expectation values. Under certain circumstances specified below, the quantity

$$P(\mathbf{X}_1, \ldots, \mathbf{X}_M; \beta, M) = \Psi^*_{\text{trial}}(\mathbf{X}_1) \left(\prod_{i=1}^{M-1} G_n(\mathbf{X}_i, \mathbf{X}_{i+1}, \tau) \right) \Psi_{\text{trial}}(\mathbf{X}_M)/N(\beta, M) \tag{3.15}$$

can be interpreted as a probability density function (PDF), in which case the expectation value is

$$\langle O \rangle = \lim_{\beta \to \infty} \lim_{M \to \infty} \int_{\text{all}} d^M \mathbf{X} \; P(\mathbf{X}_1, \ldots, \mathbf{X}_M; \beta, M) O(\mathbf{X}_{\lfloor M/2 \rfloor + 1}). \tag{3.16}$$

This can be approximated for given values of β and M as

$$\langle O \rangle \approx \lim_{K\to\infty} \frac{1}{K} \sum_{i=1}^{K} O(\left[\mathbf{X}_{\lfloor M/2 \rfloor+1}\right]_i), \tag{3.17}$$

with $\left[\mathbf{X}_{\lfloor M/2 \rfloor+1}\right]_i$ denoting the center configuration of the ith sample drawn from the PDF $P(\mathbf{X}_1, \ldots, \mathbf{X}_M; \beta, M)$. In this way it is possible to evaluate a high dimensional integral using Monte Carlo integration. The requirements for interpreting $P(\mathbf{X}_1, \ldots, \mathbf{X}_M; \beta, M)$ as a PDF are simply that $G_n(\mathbf{X}, \mathbf{X}', \tau) > 0$ and $\Psi_{\text{trial}}(\mathbf{X}) > 0$ for all $\mathbf{X}$ and $\mathbf{X}'$ which is true for Bosonic and distinguishable particles and for positive valued trial wave functions.

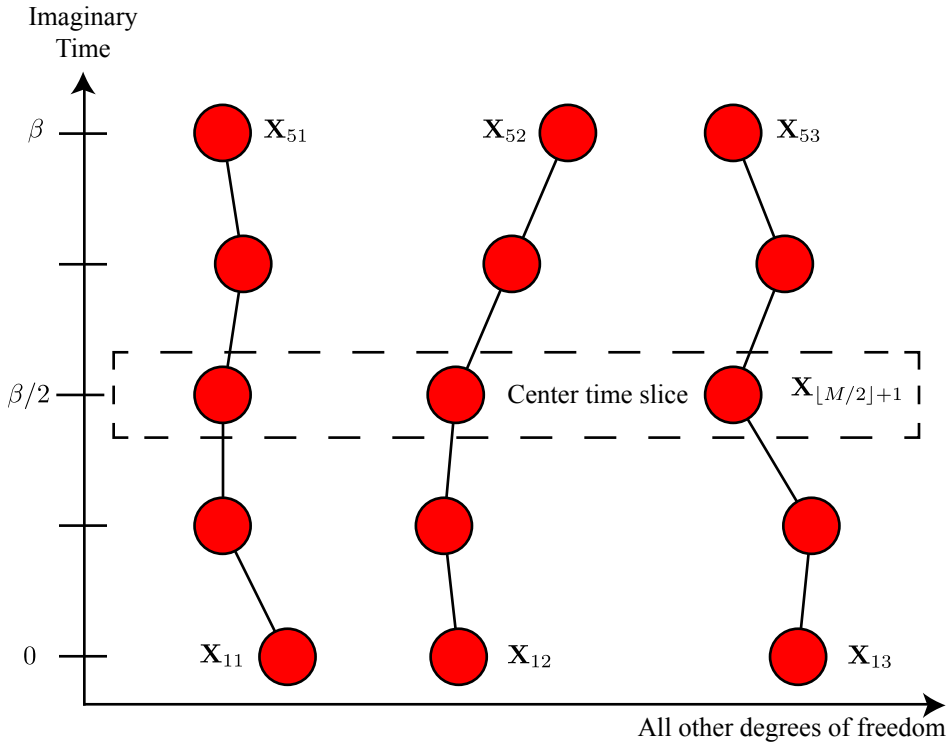

Figure 3.1: Schematic of a single path configuration in a typical PIGS simulation for $N = 3$ particles and $M = 5$ time slices. The vertical axis is the imaginary time and the horizontal axis represents the state of all other degrees of freedom, in this case the positions of the three particles in one spatial dimension. Each red dot represents a bead, and horizontal groupings of beads are referred to in the text as time slices. Vertical groupings of beads, connected by lines, represent the state of the particle at all time slices. The statistical weight of this path is given by eq. (3.15).

The set of particle configurations $\mathbf{P} \equiv \{\mathbf{X}_1, \ldots, \mathbf{X}_M\}$ is commonly referred to a path, the individual configurations at imaginary time $(j-1)\tau$, $\mathbf{X}_j$, commonly referred to as a time-slice,

and the coordinates of the kth particle on the jth time-slice, $\mathbf{X}_{jk}$, often referred to as a bead, depicted in figure 3.1. This stems from the related, and better-known, finite-temperature path integral Monte Carlo (PIMC) [47] method. Though the methods are similar, there are several important differences between PIGS and PIMC. PIMC is a finite-temperature method, and it computes thermal expectation values

$$\langle O \rangle = \frac{1}{\mathcal{Z}} \mathrm{Tr}\left[\rho_{\mathrm{thermal}}(\beta) O\right], \tag{3.18}$$

where $\rho_{\mathrm{thermal}}(\beta)$ is the thermal density matrix at some inverse temperature, β,

$$\rho_{\mathrm{thermal}}(\mathbf{X}, \mathbf{X}'; \beta) = \sum_k e^{-\beta E_k} \langle \mathbf{X} | \Phi_k \rangle \langle \Phi_k | \mathbf{X}' \rangle \tag{3.19}$$

and $\mathcal{Z} = \mathrm{Tr}\left[\rho_{\mathrm{thermal}}(\beta)\right]$ is the partition function. This is accomplished in PIMC by exploiting the similarity between the expressions for the thermal density matrix at an inverse temperature $\beta = 1/(k_B T)$, eq. (3.19), and the imaginary time propagator through some imaginary time interval, eq. (3.9), with longer imaginary time intervals corresponding to lower temperatures. Algorithmically, much is unchanged when going from the ground state PIGS method to the finite temperature PIMC method: the principle difference between the finite temperature PIMC method and the ground state PIGS method is that at finite temperatures the path must be periodic in imaginary time in order to preserve the cyclic nature of the trace in eq. (3.18) [47]. This means that the expression for the PDF in the case of PIMC contains an additional term in the product of eq. (3.15) like $G_n(\mathbf{X}_M, \mathbf{X}_1, \tau)$ as well as omitting the trial wave function factors.

With regards to computing expectation values, owing to the periodic nature of the imaginary-time paths in the PIMC method, all time-slices are equivalent and so expectation values can be computed from configurations on each of them, leading to much better sampling statistics. This is in contrast to the PIGS method in which only the central time-slice, $\lfloor M/2 \rfloor + 1$, (the time-slice occurring after a propagation interval $\beta/2$, see eq. (3.7)) is distributed (approximately, in the case of finite β and M) according to the ground state density,

$$\rho_0(\mathbf{X}, \mathbf{X}') = \langle \mathbf{X} | \Phi_0 \rangle \langle \Phi_0 | \mathbf{X}' \rangle. \tag{3.20}$$

This is a consequence of the difference in boundary conditions in imaginary time between PIMC and PIGS, with PIMC having periodic boundaries and PIGS having open boundary conditions in time. Despite these differences, however, both the algorithms for sampling paths and the short-time approximations to the propagator developed for PIMC can, for the most part, be applied equally well to PIGS.

Energy

Another significant difference between PIGS and PIMC is the estimator for the energy. Because PIGS employs a trial wave function and because the Hamiltonian commutes with

the propagator (and approximately commutes with the propagator approximations, $G_n(\tau)$) it is possible to estimate the energy of the system using the local energy estimator. This is defined as

$$E_{\text{local}}(\mathbf{X}) = \frac{1}{\Psi_{\text{trial}}(\mathbf{X})} H\Psi_{\text{trial}}(\mathbf{X}) = \frac{1}{\Psi_{\text{trial}}(\mathbf{X})} T\Psi_{\text{trial}}(\mathbf{X}) + V(\mathbf{X}). \tag{3.21}$$

This quantity depends on the value of the trial wave function and is therefore necessarily evaluated at the two ends of the path (time-slices $\mathbf{X}_1$ and $\mathbf{X}_M$). The quality of this estimator depends on the quality of the trial wave function employed but provides an alternative to the energy estimators employed in PIMC simulations, especially kinetic energy estimators that are non-local in imaginary-time [47]. In addition, since the potential energy is diagonal in the position representation it is possible to get an additional estimate of the potential energy simply by sampling $V(\mathbf{X}_{\lfloor M/2 \rfloor + 1})$.

Non-diagonal operators

With PIGS it is also possible to sample operators which are not diagonal in the position representation, most notably the one body reduced density matrix (1-RDM or OBDM) [41]. Such an operator can be written in the position representation as $O(\mathbf{X}, \mathbf{X}')$, where both $\mathbf{X}$ and $\mathbf{X}'$ reside on the same time-slice, namely the central time slice $\lfloor M/2 \rfloor + 1$, but represent different configurations of the system. In this case the expression for the expectation value is

$$\begin{aligned}\langle O \rangle = \lim_{\beta\to\infty} \lim_{M\to\infty} \frac{1}{N(\beta, M)} \int_{\text{all}} d^M\mathbf{X}\, d\tilde{\mathbf{X}} \Bigg[\Psi^*_{\text{trial}}(\mathbf{X}_1) \left(\prod_{i=1}^{\lfloor M/2 \rfloor} G_n(\mathbf{X}_i, \mathbf{X}_{i+1}, \tau) \right) \\ \times G_n(\tilde{\mathbf{X}}, \mathbf{X}_{\lfloor M/2 \rfloor + 2}, \tau) \left(\prod_{i=\lfloor M/2 \rfloor + 2}^{M-1} G_n(\mathbf{X}_i, \mathbf{X}_{i+1}, \tau) \right) \Psi_{\text{trial}}(\mathbf{X}_M) \Bigg] O(\mathbf{X}_{\lfloor M/2 \rfloor + 1}, \tilde{\mathbf{X}}),\end{aligned} \tag{3.22}$$

where an additional center time-slice, $\tilde{\mathbf{X}}$, has been added, residing alongside the configuration $\mathbf{X}_{\lfloor M/2 \rfloor + 1}$, see figure 3.1. This changes the probability density to

$$\begin{aligned}P_{\text{cut}}(\mathbf{X}_1, \ldots, \mathbf{X}_M, \tilde{\mathbf{X}}; \beta, M) = \Psi^*_{\text{trial}}(\mathbf{X}_1) \left(\prod_{i=1}^{\lfloor M/2 \rfloor} G_n(\mathbf{X}_i, \mathbf{X}_{i+1}, \tau) \right) \\ \times G_n(\tilde{\mathbf{X}}, \mathbf{X}_{\lfloor M/2 \rfloor + 2}, \tau) \left(\prod_{i=\lfloor M/2 \rfloor + 2}^{M-1} G_n(\mathbf{X}_i, \mathbf{X}_{i+1}, \tau) \right) \Psi_{\text{trial}}(\mathbf{X}_M) / N(\beta, M),\end{aligned} \tag{3.23}$$

which can still be interpreted without any issues as a PDF as long as the previously established conditions for interpreting $P(\mathbf{X}_1, \ldots, \mathbf{X}_M; \beta, M)$ as a pd.f. are met ($G(\mathbf{X}, \mathbf{X}', \tau) > 0$ and $\Psi_{\text{trial}}(\mathbf{X}) > 0$).

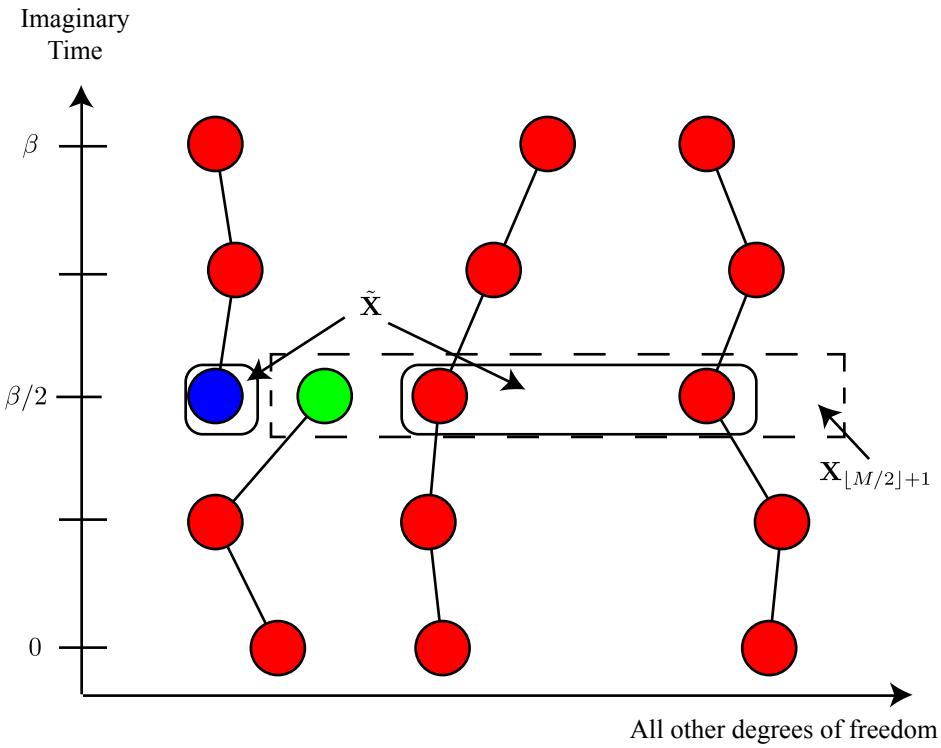

Figure 3.2: Schematic of a single path configuration in a cut path PIGS simulation for $N = 3$ particles and $M = 5$ time slices the path of a single particle cut. When calculating interactions between particles for the propagators described in section 3.3, only beads corresponding to different particles on the same time slice are allowed to interact. This means that the bead in $\mathbf{X}_{\lfloor M/2 \rfloor+1}$ which isn't in $\tilde{\mathbf{X}}$ (green) and the bead which is in $\tilde{\mathbf{X}}$ but not in $\mathbf{X}_{\lfloor M/2 \rfloor+1}$ (blue), both of which represent the same particle, do not interact with one another. The statistical weight of this path is given by eq. (3.23).

Algorithmically, estimating the expectation value of such an operator is accomplished by "breaking" the path and inserting an extra configuration at $\lfloor M/2 \rfloor+1$, often only for a subset of particles as depicted for a single particle in figure 3.1, and then sampling expectation values using the PDF defined in eq. (3.23). The only caveat is that this process of breaking the path also changes the normalization of computed expectation values, $N(\beta, M)$, to that of a

different distribution

$$N_{\rm cut}(\beta,M)=\int_{\rm all} d^M\mathbf{X}\; d\tilde{\mathbf{X}}\; \Psi^*_{\rm trial}(\mathbf{X}_1)\left(\prod_{i=1}^{\lfloor M/2\rfloor} G_n(\mathbf{X}_i,\mathbf{X}_{i+1},\tau)\right) \times G_n(\tilde{\mathbf{X}},\mathbf{X}_{\lfloor M/2\rfloor+2},\tau)\left(\prod_{i=\lfloor M/2\rfloor+2}^{M-1} G_n(\mathbf{X}_i,\mathbf{X}_{i+1},\tau)\right)\Psi_{\rm trial}(\mathbf{X}_M) \quad (3.24)$$

meaning that only non-quantitative information can be gleaned when introducing a cut path in this way. This limitation may be overcome through the implementation of a zero temperature version of the worm algorithm [41, 48, 49].

3.2 Algorithms

In order to estimate operator expectation values using the PIGS method it is necessary to have some way of sampling paths, $\mathbf{P}$, figure 3.1, from the PDF $P(\mathbf{X}_1,\ldots,\mathbf{X}_M;\beta,M)$ defined in eq. (3.15), or the analogous cut paths, figure 3.1, the PDF for cut paths defined in eq. (3.23). This can be accomplished by use of the well-known Metropolis algorithm [50, 51]. The Metropolis algorithm works by finding a Markov process with transition kernel for going from an initial state x to a final state x', $p(x,x')$, satisfying

$$\int_{\rm all} dx\; p(x,x')=1 \quad (3.25)$$

and $p(x,x')\geq 0$, the stationary distribution of which is some target PDF, $\pi(x)$, meaning

$$\pi(x')=\int_{\rm all} dx\; p(x,x')\pi(x). \quad (3.26)$$

The Metropolis algorithm supposes that $p(x,x')$ satisfies a stronger requirement, that of detailed balance, so that

$$\pi(x')p(x,x')=\pi(x)p(x',x) \quad (3.27)$$

and the transition kernel can then be written as

$$p(x,x')=A(x,x')M(x,x'), \quad (3.28)$$

where $M(x,x')$ is some (known) candidate generating distribution and $A(x,x')$ is an acceptance distribution. The problem is then to find an acceptance distribution, $A(x,x')$, given $\pi(x)$ and $M(x,x')$ fulfilling detailed balance so that

$$\frac{A(x',x)}{A(x,x')}=\frac{\pi(x')M(x,x')}{\pi(x)M(x',x)}. \quad (3.29)$$

This can be satisfied by choosing

$$A(x', x) = \min\left(\frac{\pi(x')M(x, x')}{\pi(x)M(x', x)}, 1\right) \tag{3.30}$$

or, if $M(x, x')$ is symmetric, as it is in most commonly used candidate generating distributions such as in the single bead move described below,

$$A(x', x) = \min\left(\frac{\pi(x')}{\pi(x)}, 1\right). \tag{3.31}$$

Given some way to transition from an initial state, x, to a new state, x', the probability of accepting that move in this scheme is determined by the ratio of the probabilities, *i.e.* the values of the stationary PDF for the initial state, $\pi(x)$ and the candidate state, $\pi(x')$. A transition from a less probable state to a more probable one, $\pi(x) < \pi(x')$, will always be accepted with unit probability, so that more probable states will be sampled more often than less probable states, but ergodicity is nevertheless preserved. This meaning that it is possible to transition from state x to state x' in a finite number of steps and the probability of doing so is non-zero, since the acceptance probability is only zero in the case that the probability of a given state, $\pi(x')$, is zero, *i.e.* the state is not allowed for some reason.

Since the Markov process $p(x, x')$ is ergodic, generating new states through $p(x, x')$ will allow the sampling of states distributed according to $\pi(x)$. Presuming that $p(x, x')$ is of the form given in eq. (3.28) with an acceptance distribution of the form in eq. (3.30), no knowledge of the normalization of $\pi(x)$ is required in order to sample states from this distribution: only knowledge of the relative probabilities of any two states is required. Algorithmically, sampling from $\pi(x)$ is then accomplished by:

1. pick an initial state, x,
2. generate a new state, x', using the candidate distribution $M(x', x)$,
3. calculate the acceptance probability $A(x', x)$,
4. generate a random number u from the uniform probability distribution from 0 to 1, $\mathcal{U}(0, 1)$,
5. if $u < A(x', x)$ then update the current state x to the trial state x', otherwise remain at state x,
6. return to step 2.

Steps 2 to 6 are iterated, utilizing the generated states x to compute expectation values

$$\langle f \rangle = \int_{\text{all}} dx\ \pi(x) f(x) \approx \frac{1}{K} \sum_{i=1}^{K} f(x_i) \tag{3.32}$$

until adequate sample statistics have been obtained. This will generate correct expectation values as long the sampling is ergodic [50]. However, subsequent states will necessarily be correlated with one another [52]. This requires that any simulation using this algorithm begin with a "burn-in" period in which the first $K_0 \ll K$ states be thrown away without computing expectation values, to ensure that any correlations with the initial state have sufficiently decayed. It also requires, for the estimation of errors on computed expectation values, that care be taken to incorporate the effects of correlations between samples $f_i = f(x_i)$ [52]. This can easily be accomplished by computing expectation values using only one out of every N states sampled, where N is some number large enough that x_i and x_{i+N} are essentially uncorrelated but $N \ll K$.

The Metropolis method of sampling from a target distribution is extremely useful in cases such as those that arise in statistical physics [50, 51], where the normalization of the distribution is impractical to calculate but the relative probabilities have relatively simple forms. In the case of PIGS simulations the states are the paths, $x = \mathbf{P}$, with probabilities $\pi(\mathbf{P}) = P(\mathbf{X}_1, \ldots, \mathbf{X}_M; \beta, M)$ defined in eq. (3.15), or $P_{\text{cut}}(\mathbf{X}_1, \ldots, \mathbf{X}_M, \tilde{\mathbf{X}}; \beta, M)$ from eq. (3.23) in the case of a cut-path simulation. For simulations of linear rigid rotors in d dimensions the configurations which make up the paths, $\mathbf{P}$ are the locations and orientations of the beads, $\mathbf{X}_{ij} \equiv \{\mathbf{r}_{ij}, \mathbf{n}_{ij}\}$, where $\mathbf{r}_{ij}$ represents the d-dimensional position vector of a particle and $\mathbf{n}_{ij}$ is a 3-dimensional unit vector representing the orientation of the same particle. The candidate distribution, $M(\mathbf{P}, \mathbf{P}')$, of eq. (3.30) depends on what, and how, degrees of freedom are being updated. In what follows, several candidate generating distributions for generating new configurations will be described for translational and rotational degrees of freedom. In order to sample both sets of degrees of freedom in the same simulation, all that is necessary is to add an additional step at the beginning of each of the following moves in which either the rotational or translational degrees of freedom are chosen randomly for each update.

Single bead moves

The simplest type of move involves the displacement of all or a subset of the degrees of freedom of a single particle at one time-slice, *i.e.* one bead. Such a move begins by picking a particle index, j, randomly from the interval $[1, N]$ and a slice index, i, randomly from the interval $[1, M]$, and additionally choosing randomly between $\mathbf{X}_{ij}$ and $\tilde{\mathbf{X}}_j$ in the case $i = \lfloor M/2 \rfloor + 1$ in a cut path simulation. In the case of a translational update, a d-dimensional vector, $\mathbf{v}$, is then generated, *e.g.* by sampling d numbers from a normal distribution $\mathcal{N}(0, \sigma^2)$. The new trial path is generated by displacing bead $\mathbf{r}_{ij}$

$$\mathbf{r}'_{ij} = \mathbf{r}_{ij} + \mathbf{v}. \tag{3.33}$$

When sampling orientations the trial orientation $\mathbf{n}'_{ij}$ is generated by picking a random 3-dimensional unit vector $\hat{\mathbf{v}}$ fulfilling $\mathbf{n}_{ij} \cdot \hat{\mathbf{v}} = 0$ as well as a random rotation angle, $\theta \in [0, \pi)$ from, for example, a truncated normal distribution or a uniform distribution

$\mathcal{U}(0,\pi)$. Only when $\hat{\mathbf{v}}$ fulfills $\mathbf{n}_{ij}\cdot\hat{\mathbf{v}}=0$ will the angle between $\mathbf{n}_{ij}$ and $\mathbf{n}'_{ij}$ necessarily be θ, removing ambiguities in the candidate generating distribution. Defining a unit quaternion $\mathbf{q}=\cos\theta/2+\hat{\mathbf{v}}\sin\theta/2$ [53, 54], the new orientation is generated by conjugating $\mathbf{n}_{ij}$ by $\mathbf{q}$

$$\mathbf{n}'_{ij}=\mathbf{q}(\mathbf{n}_{ij})\mathbf{q}^{-1}. \tag{3.34}$$

This is accomplished by using the rules for quaternion multiplication which are, defining $\mathbf{q}_1=a_1+\mathbf{u}_1$ and $\mathbf{q}_2=a_2+\mathbf{u}_2$,

$$\mathbf{q}_1\mathbf{q}_2=(a_1a_2-\mathbf{u}_1\cdot\mathbf{u}_2)+(a_1\mathbf{u}_2+a_2\mathbf{u}_1+\mathbf{u}_1\times\mathbf{u}_2) \tag{3.35}$$

and

$$\mathbf{q}^{-1}=\frac{\mathbf{q}^*}{||\mathbf{q}||^2}=\frac{a-\mathbf{u}}{a^2+||\mathbf{u}||^2}. \tag{3.36}$$

Here the vector $\mathbf{n}_{ij}$ has been interpreted as a purely imaginary unit quaternion, *i.e.* $\mathbf{q}=0+\mathbf{n}_{ij}$.

In either case the new path configuration, $\mathbf{P}'$, formed by replacing $\mathbf{X}_{ij}$ with $\mathbf{X}'_{ij}$ in $\mathbf{P}$, is accepted with a probability of the form in eq. (3.30),

$$A(\mathbf{P}',\mathbf{P})=\min\left(\frac{P(\mathbf{P}';\beta,M)}{P(\mathbf{P};\beta,M)},1\right), \tag{3.37}$$

where $P_{\text{cut}}(\mathbf{P};\beta,M)$ is substituted for $P(\mathbf{P}';\beta,M)$ in both the numerator and denominator in the case of a cut path simulation. Regardless of this additional detail, any candidate generating distribution $M(\mathbf{P},\mathbf{P}')$ is symmetric for single bead moves and cancels in the expression above. This can be further simplified by recognizing that the coordinates of particle j on only a single time-slice i have been updated and so all terms in $P(\mathbf{P};\beta,M)$ that do not depend on the coordinates of the particles on that time slice i cancel in the ratio in eq. (3.37), resulting in the acceptance probability

$$A(\mathbf{P}',\mathbf{P})=\min\left(\frac{G_n(\mathbf{X}_{i-1},\mathbf{X}'_i,\tau)G_n(\mathbf{X}'_i,\mathbf{X}_{i+1},\tau)}{G_n(\mathbf{X}_{i-1},\mathbf{X}_i,\tau)G_n(\mathbf{X}_i,\mathbf{X}_{i+1},\tau)},1\right) \tag{3.38}$$

for $1<i<M$,

$$A(\mathbf{P}',\mathbf{P})=\min\left(\frac{\Psi_{\text{trial}}(\mathbf{X}'_1)G_n(\mathbf{X}'_1,\mathbf{X}_2,\tau)}{\Psi_{\text{trial}}(\mathbf{X}_1)G_n(\mathbf{X}_1,\mathbf{X}_2,\tau)},1\right) \tag{3.39}$$

for $i=1$, and

$$A(\mathbf{P}',\mathbf{P})=\min\left(\frac{G_n(\mathbf{X}_{M-1},\mathbf{X}'_M,\tau)\Psi_{\text{trial}}(\mathbf{X}'_M)}{G_n(\mathbf{X}_{M-1},\mathbf{X}_M,\tau)\Psi_{\text{trial}}(\mathbf{X}_M)},1\right) \tag{3.40}$$

for $i=M$. In the case that the path of particle j is cut and i is the center time slice, $\lfloor M/2\rfloor+1$, and the bead $\tilde{\mathbf{X}}_j$ was updated the acceptance probability is

$$A(\mathbf{P}',\mathbf{P})=\min\left(\frac{G_n(\tilde{\mathbf{X}}',\mathbf{X}_{\lfloor M/2\rfloor+2},\tau)}{G_n(\tilde{\mathbf{X}},\mathbf{X}_{\lfloor M/2\rfloor+2},\tau)},1\right). \tag{3.41}$$

If, under the same circumstances (the path of particle j is cut, $i = \lfloor M/2 \rfloor + 1$), the bead $\mathbf{X}_{ij}$ is updated instead, the acceptance probability is

$$A(\mathbf{P}', \mathbf{P}) = \min\left(\frac{G_n(\mathbf{X}_{\lfloor M/2 \rfloor}, \mathbf{X}'_{\lfloor M/2 \rfloor + 1}, \tau)}{G_n(\mathbf{X}_{\lfloor M/2 \rfloor}, \mathbf{X}_{\lfloor M/2 \rfloor + 1}, \tau)}, 1\right). \tag{3.42}$$

This type of move is very simple and is useful as a consistency check, being easy implement and debug. This move, however, is incapable of generating significantly different path configurations quickly. For this reason it is preferable to use any of the following classes of moves, each of which updates a much larger section of the path at once.

Rigid path moves

A move type which has the potential to change much larger sections of the path, the rigid path move works by updating the positions or orientations of all of the beads corresponding to a single particle, *i.e.* updating $\mathbf{X}_{ij}$ for all slices i given a particle index j, by displacing them/rotating them by the same amount. This keeps the relative positions/orientations between the same particle at different slices the same, making this kind of move unsuitable for sampling paths on its own, but able to change the position of a single particle relative to all other particles on all of the time slices. This allows this type of move to make much larger updates, modifying more degrees of freedom of the system at once, making it a useful addition to either single bead moves or the multi-level bisection algorithm described below.

This move type begins by selecting a random particle index, j, from the interval $[1, N]$. In the case of a translational move a random d-dimensional vector, $\mathbf{v}$, is chosen such that all d members are sampled from a normal distribution, $\mathcal{N}(0, \sigma^2)$. Then all of the beads $\mathbf{r}_{ij}$, with i ranging from 1 to N, are displaced by this same amount,

$$\mathbf{r}'_{ij} = \mathbf{r}_{ij} + \mathbf{v}. \tag{3.43}$$

In the case of orientations a random 3-dimensional unit vector, $\hat{\mathbf{v}}$, and a random angle, $\theta \in [0, \pi]$, are selected. Then a unit quaternion, $\mathbf{q} = \cos\theta/2 + \hat{\mathbf{v}}\sin\theta/2 = a + b\hat{\mathbf{i}} + c\hat{\mathbf{j}} + d\hat{\mathbf{k}}$, is defined. From this quaternion it is possible to define a rotation matrix [53]

$$\mathbf{R} = \begin{pmatrix} 1 - 2c^2 - 2d^2 & 2bc - 2ad & 2bd + 2ac \\ 2bc + 2ad & 1 - 2b^2 - 2d^2 & 2cd - 2ab \\ 2bd - 2ac & 2cd + 2ab & 1 - 2b^2 - 2c^2 \end{pmatrix}, \tag{3.44}$$

which is used to rotate all of the beads $\mathbf{n}_{ij}$, with i ranging from 1 to N,

$$\mathbf{n}'_{ij} = \mathbf{R}\mathbf{n}_{ij}. \tag{3.45}$$

The use of a rotation matrix in this case is preferred to quaternion multiplication, described previously, for computational cost considerations. In the case of single bead moves, where

a single rotation is being performed, it takes more computational operations to compute the rotation matrix and then perform a single rotation relative to quaternion conjugation, as quaternion conjugation is approximately as expensive, computationally as generating the rotation matrix and then utilizing the rotation matrix to rotate the vector $\mathbf{n}_{ij}$ is then about half again as computationally expensive. However, when it is possible to reuse the computed rotation matrix multiple times, as in the present case of rigid path displacements, the computational effort of using a rotation matrix to compute new orientations is actually reduced relative to quaternion multiplication, as rotating the molecules via rotation matrix is only about half as computationally expensive as quaternion conjugation.

Regardless of whether a translational or rotational move is performed, the new path is accepted with probability

$$A(\mathbf{P}', \mathbf{P}) = \min\left(\frac{\Psi_{\text{trial}}(\mathbf{X}'_1)}{\Psi_{\text{trial}}(\mathbf{X}_1)}\left(\prod_{i=1}^{M-1}\frac{G_n(\mathbf{X}'_i, \mathbf{X}'_{i+1}, \tau)}{G_n(\mathbf{X}_i, \mathbf{X}_{i+1}, \tau)}\right)\frac{\Psi_{\text{trial}}(\mathbf{X}'_M)}{\Psi_{\text{trial}}(\mathbf{X}_M)}, 1\right), \tag{3.46}$$

with no further generic simplification possible since all slices have now been updated.

If a the path has been broken then it may be advantageous to instead perform a half-path rigid move. This move type proceeds as the normal path move except that in addition to selecting a random particle index, either the left or the right half of the path (slices, 1 to $\lfloor M/2 \rfloor + 1$ or $\lfloor M/2 \rfloor + 1$ to M, respectively) is chosen at random and only that half of the path is updated. In this case the acceptance probability is modified: if the left half of the path has been updated it is

$$A(\mathbf{P}', \mathbf{P}) = \min\left(\frac{\Psi_{\text{trial}}(\mathbf{X}'_1)}{\Psi_{\text{trial}}(\mathbf{X}_1)}\left(\prod_{i=1}^{\lfloor M/2 \rfloor}\frac{G_n(\mathbf{X}'_i, \mathbf{X}'_{i+1}, \tau)}{G_n(\mathbf{X}_i, \mathbf{X}_{i+1}, \tau)}\right), 1\right), \tag{3.47}$$

and if the right half of the path has been updated it is

$$A(\mathbf{P}', \mathbf{P}) = \min\left(\frac{G_n(\tilde{\mathbf{X}}', \mathbf{X}'_{\lfloor M/2 \rfloor + 2}, \tau)}{G_n(\tilde{\mathbf{X}}, \mathbf{X}_{\lfloor M/2 \rfloor + 2}, \tau)}\left(\prod_{i=\lfloor M/2 \rfloor + 2}^{M-1}\frac{G_n(\mathbf{X}'_i, \mathbf{X}'_{i+1}, \tau)}{G_n(\mathbf{X}_i, \mathbf{X}_{i+1}, \tau)}\right)\frac{\Psi_{\text{trial}}(\mathbf{X}'_M)}{\Psi_{\text{trial}}(\mathbf{X}_M)}, 1\right). \tag{3.48}$$

Multi-level bisection moves

The multi-level bisection method is a method for generating new sections of paths in a way that allows for efficient exploration of the space of paths. It does this through the use of a recursive algorithm that allows for early termination of a move proposal if it appears unlikely that the finished move will be accepted [47]. This move type proceeds by selecting at random a particle index, j, and a section of path beginning at slice i and ending at slice $i' = i + 2^l$, where l is the number of levels employed, with the constraint in the case that the path of particle j is cut that $i' \leq \lfloor M/2 \rfloor + 1$ or $i \geq \lfloor M/2 \rfloor + 1$ so that the section of the path to be

updated does not include the center slice, $\lfloor M/2 \rfloor + 1$, except possibly at the ends of the path. The algorithm begins by modifying the center bead in this interval by moving it relative to the average of the end points $\mathbf{X}_{ij}$ and $\mathbf{X}_{i'j}$ and then this new coarse-grained path section is accepted or rejected by the multi-level Metropolis criteria,

$$A_k(x', x) = \min\left(\frac{\pi_k(x')\pi_{k-1}(x)M_k(x)}{\pi_k(x)\pi_{k-1}(x')M_k(x')}, 1\right), \tag{3.49}$$

with k being the level and ranging from 0 to l, $\pi_k(x)$ being the kth level probability, and $M_k(x)$ is the kth level candidate distribution. This interval is recursively bisected until each of the beads $\mathbf{X}_{mj}$, with $i < m < i'$, have been updated or the move has been aborted because of an early rejection. At early levels large displacements of particle position or orientation are attempted and the magnitude of the displacements are ramped down over the course of the attempted move, as will be described below, allowing relatively large changes of the path to be proposed.

The choice of intermediate probability is flexible, and only $\pi_l(x)$ must be the exact probability (or the best approximation available). For intermediate levels it is common to use a rougher, but computationally simpler approximation to the propagator. For example if the final level, l, probability uses a 6th order propagator, $G_6(\tau)$, then a second order propagator, $G_2(\tau)$, might be employed at all levels $k < l$. This greatly speeds up the intermediate levels without impacting the efficiency of the move [47], and retains the higher order behavior for all accepted moves.

A cartoon of this algorithm is depicted in figure 3.2. It is seen that first the entire path section is bisected, allowing for a large displacement of the bead at the center of the path segment being updated. After this is accepted, two smaller bisections are performed, with slightly smaller displacements. In each case the displacement is from the midpoint of the spatial coordinates of the two beads at the ends of each sub-segment of path, joined by dashed lines. If this type of path update is successful at each level then the resulting updated path will differ significantly from the starting path, as depicted in figure 3.2.

The 0th level move

In the case that either $i = 1$ or $i + 2^l = M$, a 0th level move is attempted. In case of a translational move a random d-dimensional vector, $\mathbf{v}$, is generated by sampling the d components from a normal distribution $\mathcal{N}(0, \sigma_0^2 = 2^l\tau\lambda)$, where $\lambda = \hbar^2/(2m)$ for molecules of mass m. If the orientation is to be updated then a unit quaternion, $\mathbf{q} = \cos\theta/2 + \hat{\mathbf{v}}\sin\theta/2$, is generated, where $\hat{\mathbf{v}}$ is a random unit vector fulfilling the condition $\hat{\mathbf{v}} \cdot \mathbf{n}_{m,j} = 0$, m being either 1 or $i + 2^l$ depending on the slice to be updated, and θ is chosen from the normal distribution $\mathcal{N}(0, \sigma_0^2 = 2^l\tau B)$ subject to the constraint that $\theta \leq \pi$, where $B = h/(8\pi^2 I)$ is the rotational constant of the linear molecules being simulated. If $i = 1$ then the new path with

$$\mathbf{r}'_{1j} = \mathbf{r}_{1j} + \mathbf{v} \tag{3.50}$$

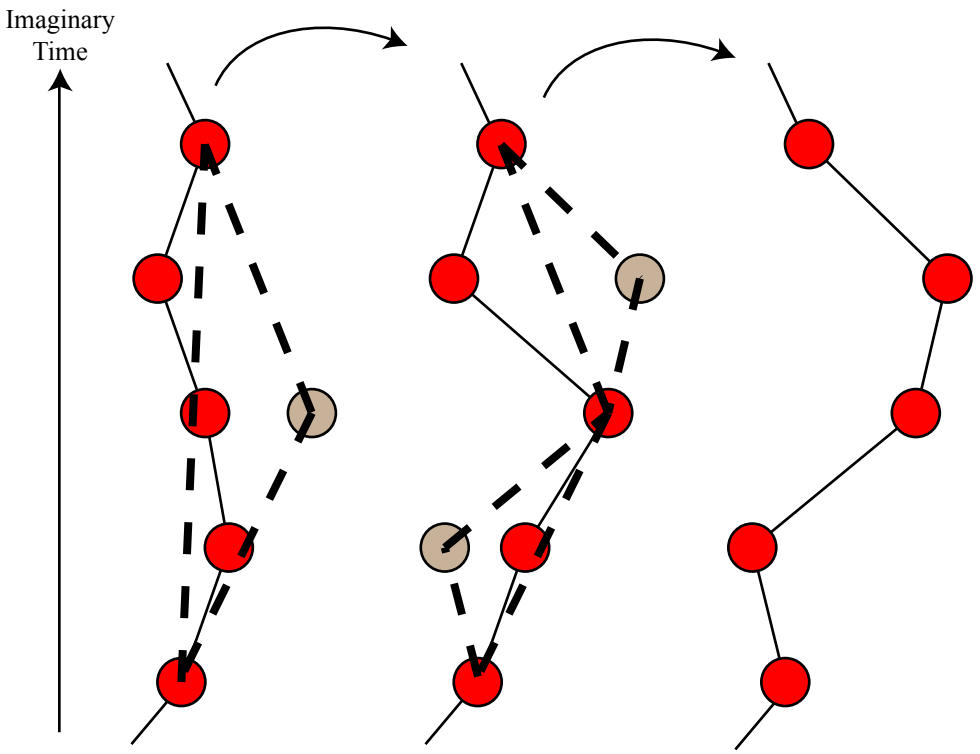

Figure 3.3: Cartoon of a two level bisection algorithm in action. The red disks represent the coordinates of the particles while the grey disks represent the proposed new positions based on the bisection procedure at each level.

or

$$\mathbf{n}'_{1j} = \mathbf{q}(\mathbf{n}_{1j})\mathbf{q}^{-1} \tag{3.51}$$

is accepted with probability

$$A(\mathbf{P}', \mathbf{P}) = \min\left(\frac{\Psi_{\text{trial}}(\mathbf{X}'_1)G_2(\mathbf{X}'_1, \mathbf{X}_{2^l+1}, 2^l\tau)}{\Psi_{\text{trial}}(\mathbf{X}_1)G_2(\mathbf{X}_1, \mathbf{X}_{2^l+1}, 2^l\tau)}, 1\right) \tag{3.52}$$

otherwise if $i + 2^l = M$ then the new path with

$$\mathbf{r}'_{Mj} = \mathbf{r}_{Mj} + \mathbf{v} \tag{3.53}$$

or

$$\mathbf{n}'_{Mj} = \mathbf{q}(\mathbf{n}_{Mj})\mathbf{q}^{-1} \tag{3.54}$$

is accepted with probability

$$A(\mathbf{P}', \mathbf{P}) = \min\left(\frac{G_2(\mathbf{X}_{M-2^l}, \mathbf{X}'_M, 2^l\tau)\Psi_{\text{trial}}(\mathbf{X}'_M)}{G_2(\mathbf{X}_{M-2^l}, \mathbf{X}_M, 2^l\tau)\Psi_{\text{trial}}(\mathbf{X}_M)}, 1\right). \tag{3.55}$$

If the path of particle j has been cut, then an additional 0th level move of one of the center time slices is possible. If the end of the path section to be updated is $i' = \lfloor M/2 \rfloor + 1$ then a new configuration is generated by

$$\mathbf{r}'_{i'j} = \mathbf{r}_{i'j} + \mathbf{v} \tag{3.56}$$

or

$$\mathbf{n}'_{i'j} = \mathbf{q}(\mathbf{n}_{i'j})\mathbf{q}^{-1} \tag{3.57}$$

for translation and rotational moves, respectively, and accepted with probability

$$A(\mathbf{P}', \mathbf{P}) = \min\left(\frac{G_2(\mathbf{X}_{\lfloor M/2 \rfloor + 1 - 2^l}, \mathbf{X}'_{\lfloor M/2 \rfloor + 1}, 2^l\tau)}{G_2(\mathbf{X}_{\lfloor M/2 \rfloor + 1 - 2^l}, \mathbf{X}_{\lfloor M/2 \rfloor + 1}, 2^l\tau)}, 1\right). \tag{3.58}$$

Otherwise, if the beginning of the path section to be updated is $i = \lfloor M/2 \rfloor + 1$ then the new configuration is

$$\tilde{\mathbf{r}}'_j = \tilde{\mathbf{r}}_j + \mathbf{v} \tag{3.59}$$

or

$$\tilde{\mathbf{n}}'_j = \mathbf{q}(\tilde{\mathbf{n}}_j)\mathbf{q}^{-1} \tag{3.60}$$

for translational and rotational moves, respectively, accepted with probability

$$A(\mathbf{P}', \mathbf{P}) = \min\left(\frac{G_2(\tilde{\mathbf{X}}', \mathbf{X}_{\lfloor M/2 \rfloor + 1 + 2^l}, 2^l\tau)}{G_2(\tilde{\mathbf{X}}, \mathbf{X}_{\lfloor M/2 \rfloor + 1 + 2^l}, 2^l\tau)}, 1\right). \tag{3.61}$$

If neither of the ends of the path section to be updated are fall at the ends of the path (or the center of the path for cut path simulations) then the 0th level move is automatically accepted with unit probability, since no degrees of freedom are changed in the case. If the 0th level move is rejected then the entire move is rejected and a new trial move is generated from scratch (generating new slice ranges and particle index, *etc.*) otherwise a $k(=1)$th level move is attempted.

The kth level moves

If the 0th level move was accepted then moves of level $k = 1, \ldots, l-1$ are performed. For the kth level move, slices $\mathbf{X}_p$, with $p = s \ldots 2^l - s$ in steps of $2s$, where $s = 2^{l-k}$, are updated. For translational moves this is accomplished by generating a random d-dimensional vector, $\mathbf{v}$, where each of the d components are sampled from the normal distribution $\mathcal{N}(0, \sigma_k^2 = 2^{l-k}\tau\lambda)$. In the case of a rotational update, a unit quaternion, $\mathbf{q} = \cos\theta/2 + \hat{\mathbf{v}}\sin\theta/2$, is generated, where $\hat{\mathbf{v}}$ is a random unit vector fulfilling the condition $\hat{\mathbf{v}} \cdot \mathbf{n}'_{\text{avg}} = 0$, with

$$\mathbf{n}'_{\text{avg}} = \frac{\mathbf{n}'_{(p-s)j} + \mathbf{n}'_{(p+s)j}}{||\mathbf{n}'_{(p-s)j} + \mathbf{n}'_{(p+s)j}||}, \tag{3.62}$$

and θ is sampled from the normal distribution $\mathcal{N}(0, \sigma_k^2 = 2^{l-k}\tau B)$, subject to the constraint that $\theta < \pi$. Then for each of these slices, $\mathbf{X}_p$, is updated by generating a new configuration with

$$\mathbf{r}'_{pj} = \mathbf{r}'_{\text{avg}} + \mathbf{v}, \tag{3.63}$$

where

$$\mathbf{r}'_{\text{avg}} = \frac{1}{2}(\mathbf{r}'_{(p-s)j} + \mathbf{r}'_{(p+s)j}) \tag{3.64}$$

is the average position, in the case of a translational move and

$$\mathbf{n}'_{pj} = \mathbf{q}(\mathbf{n}'_{\text{avg}})\mathbf{q}^{-1} \tag{3.65}$$

in the case of rotational moves, again with $\mathbf{n}'_{\text{avg}}$ taken to be the normalized average orientation. The acceptance probability of the kth level move is

$$A_k(\mathbf{P}', \mathbf{P}) = \min\left(\prod_{p=0}^{2^{k-1}-1} \frac{G_2(\mathbf{X}_{i+2sp}, \mathbf{X}_{i+2s(p+1)}, 2s\tau)}{G_2(\mathbf{X}'_{i+2sp}, \mathbf{X}'_{i+2s(m+1)}, 2s\tau)} \times \prod_{p'=0}^{2^k-1} \frac{G_2(\mathbf{X}'_{i+sp'}, \mathbf{X}'_{i+s(p'+1)}, s\tau)}{G_2(\mathbf{X}_{i+sp'}, \mathbf{X}_{i+s(p'+1)}, s\tau)} \prod_{p''=0}^{2^{k-1}-1} \frac{M_k(\mathbf{X}_{i+s+2sp''})}{M_k(\mathbf{X}'_{i+s+2sp''})}, 1\right) \tag{3.66}$$

with $\tilde{\mathbf{X}}$ substituted where appropriate (*i.e.*, when there is a cut path and the beginning of the updated path section is the center slice). Note that in this case, because new candidate paths are proposed by displacing a bead from the average position, or orientation in the case of orientational moves, and not from the current path directly, the candidate generating distribution is not symmetric and so it must appear in eq. (3.66). In the case of a translational move the candidate generating distribution, $M_k(\mathbf{X})$, is

$$M_k(\mathbf{X}_p) = (2\pi\sigma_k^2)^{-d/2} e^{-(\mathbf{r}_{pj} - \mathbf{r}_{\text{avg}})^2/(2\sigma_k^2)}, \tag{3.67}$$

i.e. the PDF of a d-dimensional normal distribution centered around $\mathbf{r}_{\text{avg}}$, and in the case of a rotational move $M_k(\mathbf{X})$ is

$$M_k(\mathbf{X}_p) = \frac{(2\pi\sigma_k^2)^{-1/2} e^{-(\arccos(\mathbf{n}_{pj}\cdot\mathbf{n}_{\text{avg}}))^2/(2\sigma_k^2)}}{\sin(\arccos(\mathbf{n}_{pj}\cdot\mathbf{n}_{\text{avg}}))}, \tag{3.68}$$

which is the distribution of new orientations obtained from quaternion conjugation as described above. If the kth level move is rejected then the entire move is rejected and a new move is attempted from scratch (picking a new range of slices and particle index, *etc.*). If the kth level move is accepted then the final level move is attempted.

The final level move

The final level proceeds in much the same way as the rest of the $1 \leq k < l$ levels, with new candidate configurations generated in the same way but now setting $k = l$. The only significant change is in the acceptance probability, where the lower accuracy propagator approximation employed for the other levels is now replaced with the best approximation available so that the convergence behavior of computed expectation values with respect to τ (see section 3.1) is of higher order than the lower order (but less computationally demanding) approximation used in the intermediate steps. In the case that the best available approximation is $G_n(\tau)$ and a second order approximation, $G_2(\tau)$, has been used for the rest of the levels, the final acceptance ratio for the entire move is

$$A_l(\mathbf{P}', \mathbf{P}) = \min \left(\prod_{p=0}^{2^{l-1}-1} \frac{G_2(\mathbf{X}_{i+2p}, \mathbf{X}_{i+2(p+1)}, 2\tau)}{G_2(\mathbf{X}'_{i+2p}, \mathbf{X}'_{i+2(p+1)}, 2\tau)} \times \prod_{p'=i}^{2^l-1} \frac{G_n(\mathbf{X}'_{p'}, \mathbf{X}'_{p'+1}, \tau)}{G_n(\mathbf{X}_{p'}, \mathbf{X}_{p'+1}, \tau)} \prod_{p''=0}^{2^{l-1}-1} \frac{M_k(\mathbf{X}_{i+1+2p''})}{M_k(\mathbf{X}'_{i+1+2p''})}, 1 \right). \quad (3.69)$$

3.3 Propagators

One of the most crucial elements in any path integral-based simulation is a suitable short-time approximation to the propagator, $G_n(\tau)$. This together with the value of the corresponding imaginary-time step, τ, determines the accuracy of the simulation. The quality of the approximation will determine how large an imaginary-time step can be employed. Since at low temperatures or for the ground state, the total propagation period in imaginary time, β, must be long and computational complexity increases linearly with the number of time slices, then it is clearly advantageous to be able to use as long a time step as is feasible, in order to decrease the number of time slices.

Since it is impossible to write down a numerically usable definition of the propagator without being able to diagonalize the full Hamiltonian (the precise reason that a short-time approximation is necessary in the first place) it is clear that obtaining an accurate and efficient approximation to the imaginary time propagator is the principal challenge for implementing the PIGS method efficiently. The quantum mechanical propagator (in imaginary time) is of the form

$$G(\tau) = e^{-\tau H/\hbar} = e^{-\tau(T+V)/\hbar} = \sum_{k=0}^{\infty} \frac{1}{k!} \left(-\frac{\tau}{\hbar} \right)^k (T+V)^k, \quad (3.70)$$

where in general $[T, V] \neq 0$. The simplest approximation is based on splitting the propagator as

$$G_1(\tau) = e^{-\tau T/\hbar} e^{-\tau V/\hbar} = G_0(\tau) e^{-\tau V/\hbar} = G(\tau) + O(\tau^2), \quad (3.71)$$

where $G_0(\tau) = e^{-\tau T/\hbar}$ is the free-particle propagator. By Taylor expanding this operator and comparing to the exact expression it is clear that the leading order error term is $O(\tau^2)$, except in the exceptional case where the operators T and V commute, in which case the formula is exact. Another well known splitting, which forms the basis of the "any-order" propagator utilized in this work [55], is

$$G_2(\tau) = e^{-\tau V/2\hbar} e^{-\tau T/\hbar} e^{-\tau V/2\hbar} = e^{-\tau V/2\hbar} G_0(\tau) e^{-\tau V/2\hbar} = G(\tau) + O(\tau^3), \tag{3.72}$$

which is one order better than eq. (3.71), without requiring the evaluation of anything other than the kinetic energy and potential propagators. This approximation will be referred to hereafter as the primitive approximation. Higher order approximations in this spirit require the evaluation of not only the potential energy and the free-particle propagators but also $[V,[T,V]] = |\nabla V|^2$, *e.g.*, the fourth-order Trotter-Suzuki propagator [56] and related factorizations [57].

In this work a different type of operator splitting was utilized, referred to as an "any-order" propagator here, which is based on a decomposition of the form [55]

$$G_{2n}(\tau) = \sum_{i=1}^{n} c_i \left(G_2(\tau/k_i)\right)^{k_i} = G(\tau) + O(\tau^{2n+1}), \tag{3.73}$$

where $k_i \in \mathbb{W}$ are a set of whole numbers which can be chosen arbitrarily and the coefficients are

$$c_i = \prod_{j \neq i} \frac{k_i^2}{k_i^2 - k_j^2}. \tag{3.74}$$

The intervals, k_i can be chosen at will, but it is convenient to use sequences such that all of the smaller intervals are factors of the largest interval, for example in this work the sequence $k_i = \{1, 2, 4\}$, which generates a 6th order propagator, was employed. This "any-order" propagator allows the evaluation, in theory, of arbitrarily high order approximations to the propagator, with the caveat that in this case $G_{2n}(\tau)$ may not be strictly positive, especially if the time step is too large. This occurs because while $G_2(\tau)$ is strictly positive, sums of products of $G_2(\tau)$ at the different size time steps, as in eq. (3.73), will not necessarily be strictly positive, but will be only "mostly positive" for sufficiently small τ [55]. If this occurs the entire move should be rejected when determining whether or not to accept a move based on the evaluation of $A(\mathbf{P}', \mathbf{P})$, as in the Metropolis algorithm described above. In addition care should be taken to choose time step small enough that the fraction of propagator evaluations which yield negative values is not too large.

Evaluating the propagator is accomplished through inserting factors of the identity so that, *e.g.*

$$G_2(\mathbf{X}_1, \mathbf{X}_2, \tau) = e^{-\tau(V(\mathbf{X}_1)+V(\mathbf{X}_2))/(2\hbar)} G_0(\mathbf{X}_1, \mathbf{X}_2, \tau) \tag{3.75}$$

in the case of the second order primitive approximation. The case of the "any-order" propagator is slightly more involved. For illustration, the 6th order propagator is

$$\begin{aligned} G_6(\mathbf{X}_1,\mathbf{X}_5,4\tau) = & \frac{1}{45}e^{-2\tau(V(\mathbf{X}_1)+V(\mathbf{X}_5))/\hbar}G_0(\mathbf{X}_1,\mathbf{X}_5,4\tau) \\ & -\frac{4}{9}e^{-\tau(V(\mathbf{X}_1)+2V(\mathbf{X}_3)+V(\mathbf{X}_5))/\hbar}G_0(\mathbf{X}_1,\mathbf{X}_3,2\tau)G_0(\mathbf{X}_3,\mathbf{X}_5,2\tau) \\ & +\frac{64}{45}\left(e^{-\tau(V(\mathbf{X}_1)+2V(\mathbf{X}_2)+2V(\mathbf{X}_3)+2V(\mathbf{X}_4)+V(\mathbf{X}_5))/(2\hbar)}\right. \\ & \left.\times G_0(\mathbf{X}_1,\mathbf{X}_2,\tau)G_0(\mathbf{X}_2,\mathbf{X}_3,\tau)G_0(\mathbf{X}_3,\mathbf{X}_4,\tau)G_0(\mathbf{X}_4,\mathbf{X}_5,\tau)\right), \end{aligned} \tag{3.76}$$

which can be further simplified to

$$\begin{aligned} G_6(\mathbf{X}_1,\mathbf{X}_5,4\tau) = & G_0(\mathbf{X}_1,\mathbf{X}_2,\tau)G_0(\mathbf{X}_2,\mathbf{X}_3,\tau)G_0(\mathbf{X}_3,\mathbf{X}_4,\tau)G_0(\mathbf{X}_4,\mathbf{X}_5,\tau) \\ & \times\left(\frac{1}{45}e^{-2\tau(V(\mathbf{X}_1)+V(\mathbf{X}_5))/\hbar}\right. \\ & -\frac{4}{9}e^{-\tau(V(\mathbf{X}_1)+2V(\mathbf{X}_3)+V(\mathbf{X}_5))/\hbar} \\ & \left.+\frac{64}{45}e^{-\tau(V(\mathbf{X}_1)+2V(\mathbf{X}_2)+2V(\mathbf{X}_3)+2V(\mathbf{X}_4)+V(\mathbf{X}_5))/(2\hbar)}\right) \end{aligned} \tag{3.77}$$

by breaking up all of the free propagators. Similar expressions can be derived for other orders of the "any-order" propagator, eq. (3.73).

Free particle propagator

The potential energy portion of the propagator is relatively easy to evaluate since the potential energy operator is already diagonal in the representation of choice for PIGS simulations, which is the position representation. The kinetic energy portion, *i.e.* the free-particle propagator, on the other hand, is more complicated and depends on the nature of the degrees of freedom being simulated. In general, the propagator can be written as

$$G(\tau) = \sum_i e^{-\tau E_i/\hbar}|\phi_i\rangle\langle\phi_i|, \tag{3.78}$$

where $\sum_i \to \int dE$ in the case of continuous spectra and E_i is the eigenenergy of the ith eigenstate of H. To evaluate the free-particle propagator it is necessary to evaluate matrix elements of the form $\langle\mathbf{X}'|G(\tau)|\mathbf{X}\rangle$, with $H = T$ (*i.e.*, the Hamiltonian is only the kinetic energy operator).

In the case of N molecules, each with mass m, with only translational degrees of freedom in d-dimensions (here $d = 1, 2$ or 3) the Hamiltonian is

$$T_{\text{trans}} = \sum_{i=1}^{N}\frac{\mathbf{p}_i^2}{2m}, \tag{3.79}$$

which gives the expression, after insertion of the identity $\mathbb{I} = \int_{\text{all}} d^d\mathbf{p}\,|\mathbf{p}\rangle\langle\mathbf{p}|$ and using $\langle\mathbf{r}|\mathbf{p}\rangle = (2\pi\hbar)^{-d/2}e^{i\mathbf{p}\cdot\mathbf{r}/\hbar}$

$$\begin{aligned} G_0^{(T)}(\mathbf{R},\mathbf{R}',\tau) &= \left(\frac{1}{2\pi\hbar}\right)^{Nd}\prod_{i=1}^{N}\int_{\text{all}}\int_{\text{all}} d^d\mathbf{p}_i\,d^d\mathbf{p}_i'\,e^{i(\mathbf{p}_i\cdot\mathbf{r}_i-\mathbf{p}_i'\cdot\mathbf{r}_i')/\hbar}e^{-\tau\lambda\mathbf{p}_i^2/\hbar}\delta(\mathbf{p}_i-\mathbf{p}_i') \\ &= \left(\frac{1}{2\pi\hbar}\right)^{Nd}\prod_{i=1}^{N}\int_{\text{all}} d^d\mathbf{p}_i\,e^{i\mathbf{p}_i\cdot(\mathbf{r}_i-\mathbf{r}_i')/\hbar}e^{-\tau\lambda\mathbf{p}_i^2/\hbar}, \end{aligned} \tag{3.80}$$

where $\lambda = \hbar^2/(2m)$. Evaluating this product of Gaussian integrals leads to the well-known expression (see, for example, reference [58])

$$G_0^{(T)}(\mathbf{R},\mathbf{R}',\tau) = \left(\frac{\hbar}{4\pi\lambda\tau}\right)^{Nd/2}\prod_{i=1}^{N}e^{-\hbar\,(\mathbf{r}_i-\mathbf{r}_i')^2/(4\lambda\tau)}. \tag{3.81}$$

In the case of particles with purely rotational degrees of freedom in 3-dimensions (stationary rigid rotors), the Hamiltonian is

$$T_{\text{rot}} = \sum_{i=1}^{N}\frac{\mathbf{L}_i^2}{2I}, \tag{3.82}$$

is more complicated in that no closed-form expression exists for the free-particle propagator. The expression for the free-particle propagator in can be obtained here by using the eigenfunctions and eigenenergies of the rigid rotor Hamiltonian, eq. (2.21), and using the fact that $Y_l^m(\mathbf{n}) \equiv Y_l^m(\theta,\phi) = \langle\theta,\phi|lm\rangle$, to yield the expression

$$G_0^{(R)}(\mathbf{N},\mathbf{N}',\tau) = \prod_{i=1}^{N}\sum_{l=0}^{\infty}e^{-2\pi\tau Bl(l+1)}\sum_{m=-l}^{l}Y_l^m(\mathbf{n}_i)Y_l^{m*}(\mathbf{n}_i'). \tag{3.83}$$

By using the spherical harmonic addition theorem [36],

$$\sum_{m=-l}^{l}Y_l^m(\mathbf{n})Y_l^{m*}(\mathbf{n}') = \frac{2l+1}{4\pi}P_l(\mathbf{n}\cdot\mathbf{n}'), \tag{3.84}$$

where $P_l(x)$ is the Legendre polynomial of degree l, it is possible to simplify this expression for the propagator to [59]

$$G_0^{(R)}(\mathbf{N},\mathbf{N}',\tau) = \prod_{i=1}^{N}\sum_{l=0}^{\infty}\frac{2l+1}{4\pi}P_l(\mathbf{n}_i\cdot\mathbf{n}_i')e^{-2\pi\tau Bl(l+1)}. \tag{3.85}$$

In order to make use of this expression it is most convenient to tabulate values before a simulation on a sufficiently fine grid in $\cos(\theta) = \mathbf{n}\cdot\mathbf{n}'$ and with a sufficiently high maximum

value for l, and then use an interpolation during the course of the simulation to evaluate $G_0^{(R)}(\mathbf{N}, \mathbf{N}', \tau)$.

The case of both translational and rotational degrees of freedom is easy, since $[T_{\rm trans}, T_{\rm rot}] = 0$ so that rotations are unaffected by center-of-mass translations of the particles. In this final case the free-particle propagator for translations and rotations is simply the product of the two propagators, $G_0(\mathbf{X}, \mathbf{X}', \tau) = G_0^{(T)}(\mathbf{R}, \mathbf{R}', \tau) G_0^{(R)}(\mathbf{N}, \mathbf{N}', \tau)$.

Chapter 4

Feynman excitation spectrum for particles with rotational degrees of freedom

The Bijl-Feynman approximation for the elementary excitation spectrum, which was originally derived for homogeneous many-body systems of structureless particles [33, 34], is one of the simplest theories for calculating elementary excitation energies in such systems. Owing to its simplicity and the fact that it only depends on the Fourier transform of the pair distribution function, this approximate excitation spectrum can be evaluated using standard quantum Monte Carlo methods. The following derivation for homogeneous gases of rigid rotors follows Feynman's derivation for structureless particles very closely [34].

The Hamiltonian describing a homogeneous system of N interacting rotating particles in 3 dimensions is (relative to the ground state energy, E_0, of the system)

$$H = \sum_{i=1}^{N} \frac{\mathbf{p}_i^2}{2m} + \sum_{i=1}^{N} \frac{\mathbf{L}_i^2}{2I} + V(\mathbf{X}) - E_0, \tag{4.1}$$

where $V(\mathbf{X})$ is the potential energy operator of the system. The ground state many-body wave function of this Hamiltonian is $\Phi(\mathbf{X})$ and satisfies

$$H\Phi(\mathbf{X}) = 0, \tag{4.2}$$

which is a function of all of the coordinates of the system, $\mathbf{X} \equiv \{\mathbf{x}_1, \ldots, \mathbf{x}_N\}$ and $\mathbf{x}_i \equiv \{\mathbf{r}_i, \mathbf{n}_i\}$. The ground state wave function is taken to be real valued and so $\rho(\mathbf{X}) = \Phi(\mathbf{X})^2$. In keeping with Feynman's argument [33, 34] it is assumed that the excited state wave function can be expressed as

$$\Psi(\mathbf{X}) = F(\mathbf{X})\Phi(\mathbf{X}) = \Phi(\mathbf{X}) \sum_{i=1}^{N} f(\mathbf{x}_i), \tag{4.3}$$

where $F(\mathbf{X})$ is some function of all of the coordinates of the system to be determined. By utilizing the product rule and eq. (4.2) the Hamiltonian acting on the wave function in eq. (4.3) can be written as

$$H\Psi(\mathbf{X}) = \frac{1}{\Phi(\mathbf{X})}\left(-\frac{\hbar^2}{2m}\sum_{i=1}^{N}\nabla_i^{(s)}\cdot\rho(\mathbf{X})\nabla_i^{(s)}F(\mathbf{X}) - \frac{\hbar^2}{2I}\sum_{i=1}^{N}\nabla_i^{(o)}\cdot\rho(\mathbf{X})\nabla_i^{(o)}F(\mathbf{X})\right), \quad (4.4)$$

in which $\nabla_i^{(o)}$ is used to denote the divergence and gradient with respect to the orientation of particle i so that

$$\nabla^{(o)}\cdot f(\theta,\phi)\nabla^{(o)}g(\theta,\phi) = \frac{1}{\sin\theta}\frac{\partial}{\partial\theta}\sin\theta f(\theta,\phi)\frac{\partial}{\partial\theta}g(\theta,\phi) + \frac{1}{\sin^2\theta}\frac{\partial}{\partial\phi}f(\theta,\phi)\frac{\partial}{\partial\phi}g(\theta,\phi), \quad (4.5)$$

$\nabla_i^{(s)}$ denotes the spatial divergence and gradient so that

$$\begin{aligned}\nabla^{(s)}\cdot f(x,y,z)\nabla^{(s)}g(x,y,z) = &\frac{\partial}{\partial x}f(x,y,z)\frac{\partial}{\partial x}g(x,y,z)\\ &+\frac{\partial}{\partial y}f(x,y,z)\frac{\partial}{\partial y}g(x,y,z) + \frac{\partial}{\partial z}f(x,y,z)\frac{\partial}{\partial z}g(x,y,z), \quad (4.6)\end{aligned}$$

and $\Delta^{(x)} = \nabla^{(x)}\cdot\nabla^{(x)}$, with $x = o$ or s is the Laplacian for the orientational and spatial coordinates, respectively. It should be noted that while the expression in eq. (4.4) does not explicitly depend on $V(\mathbf{X})$, having used eq. (4.2) to simplify terms arising from the product rule like

$$F(\mathbf{X})\left(\sum_{i=1}^{N}-\frac{\hbar^2}{2m}\Delta_i^{(s)} + \sum_{i=1}^{N}-\frac{\hbar^2}{2I}\Delta_i^{(o)} + V(\mathbf{X}) - E_0\right)\Phi(\mathbf{X}) = F(\mathbf{X})\left(H\Phi(\mathbf{X})\right) = 0, \quad (4.7)$$

the expression for the excited state energy that is the result of this analysis will implicitly depend on $V(\mathbf{X})$ through its influence on the structure of the ground state wave function, $\Phi(\mathbf{X})$ and hence on $\rho(X)$. The energy will be determined variationally by minimizing the integral

$$\begin{aligned}\mathcal{E} = &\int_A d^N\mathbf{X}\ \Psi^*(\mathbf{X})H\Psi(\mathbf{X}) \quad (4.8)\\ =&\frac{\hbar^2}{2m}\sum_{i=1}^{N}\int_A d^N\mathbf{X}\ \left(\nabla_i^{(s)}f^*(\mathbf{x}_i)\right)\cdot\left(\nabla_i^{(s)}f(\mathbf{x}_i)\right)\rho(\mathbf{X})\\ &+\frac{\hbar^2}{2I}\sum_{i=1}^{N}\int_A d^N\mathbf{X}\ \left(\nabla_i^{(o)}f^*(\mathbf{x}_i)\right)\cdot\left(\nabla_i^{(o)}f(\mathbf{x}_i)\right)\rho(\mathbf{X}), \quad (4.9)\end{aligned}$$

where $\int_A$ means integrating over all space (and all angles). The constraint on this minimization is the normalization integral

$$\mathcal{G} = \int_A d^N\mathbf{X}\ F^*(\mathbf{X})F(\mathbf{X})\rho(\mathbf{X}) = \sum_{i=1}^{N}\sum_{j=1}^{N}\int_A d^N\mathbf{X}\ f^*(\mathbf{x}_i)f(\mathbf{x}_j)\rho(\mathbf{X}) \quad (4.10)$$

so that the energy is $E = \mathcal{E}/\mathcal{G}$. These expressions can be further simplified by introducing the two body reduced density

$$\rho^{(2)}(\mathbf{x}_1', \mathbf{x}_2') = \sum_{i=1}^{N} \sum_{j \neq i} \int_A d^N\mathbf{X}\ \delta(\mathbf{x}_i - \mathbf{x}_1')\delta(\mathbf{x}_j - \mathbf{x}_2')\rho(\mathbf{X}) \tag{4.11}$$

and the one body reduced density

$$\rho^{(1)}(\mathbf{x}_1') = \sum_{i=1}^{N} \int_A d^N\mathbf{X}\ \delta(\mathbf{x}_i - \mathbf{x}_1')\rho(\mathbf{X}). \tag{4.12}$$

Inserting these reduced densities into eq. (4.9) and eq. (4.10) results in

$$\mathcal{E} = \frac{\hbar^2}{2m} \int_A d\mathbf{x}\ \rho^{(1)}(\mathbf{x}) \nabla^{(s)} f^*(\mathbf{x}) \cdot \nabla^{(s)} f(\mathbf{x}) + \frac{\hbar^2}{2I} \int_A d\mathbf{x}\ \rho^{(1)}(\mathbf{x}) \nabla^{(o)} f^*(\mathbf{x}) \cdot \nabla^{(o)} f(\mathbf{x}) \tag{4.13}$$

and

$$\mathcal{G} = \int_A d\mathbf{x}\, d\mathbf{x}'\ f^*(\mathbf{x}) f(\mathbf{x}') \rho^{(2)}(\mathbf{x}, \mathbf{x}') + \int_A d\mathbf{x}\ |f(\mathbf{x})|^2 \rho^{(1)}(\mathbf{x}) \tag{4.14}$$

respectively.

The goal is to extremize $\mathcal{E} = \int d\mathbf{x}\ \mathcal{L}$ subject to the constraint $\mathcal{G} = \int d\mathbf{x}\ g = 1$. This is done by using the calculus of variations and defining the function

$$\begin{aligned} u =& \mathcal{L} + \lambda g \\ =& \frac{\hbar^2}{2m} \rho^{(1)}(\mathbf{x}) \nabla^{(s)} f^*(\mathbf{x}) \cdot \nabla^{(s)} f(\mathbf{x}) + \frac{\hbar^2}{2m} \rho^{(1)}(\mathbf{x}) \nabla^{(o)} f^*(\mathbf{x}) \cdot \nabla^{(o)} f(\mathbf{x}) \\ & + \lambda \left(\int_A d\mathbf{x}'\ \rho^{(2)}(\mathbf{x}, \mathbf{x}') f^*(\mathbf{x}) f(\mathbf{x}') + \rho^{(1)}(\mathbf{x}) f^*(\mathbf{x}) f(\mathbf{x}) \right), \end{aligned} \tag{4.15}$$

which satisfies a system of Euler-Lagrange equations (for a derivation see, *e.g.*, reference [60]). In particular the equation for $f(\mathbf{x})$ is given by

$$\lambda \int_A d\mathbf{x}'\ \rho^{(2)}(\mathbf{x}, \mathbf{x}') f(\mathbf{x}') + \lambda \frac{\rho_0}{4\pi} f(\mathbf{x}) - \frac{\hbar^2}{2m} \frac{\rho_0}{4\pi} \Delta^{(s)} f(\mathbf{x}) - \frac{\hbar^2}{2I} \frac{\rho_0}{4\pi} \Delta^{(o)} f(\mathbf{x}) = 0, \tag{4.16}$$

where the fact that for homogeneous systems $\rho^{(1)}(\mathbf{x}) = \rho_0/4\pi$ has been used. This can also be written as

$$\lambda \left(\frac{\rho_0}{4\pi} \right)^2 h(\mathbf{x}) + \lambda \frac{\rho_0}{4\pi} f(\mathbf{x}) - \frac{\hbar^2}{2m} \frac{\rho_0}{4\pi} \Delta^{(s)} f(\mathbf{x}) - \frac{\hbar^2}{2I} \frac{\rho_0}{4\pi} \Delta^{(o)} f(\mathbf{x}) = 0, \tag{4.17}$$

in which the function

$$h(\mathbf{x}) = \int_A d\mathbf{x}'\ g(\mathbf{r} - \mathbf{r}', \mathbf{n}, \mathbf{n}') f(\mathbf{x}') \tag{4.18}$$

has been defined for simplicity. Here the definition

$$\rho^{(2)}(\mathbf{x}_1, \mathbf{x}_2) = \left(\frac{\rho_0}{4\pi}\right)^2 g(\mathbf{r}_1 - \mathbf{r}_2, \mathbf{n}_1, \mathbf{n}_2) \tag{4.19}$$

for $g(\mathbf{r}_1 - \mathbf{r}_2, \mathbf{n}_1, \mathbf{n}_2)$, the molecular pair distribution function, has been used.

To make further progress the (spatial) Fourier transform of eq. (4.17) must be taken. Replacing $\lambda = -E$ and using the cross-correlation theorem [61],

$$\text{F.T.}\left[\int_{-\infty}^{\infty} dy\ f^*(y)g(x+y)\right](k) = \tilde{f}^*(k)\tilde{g}(k), \tag{4.20}$$

to simplify the Fourier transform of $h(\mathbf{x})$ leads to

$$\begin{aligned} 0 = &- E\left[\left(\frac{\rho_0}{4\pi}\right)^2 \int_O d\mathbf{n}'\ \tilde{g}(\mathbf{k}, \mathbf{n}, \mathbf{n}')\tilde{f}(\mathbf{k}, \mathbf{n}') + \frac{\rho_0}{4\pi}\tilde{f}(\mathbf{k}, \mathbf{n})\right] + \frac{\rho_0}{4\pi}\frac{\hbar^2 k^2}{2m}\tilde{f}(\mathbf{k}, \mathbf{n}) \\ &- \frac{\rho_0}{4\pi}\frac{\hbar^2}{2I}\Delta^{(o)}\tilde{f}(\mathbf{k}, \mathbf{n}), \end{aligned} \tag{4.21}$$

where here $\int_O d\mathbf{n}' \equiv \int_0^\pi d\theta\, \sin\theta \int_0^{2\pi} d\phi$ denotes integration over the orientation of $\mathbf{n}'$. The functions $\tilde{f}(\mathbf{k}, \mathbf{n})$ and $\tilde{g}(\mathbf{k}, \mathbf{n}, \mathbf{n}')$ can then be expanded in the basis of spherical harmonics. The expansion of $\tilde{f}(\mathbf{k}, \mathbf{n})$ is straight-forward and gives

$$\begin{aligned} 0 = &- E\left[\left(\frac{\rho_0}{4\pi}\right)^2 \int_O d\mathbf{n}'\ \tilde{g}(\mathbf{k}, \mathbf{n}, \mathbf{n}') \sum_{l_2}\sum_{m_2} \tilde{f}_{l_2}^{m_2}(\mathbf{k}) Y_{l_2}^{m_2}(\mathbf{n}') + \frac{\rho_0}{4\pi}\sum_{l_1}\sum_{m_1}\tilde{f}_{l_1}^{m_1}(\mathbf{k})Y_{l_1}^{m_1}(\mathbf{n})\right] \\ &+ \frac{\rho_0}{4\pi}\frac{\hbar^2 k^2}{2m}\sum_{l_1}\sum_{m_1}\tilde{f}_{l_1}^{m_1}(\mathbf{k})Y_{l_1}^{m_1}(\mathbf{n}) + \frac{\rho_0}{4\pi}\frac{\hbar^2}{2I}\sum_{l_1}\sum_{m_1} l_1(l_1+1)\tilde{f}_{l_1}^{m_1}(\mathbf{k})Y_{l_1}^{m_1}(\mathbf{n}). \end{aligned} \tag{4.22}$$

The expansion of $\tilde{g}(\mathbf{k}, \mathbf{n}, \mathbf{n}')$, however, is not so simple. For a discussion of molecular pair distribution functions see chapter 11 of reference [62]. In the laboratory fixed frame the expansion of the molecular pair distribution function in spherical harmonics is

$$\begin{aligned} g(\mathbf{r}, \mathbf{n}_a, \mathbf{n}_b) = &\sum_{l_a}\sum_{l_b}\sum_{l} g_{l_a l_b l}(r) \sum_{m_a}\sum_{m_b}\sum_{m}\langle l_a\, m_a, l_b\, m_b | l\, m\rangle \\ &\times Y_{l_a}^{m_a}(\mathbf{n}_a)Y_{l_b}^{m_b}(\mathbf{n}_b)Y_l^{m\,*}(\Omega_r), \end{aligned} \tag{4.23}$$

where $\Omega_r \equiv \{\theta_r, \phi_r\}$ are the angles defining the orientation of the vector $\mathbf{r}$ and $\langle l_a\, m_a, l_b\, m_b | l\, m\rangle$ is a Clebsch-Gordan coefficient. The real space components can be calculated in the laboratory frame as

$$\begin{aligned} g_{l_a l_b l}(r) = &\frac{1}{2l+1}\int_O d\mathbf{n}_a \int_O d\mathbf{n}_b\, d\Omega_r \sum_{m_a}\sum_{m_b}\sum_{m}\langle l\, m | l_a\, m_a, l_b\, m_b\rangle \\ &\times Y_{l_a}^{m_a\,*}(\mathbf{n}_a)Y_{l_b}^{m_b\,*}(\mathbf{n}_b)Y_l^m(\Omega_r)g(\mathbf{r}, \mathbf{n}_a, \mathbf{n}_b), \end{aligned} \tag{4.24}$$

where $|l_a - l_b| \leq l \leq l_a + l_b$ and the limits on the sum over m_i are $-l_i$ to l_i. In this same frame the Fourier transform takes a particularly simple form

$$\begin{aligned}\tilde{g}(\mathbf{k}, \mathbf{n}_a, \mathbf{n}_b) = &\sum_{l_a}\sum_{l_b}\sum_{l}\tilde{g}_{l_a l_b l}(k)\sum_{m_a}\sum_{m_b}\sum_{m}\langle l_a\, m_a, l_b\, m_b | l\, m\rangle \\ &\times Y_{l_a}^{m_a}(\mathbf{n}_a) Y_{l_b}^{m_b}(\mathbf{n}_b) Y_l^{m\,*}(\Omega_k),\end{aligned} \tag{4.25}$$

in which $\Omega_k \equiv \{\theta_k, \phi_k\}$ are the angles defining the orientation of the vector $\mathbf{k}$. The real space and Fourier space components are related through the generalized Hankel transform [62],

$$\tilde{g}_{l_a l_b l}(k) = 4\pi i^l \int_0^\infty dr\ j_l(kr)(g_{l_a l_b l}(r) - g_{l_a l_b l}(\infty))r^2, \tag{4.26}$$

where $g_{l_a l_b l}(\infty)$ (which is constant for $l = l_a = l_b = 0$, and 0 when at least one of l_a, l_b, or l is non-zero) has been subtracted (affecting only $k = 0$) so that the Hankel transform converges. By inserting eq. (4.25) into eq. (4.22) and utilizing the orthogonality of the spherical harmonics and projecting onto a particular spherical harmonic the following equation is obtained:

$$\begin{aligned}0 = &- E\left[\left(\frac{\rho_0}{4\pi}\right)^2 \sum_{l_2}\sum_{l}\tilde{g}_{l_1 l_2 l}(k)\sum_{m_2}\sum_{m}(-1)^{m_2}\langle l_1\, m_1, l_2\, m_2 | l\, m\rangle Y_l^{m\,*}(\Omega_k)\tilde{f}_{l_2}^{-m_2}(\mathbf{k}) + \frac{\rho_0}{4\pi}\tilde{f}_{l_1}^{m_1}(\mathbf{k})\right] \\ &+ \frac{\rho_0}{4\pi}\frac{\hbar^2 k^2}{2m}\tilde{f}_{l_1}^{m_1}(\mathbf{k}) + \frac{\rho_0}{4\pi}\frac{\hbar^2}{2I}l_1(l_1+1)\tilde{f}_{l_1}^{m_1}(\mathbf{k}),\end{aligned} \tag{4.27}$$

which can be written in the more suggestive form

$$\mathbf{T}(\mathbf{k})\tilde{\mathbf{f}}_i(\mathbf{k}) = E_i(\mathbf{k})\mathbf{G}(\mathbf{k})\tilde{\mathbf{f}}_i(\mathbf{k}), \tag{4.28}$$

where $\mathbf{T}(\mathbf{k})$ and $\mathbf{G}(\mathbf{k})$ are matrices and $\tilde{\mathbf{f}}_i(\mathbf{k})$ is a generalized eigenvector with eigenvalue $E_i(\mathbf{k})$.

In a homogeneous system the energy should not depend on the direction of $\mathbf{k}$ so it is possible to choose any direction, with $\mathbf{k}$ along the z-axis being a convenient choice. Then

$$Y_l^m(\theta_k = 0, \phi_k) = \sqrt{\frac{2l+1}{4\pi}}\delta_{m,0}, \tag{4.29}$$

which simplifies eq. (4.27) to

$$\begin{aligned}0 = &- E\left[\left(\frac{\rho_0}{4\pi}\right)^2 \sum_{l_2}\sum_{l}\tilde{g}_{l_1 l_2 l}(k)\langle l_1\, m, l_2\, -m | l\, 0\rangle(-1)^m\left(\frac{2l+1}{4\pi}\right)^{1/2}\tilde{f}_{l_2}^{m}(\mathbf{k}) + \frac{\rho_0}{4\pi}\tilde{f}_{l_1}^{m}(\mathbf{k})\right] \\ &+ \frac{\rho_0}{4\pi}\frac{\hbar^2 k^2}{2m}\tilde{f}_{l_1}^{m}(\mathbf{k}) + \frac{\rho_0}{4\pi}\frac{\hbar^2}{2I}l_1(l_1+1)\tilde{f}_{l_1}^{m}(\mathbf{k}).\end{aligned} \tag{4.30}$$

Here the property of Clebsch-Gordan coefficients that they vanish unless $m_1 + m_2 = m$ has been used to eliminate the sum over m_2. From this it is clear that the matrix elements which must be calculated are

$$\begin{aligned}\langle l_2 m_2|\mathbf{G}(\mathbf{k})|l_1 m_1\rangle =& \delta_{m_1,m_2}\left(\frac{\rho_0}{4\pi}\right)^2 \sum_l \tilde{g}_{l_1 l_2 l}(k)\langle l_1\, m_1, l_2\, -m_2|l\, 0\rangle(-1)^{m_2}\left(\frac{2l+1}{4\pi}\right)^{1/2} \\ &+ \delta_{l_1,l_2}\delta_{m_1,m_2}\frac{\rho_0}{4\pi}\end{aligned} \tag{4.31}$$

and

$$\langle l_2 m_2|\mathbf{T}(\mathbf{k})|l_1 m_1\rangle = \delta_{l_1,l_2}\delta_{m_1,m_2}\left[\frac{\rho_0}{4\pi}\frac{\hbar^2 k^2}{2m} + \frac{\rho_0}{4\pi}\frac{\hbar^2}{2I}l_2(l_2+1)\right], \tag{4.32}$$

where the sum over l is restricted to l such that $|l_1 - l_2| \leq l \leq l_1 + l_2$. Here it is through $\tilde{g}_{l_1 l_2 l}(k)$ that the dependence of the eigenenergies, $E_i(\mathbf{k})$, on the potential energy, $V(\mathbf{X})$, enters.

As an illustrative example consider the result of a PIGS simulation of 32 translating non-interacting rigid rotors in a $3\times3\times3$ a.u. periodic box with $hB = 1$ a.u. and $\hbar^2/(2m) = 1/4$ a.u., sampling both translational and rotational degrees of freedom. In this case the Hamiltonian of the system is

$$H = \sum_{i=1}^{N}\frac{\mathbf{p}_i^2}{2m} + \sum_{i=1}^{N}\frac{\mathbf{L}_i^2}{2I}, \tag{4.33}$$

with exact wave functions

$$\Phi(\mathbf{X}) = \prod_{i=1}^{N}\frac{1}{\sqrt{V}}e^{-i\mathbf{k}_i\cdot\mathbf{r}_i}Y_{l_i}^{m_i}(\mathbf{n}_i), \tag{4.34}$$

where the possible values of $\mathbf{k}_i$ are restricted by the box side lengths. The elementary excitation spectrum can be found simply by increasing $\mathbf{k}_i$ or promoting the rotational state of a single particle, meaning that the spectrum in the large box limit is comprised of a series of parabolas of the form

$$E_{l,m}(\mathbf{k}) = \frac{\hbar^2 k^2}{2m} + hBl(l+1) \tag{4.35}$$

split by the free-rotor energy splitting. The results of such a PIGS Monte Carlo simulation with imaginary time path length $\beta = 10\,\hbar/E_h$, imaginary time step $\tau = 10/8\,\hbar/E_h$, and using a constant trial wave function, are shown in figure 4 and clearly show excellent agreement with the predicted spectrum from eq. (4.35).

For this simple toy system of a homogeneous gas of non-interacting rigid rotors the application of eq. (4.28) is trivial. Using eq. (4.24) it is easy to see that for all l_a, l_b, and l greater than zero $g_{l_a l_b l}(r) = 0$ for a homogeneous system of rigid rotors in their respective ground states. Furthermore, without pair-wise interactions between rigid rotors there will be no structure in the single non-vanishing pair distribution function, $g_{000}(r)$, *i.e.* it will be

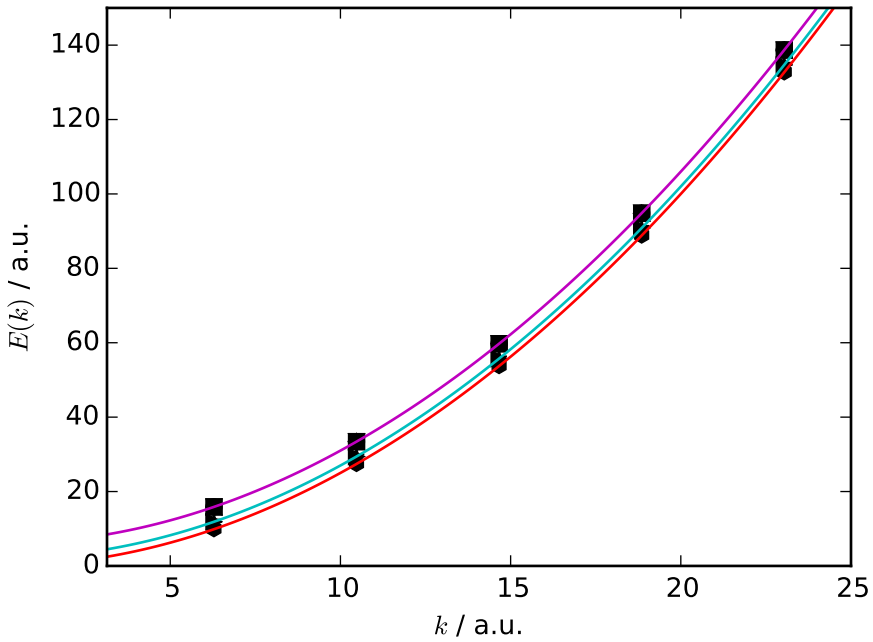

Figure 4.1: The results of a simulation of 32 translating rigid rotors in a periodic box with side length $L = 3$ a.u. showing the excitation spectrum up to $l_{\max} = 2$. The symbols are the results of the simulation and the lines are of the form in eq. (4.35), with $\hbar^2/(2m) = 1/4$ a.u. and $hB = 1$ a.u. The $2l + 1$ curves with the same m for a given l are all degenerate.

constant, since the probability of finding two molecules separated by a distance r should be uniform for all distances in a homogeneous non-interacting system. However, the analysis is no longer trivial when an potential, $V(\mathbf{X})$, is included. As mentioned previously, while this analysis does not depend explicitly on the potential energy, $V(\mathbf{X})$, it does indirectly depend on the interaction potential between pairs of molecules through the effect of interactions on the ground state pair distribution function.

As a concrete example of the effects of interactions on the predicted spectrum, consider the much simpler system of liquid helium. In this case the Feynman-Bijl approximation predicts the appearance of a roton minimum, which arises due to the appearance of a peak in the static structure function, $S(\mathbf{k})$, defined as the Fourier transform of the pair distribution function [34]. For interacting molecular systems this same principle will hold, where interactions will add structure to the molecular pair distribution function resulting in analogous features in the excitation spectrum, with orientation-dependent interaction potentials possibly leading to non-trivial excited state dispersion relations, *e.g.* roton-like features when the potential contains a repulsive interaction at short distances.

Chapter 5

1D Lattices

Polar molecules trapped in one-dimensional optical lattices present an interesting opportunity to study a system which demonstrates an order-disorder quantum phase transition. Under consideration here is a system of polar molecules trapped in a deep optical lattice, such that the center-of-mass motion of individual dipoles is negligible, as are the tunneling rates of molecules between optical lattice sites. Under these conditions the positions of the centers-of-mass of each molecule can then be considered fixed at regular lattice points and only the orientation of the molecules must be considered. Under these approximations, a "crystal" at unit filling (one dipole per lattice site) of molecular dipoles, taken to be heteronuclear diatomic molecules within the rigid rotor approximation, and with an optional electric field can be described with the model Hamiltonian

$$H = \sum_{i=1}^{N} \frac{\mathbf{L}_i^2}{2I} - d\mathbf{n}_i \cdot \mathbf{E} + \sum_{j<i} \frac{C_{\rm dd}}{4\pi|\mathbf{r}_{ij}|^3}(\mathbf{n}_i \cdot \mathbf{n}_j - 3(\mathbf{n}_i \cdot \hat{\mathbf{r}}_{ij})(\mathbf{n}_j \cdot \hat{\mathbf{r}}_{ij})) \tag{5.1}$$

$$= \sum_{i=1}^{N} \frac{\mathbf{L}_i^2}{2I} - d\mathbf{n}_i \cdot \mathbf{E} + \frac{C_{\rm dd}}{4\pi r_{\rm lat}^3} \sum_{j<i} \frac{1}{|i-j|^3}(\mathbf{n}_i \cdot \mathbf{n}_j - 3n_i^x n_j^x), \tag{5.2}$$

where $\mathbf{E} = E\hat{\mathbf{e}}$ is the applied static electric field along the direction $\hat{\mathbf{e}}$, $r_{\rm lat}$ is the distance between nearest neighbors on the 1-dimension lattice, and $\hat{\mathbf{r}}_{ij}$ is a unit vector in the direction of the intermolecular vector between molecules i and j, $\mathbf{r}_{ij} = \mathbf{r}_i - \mathbf{r}_j = (i-j)r_{\rm lat}$. $C_{\rm dd}$ is the dipole-dipole coupling strength which depends on the type of coupling and is given by $C_{\rm dd} = d^2/\epsilon_0$ in the case of electric dipole-dipole coupling, where d is the magnitude of the permanent electric dipole moment in the molecular body-fixed frame. $\mathbf{L}_i^2/(2I)$ is the rotational kinetic energy operator for the ith molecule with moment of inertia I, and $\mathbf{n}_i$ is the orientation of that same molecule. The form of eq. (5.2) assumes that the lattice is along the x-axis so that the location of the jth molecule is $jr_{\rm lat}\hat{\mathbf{x}}$. The Hamiltonian in eq. (5.2) may be written more conveniently in units of $hB = \hbar^2/(2I)$, in which case it becomes

$$H = \sum_{i=1}^{N} \frac{\mathbf{L}_i^2}{\hbar^2} - u\mathbf{n}_i \cdot \hat{\mathbf{e}} + g \sum_{j<i} \frac{1}{|i-j|^3}(\mathbf{n}_i \cdot \mathbf{n}_j - 3n_i^x n_j^x), \tag{5.3}$$

in which the scaled electric field parameter, $u = dE/(hB)$, and interaction parameter, $g = C_{\rm dd}/(4\pi hBr_{\rm lat}^3)$, have been introduced.

In this chapter the behavior of the Hamiltonian in eq. (5.3) will be studied. In section 5.1 several important limiting cases of eq. (5.3) will be presented. Then in section 5.2, a study of the ground states of eq. (5.3) as a function of the interaction strength, g, in the limit of a vanishing electric field, $u = 0$, is presented [63]. In this limit eq. (5.3) can be compared to the well-known quantum rotor model (QRM) [64] which is known not to possess an order-disorder phase transition at $T = 0$ as a result of the Mermin-Wagner theorem [65]. Here it is found that the anisotropy of the dipole-dipole potential changes the nature of the phase diagram from that of the QRM, and strong evidence of an order-disorder phase transition in the orientational degrees of freedom of lattice confined polar molecules is presented in this section.

5.1 Important limiting cases

Non-interacting rigid rotors

The Hamiltonian eq. (5.1) has several interesting limits. First, by inspection, if $g \ll 1$ and $u \ll 1$, then one approximately recovers the Hamiltonian for a collection of non-interacting rigid rotors. In this case one expects the average polarization per particle,

$$\mathbf{n}_{\rm avg} = \frac{1}{N}\left\langle \sum_{i=1}^{N} \mathbf{n}_i \right\rangle, \tag{5.4}$$

to vanish in the ground-state since the ground state wave function in this limit will be

$$\Phi_0(\mathbf{N}) \approx \prod_{i=1}^{N} Y_0^0(\mathbf{n}_i) = \left(\frac{1}{\sqrt{4\pi}}\right)^N, \tag{5.5}$$

which is completely isotropic.

A second limit occurs when $u \gg 0$ and $g \ll 1$. Here the system is well described as an array of non-interacting rotors in a static electric field. In this case each individual rotor will be polarized by its interaction with the electric field of the form $-u\mathbf{n}\cdot\hat{\mathbf{e}} = -u\cos\theta$, where $\hat{\mathbf{e}}$ is assumed to be along $\hat{\mathbf{z}}$, perpendicular to the lattice axis. The wave function is still well approximated by a product of single-particle wave functions,

$$\Phi_0(\mathbf{N}) \approx \prod_{i=1}^{N} \phi_0(\mathbf{n}_i), \tag{5.6}$$

but it is no longer possible to find an analytical solution to the problem. Since the single particle wave function in this limit, $\phi_0(\mathbf{n}_i)$, will be polarized toward the positive z-axis, the average polarization of the system will not vanish and will be proportional to $\hat{\mathbf{z}}$.

The problem of a single dipolar rotor in a uniform electric field can, however, easily be solved numerically using the variational theorem. Eigenstates of the single-particle Hamiltonian

$$H = \frac{\mathbf{L}^2}{\hbar^2} - u\mathbf{n}\cdot\hat{\mathbf{e}} = \frac{\mathbf{L}^2}{\hbar^2} - uC_0^1(\theta,\phi), \tag{5.7}$$

where the electric field is, again, taken to be along the z-axis, perpendicular to the lattice axis, and $C_q^k(\theta,\phi) = \sqrt{4\pi/(2l+1)}Y_k^q(\theta,\phi)$ are the Racah normalized spherical harmonics [36], can conveniently be written in the basis of spherical harmonics, $Y_l^m(\theta,\phi)$. Additional simplification comes from the cylindrical symmetry of eq. (5.7), which suggests that the eigenstates should depend only on the polar angle, θ, and not on the azimuthal angle, ϕ, so that the wave function can be written in the form

$$\phi_0(\mathbf{n}) = \sum_{l=0}^{\infty} c_l Y_l^0(\mathbf{n}) = \sum_{l=0}^{\infty} c_l \sqrt{\frac{2l+1}{4\pi}} P_l(\cos\theta). \tag{5.8}$$

By truncating the expansion at some $l_{\max}$ it is possible to numerically solve an eigenvalue problem in this basis, solving

$$\det(\mathbf{H} - \lambda\mathbb{I}) = 0 \tag{5.9}$$

and

$$(\mathbf{H} - \lambda_i\mathbb{I})\mathbf{c}_i = 0 \tag{5.10}$$

for the eigenvalues and eigenvectors, respectively, to find the lowest energy single-particle eigenfunction in this truncated basis,

$$\phi_0(\mathbf{n}) = \sum_{l=0}^{l_{\max}} \mathbf{c}_{0l} \sqrt{\frac{2l+1}{4\pi}} P_l(\cos\theta), \tag{5.11}$$

where the matrix elements, calculated with the help of the Wigner-Eckart theorem, are

$$\mathbf{H}_{ll'} = \langle l0|H|l'0\rangle = l(l+1)\delta_{ll'} - u\sqrt{(2l+1)(2l'+1)} \begin{pmatrix} l & 1 & l' \\ 0 & 0 & 0 \end{pmatrix}^2. \tag{5.12}$$

This procedure can be done repeatedly with larger and larger values of $l_{\max}$ until the energies and eigenfunctions of eq. (5.7) have been found to the desired accuracy. Alternatively, for weak to moderate electric fields the single-particle function can be approximated as

$$\phi_{\text{trial}}(\mathbf{n}) = e^{\alpha\cos\theta}, \tag{5.13}$$

with a single variational parameter α. Trial wave functions of this form can be optimized by finding the value of the parameter, $\alpha_{\min}$, which minimizes the variational estimate of the energy,

$$E_{\text{var}}(\alpha) = -\frac{1}{N(\alpha)} \int_0^{\pi} d\theta\, \sin\theta \left(e^{\alpha\cos\theta} \frac{1}{\sin\theta} \frac{\partial}{\partial\theta} \sin\theta \frac{\partial}{\partial\theta} e^{\alpha\cos\theta} + e^{2\alpha\cos\theta} u\cos\theta \right), \tag{5.14}$$

with normalization

$$N(\alpha) = \int_0^\pi d\theta \, \sin\theta \, e^{2\alpha \cos\theta}. \tag{5.15}$$

In figure 5.1 the optimized variational solution, eq. (5.13) is compared to a numerically exact solution of eq. (5.11), converged with respect to $l_{\max}$, for a field strength of $u = 0.5$, demonstrating excellent agreement.

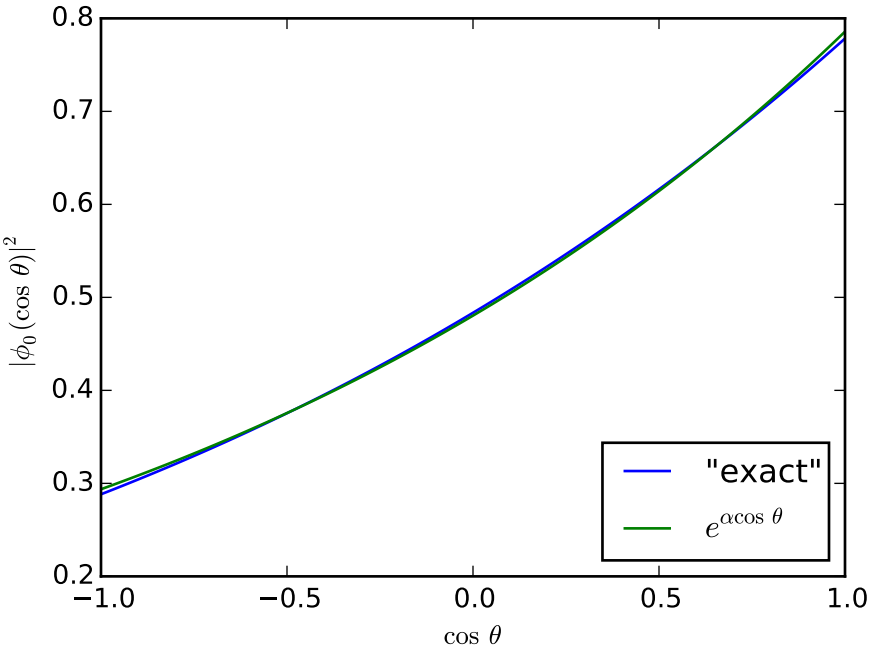

Figure 5.1: Comparison of the approximate wave functions of the form of eq. (5.11), with $l_{\max} = 50$ ("exact"), and the variational solution of eq. (5.13) for $u = 0.5$. Good agreement can be found for a broad range of external field strengths.

The form of the single particle wave function in eq. (5.13) is very convenient for quantum Monte Carlo simulations at a practical level because it requires relatively few elementary operations to evaluate as compared to a sum of orthogonal polynomials as most programming languages offer a fast built-in exponential function. The single particle trial wave function in eq. (5.13) is unnormalized, but this poses no practical problem for PIGS simulations as the calculation of acceptance probabilities for trial moves require ratios of the trial wave function.

Strongly interacting dipolar rotors

The third important limit of eq. (5.1) is when $g \gg 1$ and $u \ll 1$. In this case the behavior is dominated by the dipole-dipole potential energy, plotted in figures 1 and 1. As discussed

in chapter 1 due to the dipole-dipole interaction potential the system will tend to order itself in a "tip-to-tail" configuration polarized along the lattice axis, which is the potential energy minimum of the dipole-dipole potential for dipoles confined to discrete points along one dimension. In the case of eq. (5.2) this is the x-axis. This limit exhibits spontaneous symmetry breaking, because there is an additional inversion symmetry, demonstrated in figure 1 (b) [63]. Because of this, care must be taken during PIGS simulations when calculating the average polarization, since for finite-sized systems the simulation averaged polarization may vanish due to switching from one symmetry-related sector to the other over the course of a single simulation. This switching is suppressed for larger systems because the barrier to switching grows with system size. The effect can be mitigated by tracking an unsigned polarization,

$$n_{\text{abs}} = \frac{1}{N} \left\langle \left| \sum_{i=1}^{N} \mathbf{n}_i \right| \right\rangle , \tag{5.16}$$

instead of $\mathbf{n}_{\text{avg}}$. Unlike $\mathbf{n}_{\text{avg}}$, n_{abs} has the same value for both symmetry-related configurations depicted in figure 5.1.

There are many possible choices of trial wave function in this situation. Among these is a product wave function with single-particle wave functions similar to eq. (5.13) but rotated to reflect the symmetry about the lattice (x-) axis, *i.e.* replacing $\cos\theta = n^z$ with $\cos\phi\sin\theta = n^x$, then optimizing the variational parameter, α, for the mean-field, *e.g.* determined by a self-consistent field (SCF) approach (see, for example, the discussion on the application of a mean-field method to this problem in section 5.2 below). This procedure works well for $g \gg 1$ and $g \ll 1$ but such product wave functions break down at intermediate dipole-dipole interaction strengths due to increasing correlation lengths, as shall be shown in section 5.2 below.

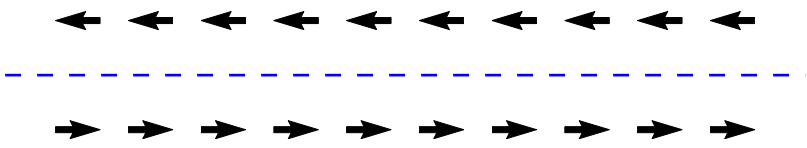

Figure 5.2: The symmetry related configurations in the limit $g \gg 1$ and $u \ll 1$. Inversion through the origin relates the two degenerate symmetry-related configurations: all of the dipoles pointing along the negative x-axis and all of the dipoles pointing along the positive x-axis.

5.2 Orientational phase transitions in the absence of applied fields

Now consider ground states of eq. (5.3) when there is no externally applied field to orient the molecular dipoles, $u = 0$, but with variable interaction strength, g, *i.e.* between the first and third limits of section 5.1. Hamiltonian (5.3) simplifies to

$$H = \sum_{i=1}^{N} \frac{\mathbf{L}_i^2}{\hbar^2} + g \sum_{j<i} \frac{1}{|i-j|^3} (\mathbf{n}_i \cdot \mathbf{n}_j - 3 n_i^x n_j^x), \tag{5.17}$$

which can be directly compared to the well known O(3) quantum rotor model (QRM),

$$H_{\mathrm{QRM}} = \sum_{i=1}^{N} \frac{\mathbf{L}_i^2}{2\tilde{g}} + \sum_{j<i} J_{ij} \mathbf{n}_i \cdot \mathbf{n}_j, \tag{5.18}$$

with some general dependence on the distance between rotors encoded in J_{ij}. The O(3) QRMs in $d = 1$ with both nearest neighbor couplings [64] and dipolar ($1/r^3$) couplings [65] exhibit no order-disorder phase transition for any value of $\tilde{g} > 0$. This can be seen by mapping them onto the equivalent $d+1$ dimensional classical models at a finite temperature via Trotterization, effectively introducing a nearest-neighbor interaction along an extra spatial dimension [66]. From this it is evident that there cannot be spontaneous symmetry breaking of the continuous O(3) symmetry at finite $\tilde{g} > 0$ [64, 65], a consequence of the Mermin-Wagner theorem, which forbids spontaneous symmetry breaking at finite temperatures in low dimensional systems with short ranged interactions and continuous symmetries [67]. The principle difference between the QRM and Hamiltonian (5.17) is the addition of the term $-3 n_i^x n_j^x$, which breaks the continuous O(3) symmetry but leaves a residual discrete, inversion symmetry, thus allowing the possibility of an order-disorder phase transition at some $g_c > 0$.

As a preliminary study, the phase diagram of eq. (5.17) was computed using a mean-field theory. In this case the real Hamiltonian was replaced with an effective single-site Hamiltonian

$$H_{\mathrm{mf}} = \frac{\mathbf{L}^2}{\hbar^2} + g \sum_{k=1}^{\infty} \frac{2}{k^3} \left(\mathbf{n} \cdot \langle \mathbf{n} \rangle - 3 n^x \langle n^x \rangle \right) = \frac{\mathbf{L}^2}{\hbar^2} - g \mathbf{n} \cdot \boldsymbol{\epsilon}_{\mathrm{mf}}, \tag{5.19}$$

where $-g \mathbf{n} \cdot \boldsymbol{\epsilon}_{\mathrm{mf}}$ is the interaction of the single dipole with the mean effective electric field, determined self-consistently, with direction components

$$\epsilon_{\mathrm{mf}}^x = 4\zeta(3) \langle n^x \rangle , \tag{5.20}$$

$$\epsilon_{\mathrm{mf}}^y = -2\zeta(3) \langle n^y \rangle , \tag{5.21}$$

$$\epsilon_{\mathrm{mf}}^z = -2\zeta(3) \langle n^z \rangle , \tag{5.22}$$

where the Riemann zeta function,

$$\zeta(3) = \sum_{k=1}^{\infty} \frac{1}{k^3}, \tag{5.23}$$

accounts for the sum over lattice sites. This is done in the usual way, by starting with an initial guess and iteratively solving the eigenvalue equation for the eigenvalues and eigenvectors of eq. (5.19), using the ground state solutions to determine $\langle n^i \rangle$ $(i = x, y, z)$ used to determine $\boldsymbol{\epsilon}_{\text{mf}}$ for the next iteration, until convergence is achieved. Taking into account the symmetry about the lattice axis $\langle n^y \rangle = \langle n^z \rangle = 0$ the problem can be solved in the basis of spherical harmonics with an initial trial wave function of the form

$$\phi_{\text{trial}}(\mathbf{n}) = \frac{1}{\sqrt{2}} \left(Y_0^0(\mathbf{n}) - \frac{1}{\sqrt{2}} \left(Y_1^1(\mathbf{n}) - Y_1^{-1}(\mathbf{n}) \right) \right), \tag{5.24}$$

which is polarized along the x-axis. By studying the mean-field per-particle polarization, $\phi_{\text{mf}} = \langle n^x \rangle$, one can see that SCF calculations predict an orientational phase transition at $g_c \approx 0.6$, reflected by the rapid increase of the mean-field order parameter, ϕ_{mf}, from 0 as shown in figure 5.2.

As a brief aside, with SCF calculations it is fine to use a signed order parameter like ϕ_{mf}, since such calculations are by their nature deterministic. This means that during the course of a calculation, barring some numerical instability, the direction of $\boldsymbol{\epsilon}_{\text{mf}}$ and, as a consequence of this, also the sign of ϕ_{mf} will not change.

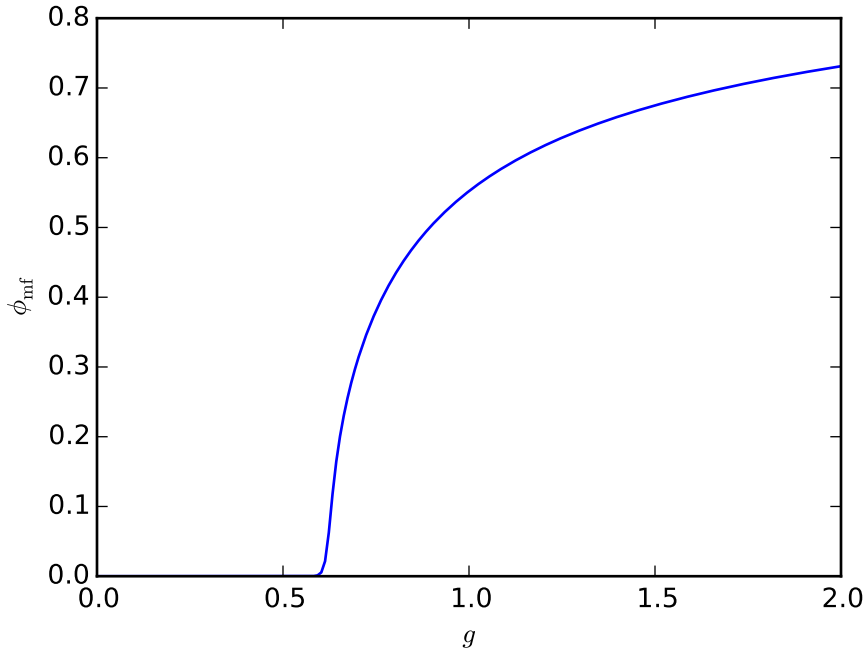

Figure 5.3: The phase diagram of a one-dimensional lattice of dipolar rotors as determined through self-consistent field theory. The SCF treatment predicts a phase transition near $g_c \approx 0.6$.

The SCF treatment of the problem necessarily neglects correlations between particles which are properly captured by quantum Monte Carlo simulations. However, while the SCF calculations were for an infinite sized system, the nature of PIGS simulations restricts them to finite sized systems (specifically systems with a finite number of degrees of freedom). In order to simulate extended systems it is necessary to introduce some approximation. Perhaps the most common approximation is the introduction of periodic boundary conditions [53]. Under this approximation the system is considered to be composed of a finite number of molecules in the primary simulation box. This simulation box is then tiled in all directions, so that the primary simulation box appears to be embedded in an extended system, depicted in figure 5.2. Naturally, a molecule will be perfectly correlated with periodic images of itself, introducing artifacts due to the finite sized nature of the simulation if the extents of the primary simulation box are too small. In the following, periodic boundary conditions are utilized with the nearest image (or minimum image) convention [53]. In order to gauge the effect of approximating an infinite sized system by a finite sized system, multiple system sizes were simulated.

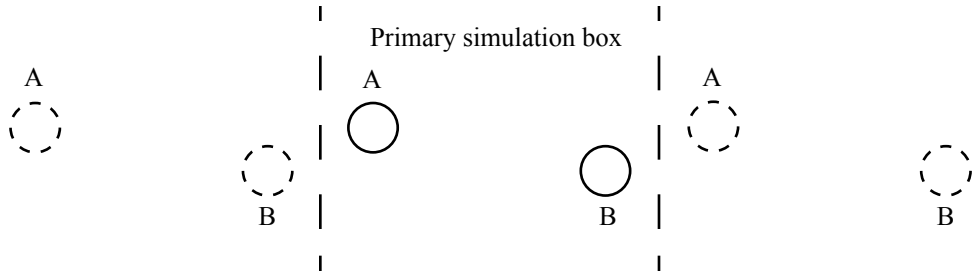

Figure 5.4: Cartoon of a primary simulation box in a quasi-1D system in which periodic tilings are considered in one direction but not the others. In the center is the primary simulation box containing the physical degrees of freedom, in this case two particles. Pictured on either side are two of the infinite number of periodic images of the primary simulation box. Under the nearest image convention particle A will only interact with the nearest periodic "image" of particle B, in this case one of the periodic images.

As noted before, it is possible, over the course of a single simulation, for the state of a finite sized system to switch between the two symmetry related sectors depicted in figure 5.1 since this requires only the coordinated motion of a finite number of dipoles. Because of this it is necessary to use an unsigned order parameter, in this case $\phi_{\text{abs}} = n_{\text{abs}}$. The downside of this choice of order parameter is that even for non-interacting systems, this order parameter as calculated during a Monte Carlo simulation will not completely vanish; the average signed polarization does vanish but any single path configuration is likely to exhibit some small but non-zero net polarization, and the average magnitude of these many small but non-zero polarizations means that the unsigned polarization will take on a small but non-zero value.

Before proceeding to a study of the phase diagram of Hamiltonian (5.17) a series of simulations using a constant trial wave function, eq. (5.5), were performed to quickly determine

an appropriate small time step size, τ, and imaginary path length, β, as described in chapter 3. It was initially decided that the range of values of g studied would go from $g = 0$, being the completely non-interacting case, to $g = 2$, which, it would be discovered through further investigation, encompasses all of the interesting phase behavior of this Hamiltonian. Then simulations were performed at $g = 2$ with a small system size while varying τ and keeping β fixed to determine an appropriate small time step size, τ, shown in figure 5.2. Once this value of τ was determined, a similar series of simulations was undertaken, this time with τ fixed to the previously determined value and varying β, for a representative set of the values of g under consideration. This allowed the determination of an appropriate value for β. The results of this second convergence test are shown in figure 5.2. Based on these results, shown in figures 5.2 and 5.2, a PIGS study of the phase diagram of Hamiltonian (5.17) was undertaken with 153 time slices and with a total imaginary-path length $\beta = 20.0\ (2\pi B)^{-1}$, so that the time-step is $\tau \approx 0.132\ (2\pi B)^{-1}$ and using the same constant trial wave function, eq. (5.5), also employed for figures 5.2 and 5.2.

Figure 5.2 depicts the behavior of ϕ_{abs} vs. g for a variety of system sizes. From this plot it appears that around a critical value of $g_c \approx 0.9$ there is a transition from a disordered phase below g_c to an ordered phase above g_c, signaled by a sharp rise in ϕ_{abs} around this value of g. This transition is more pronounced with larger system sizes, consistent with the existence of finite-sized effects.

The exact nature of this transition cannot be determined from figure 5.2, but inspection of the histograms of per-particle signed polarization along the x-axis,

$$\phi_x = \left\langle \frac{1}{N} \sum_{i=1}^{N} n_i^x \right\rangle, \tag{5.25}$$

as a function of g, shown in figure 5.2, shows that there appears to be no coexistence between ordered and disordered phases, suggesting that this phase transition is of order two or higher [68].

Further evidence for the existence of an orientational phase transition can be found by studying the behavior of the correlation function

$$C(j) = \frac{1}{N} \sum_{i=1}^{N} \left(\left\langle n_i^x n_{i+j}^x \right\rangle - \left\langle n_i^x \right\rangle \left\langle n_{i+j}^x \right\rangle \right). \tag{5.26}$$

From simulations with 64 molecular dipoles this correlation function was found to decay roughly exponentially as $C(j) \propto e^{-j/\eta}$. By extracting this characteristic length scale η and plotting it against the interaction strength, g, a prominent peak was found just above $g_c \approx 0.9$, shown in figure 5.2. This increasing correlation length, likely broadened by finite size effects, could be consistent with the expected divergence of correlation lengths near a critical point [68], providing further evidence for an order-disorder orientational phase transition in this system near $g_c \approx 0.9$ — 1.

To put this phase transition in context, we note that typical heteronuclear diatomic molecules have rotational constants $B \approx 0.5$ — 10 GHz and dipole moments $d \approx 0.5$ —

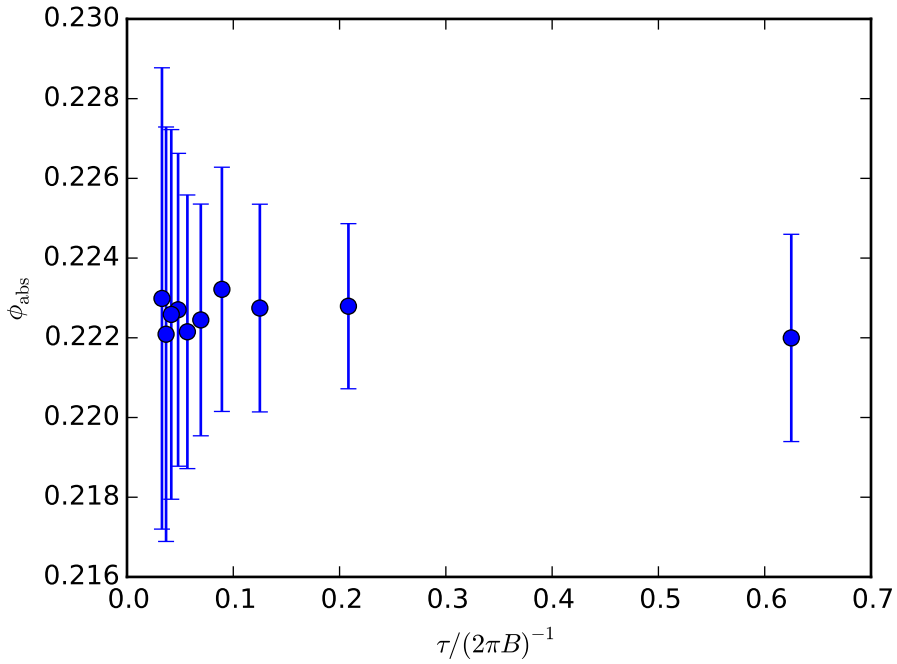

Figure 5.5: Results of a series of PIGS simulations of Hamiltonian (5.17) with four dipoles and an interaction strength $g = 2$ while varying the small time step, τ, but keeping the total path length, β, constant at $\beta = 5.4\ (2\pi B)^{-1}$. Plotted is ϕ_{abs}, defined in eq. (5.16), vs. the small time step, τ, showing that within error bars the quantity is converged with respect to the time step. When determining whether a quantity, in this case ϕ_{abs}, has converged with respect to τ it is only necessary to treat the strongest interaction under consideration in a given set of simulations since the convergence with respect to τ only depends on how much the Hamiltonian deviates from the free-particle Hamiltonian, (see section 3.1).

10 D. With these parameters the phase transition in a one-dimensional molecular crystal is predicted to occur for lattice spacing less than 50 nm. Concretely, for the system ^{133}Cs^{127}I, with $B = 0.71$ GHz [70] and $d = 11.69$ D [71], a lattice spacing of 30 nm will yield a coupling strength of $g = 1.08$. However, typical optical lattice spacings in current experimental realizations are generally an order of magnitude greater than this [3, 25], implying that observing this transition experimentally in optical lattice experiments at unit fillings would be a difficult task with current technology. Still, in systems with multiple occupancy of lattice sites such an effect could have consequences for the stability of such a system, since intermolecular spacings on the order of tens of nanometers which are to be expected within a single lattice site, would certainly put the system in a regime where the dipole-dipole interactions could play an important role. Furthermore, new nanoplasmonic lattice technology, currently available for atomic systems [72], could lead to lattice spacings on this same scale with unit

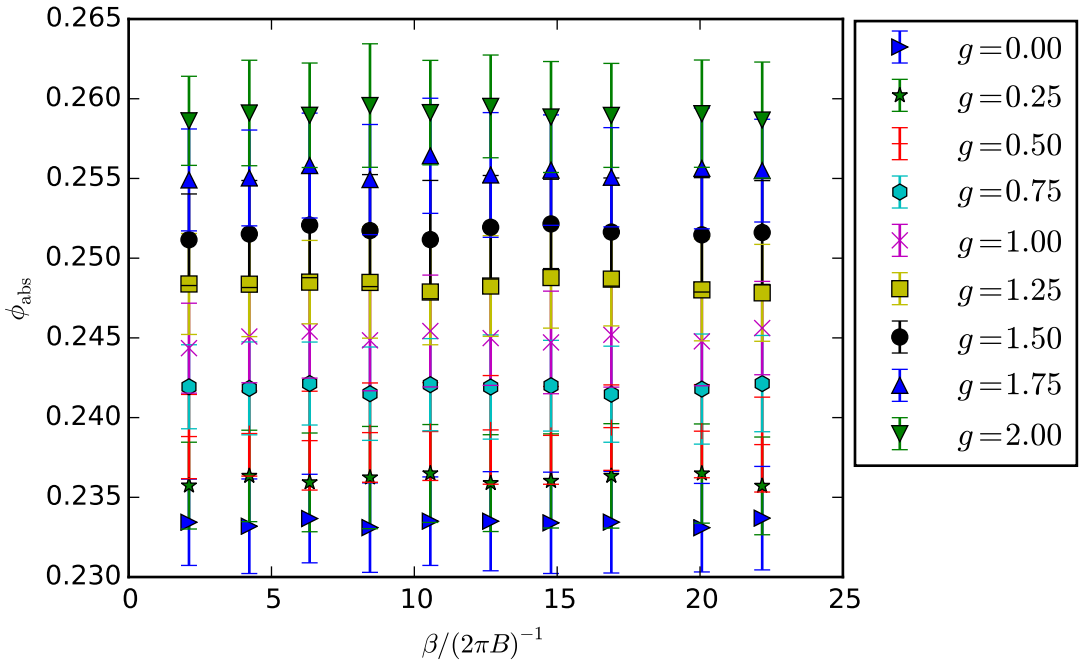

Figure 5.6: Results of a series of PIGS simulations of Hamiltonian (5.17) with four dipoles and interaction strengths ranging from $g = 0$ to $g = 2$ while varying β but keeping τ constant at $\tau = 0.132\ (2\pi B)^{-1}$. Plotted is ϕ_{abs} vs. total path length, β, demonstrating convergence of ϕ_{abs} to within error bars with respect to β for a variety of interaction strengths.

filled lattices, which would also put such systems of lattice confined polar molecules in the $g > 1$ regime.

The PIGS method also allows for the simulation of systems with applied electric fields, *i.e.*, for $u > 0$. In one dimension the expected effect of adding a transverse electric field is the modification of the phase transition by replacing the disordered phase by a phase in which the dipoles are polarized with the applied electric field. As this was deemed to be of lesser interest than the study of two-dimensional systems, chapter 6, the study of such systems was forgone in this dissertation. However, simulations of systems of dipoles in two dimensions commonly utilize transverse electric fields in order to polarize the system and control the interaction potential. PIGS simulations with applied transverse electric fields in two dimensions will be presented in chapter 6.

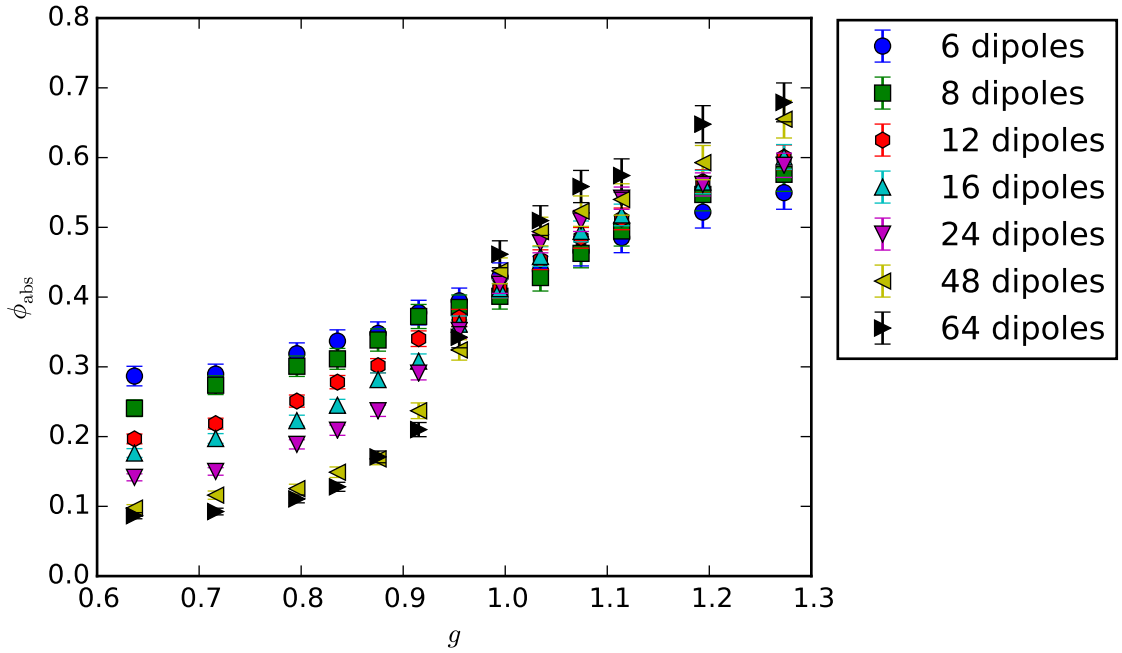

Figure 5.7: The order parameter, ϕ_{abs} vs. interaction strength, g, calculated for a variety of system sizes from 6 to 64 dipoles. From these simulations it appears that there is an orientational phase transition near $g_c \approx 0.9$.

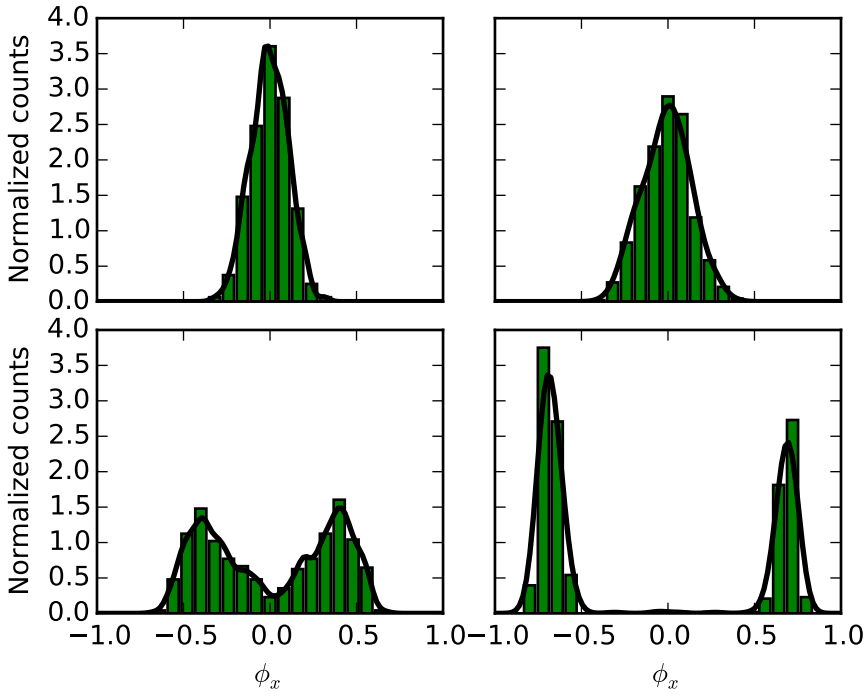

Figure 5.8: Histograms of the order parameter ϕ_x, eq. (5.25), for 64 dipoles in a 1D periodic array with $u = 0$ and $g = 8/(4\pi)$ (top left), $g = 10/(4\pi)$ (top right), $g = 12/(4\pi)$ (bottom left), and $g = 16/(4\pi)$ (bottom right). The curve in each case is an optimized Gaussian kernel density estimate [69]. The lack of a trimodal histogram at $g = 12/(4\pi) \approx 0.95$ suggests that the transition from disordered behavior at low g to ordered behavior at high g is continuous, there being no coexistence between the two phases. Asymmetries in the distributions likely arise from the fact that these represent a finite number of samples.

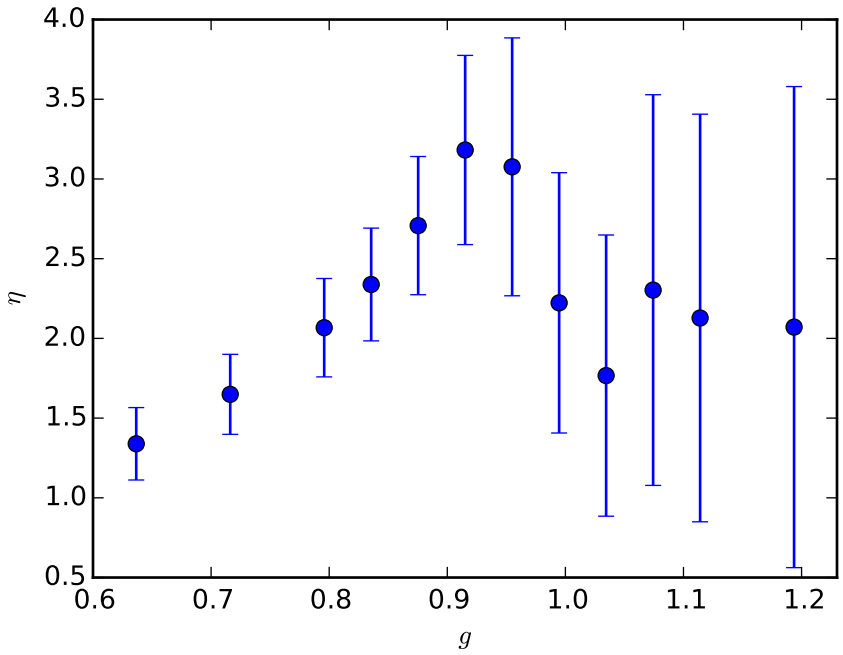

Figure 5.9: The characteristic length, η, of the exponential decay of the correlation function defined in eq. (5.26) in a system of 64 dipoles in a periodic box under the nearest image convention.

Chapter 6

2D lattices

Dipolar molecular ensembles in two spatial dimensions have been the subject of extensive study for their long-ranged, anisotropic, and tunable interactions, both on lattices and in continuum systems [1]. Quasi-2D harmonically confined systems have been of interest both in order to understand the circumstances under which such ensembles are stable to collapse [73], as well as the ability of such ensembles to organize into exotic quantum phases of matter [4, 42, 43, 74–78]. The low energy spectrum of systems comprised of dipoles harmonically confined loosely in two directions and tightly in the third, and polarized by an applied electric field along the tightly confined direction so that the dipole-dipole interaction is purely repulsive, is characterized by a roton minimum [73, 75, 79]. These quasi-2D systems appear to collapse under insufficient trapping in the out-of-plane direction, allowing molecules to explore the purely attractive region of the dipole-dipole interaction potential that leads to this instability [73]. Under sufficiently tight confinement such systems organize themselves into regular triangular lattices [4, 74] and have even been shown to exhibit more exotic phases such as supersolid [76] phases and even a quantum mechanical crystalline phase which is stabilized by zero-point motion of the trapped dipoles [78].

Dipolar quantum particles confined to two-dimensional optical lattices have also been considered, showing a rich phase diagram here as well [12–14, 80]. Such systems are generally described using an effective Hubbard model Hamiltonian [1], sometimes also including long-ranged interactions [12]. On square optical lattices such systems possess a rich phase diagram, including superfluid, supersolid, and Mott insulator phases [12–14, 81]. With triangular optical lattice geometries, ensembles of dipolar particles possess a normal fluid phase in addition to the Mott insulator, superfluid, and supersolid phases [80].

Previous research in this area has focused largely on fully polarized ensembles *i.e.* the direction of polarization and effective electric dipole moment of the particles is taken as a parameter to be varied [4, 12–14, 42, 43, 73–81]. This can be calculated by considering the degree of polarization of a single dipole in a static electric field, *e.g.* using the linear variational method described in section 5.1. Previous studies were performed with no explicit consideration of the rotational degrees of freedom of dipolar molecules. Implicit in this assumption is a separation of energy scales for rotations and translations. For very dilute sys-

tems where, on average, $hB \gg C_{\rm dd}/(4\pi r^3)$, such a separation of energy scales is valid, since while the dipole-dipole interaction couples rotational and translational degrees of freedom, it does so only weakly. However, for more dense systems with shorter average inter-particle distances, translations and rotations become strongly coupled and it is no longer appropriate to treat particles as completely polarized with an effective dipole moment. This chapter describes the study of the behavior of dipolar molecular systems in two dimensions in which the rotational motion of the molecules has been considered explicitly, utilizing the PIGS method described in chapter 3 and applied to one-dimensional arrays of dipolar molecules in chapter 5. For sections 6.1 and 6.2 translational degrees of freedom are not sampled, as was the case in chapter 5. Considerations for simulating systems with translational degrees of freedom are presented in section 6.3.

As with one-dimensional lattices, the particle positions in the current work were considered to be held at fixed lattice sites, as in a deep optical lattice, and are then governed by the Hamiltonian of eq. (5.1), with the lattice defined now to be in the xy-plane. In 2D the dipole-dipole potential is still not long-ranged (in the sense of energy diverging with increasing system size) but for extended systems the energy is still slow to converge [82], a fact that has consequences for the lowest energy ordering on triangular lattices. Unlike the 1D case, in 2D the Mermin-Wagner theorem does not prohibit a order-disorder (quantum) phase transition even for a system with a continuous symmetry, such as the O(3) quantum rotor model [64], discussed in section 5.2.

Taking this quasi-long ranged behavior into account can be accomplished by extending the sum over interaction partners to all periodic images of interaction partners, instead of just the nearest image [53] as was done in section 5.2. The effective Hamiltonian in this case becomes

$$H = \sum_{i=1}^{N} \frac{\mathbf{L}_i^2}{\hbar^2} - u\mathbf{n}_i \cdot \hat{\mathbf{e}} + g \sum_{j<i} \sum_{\mathbf{v}} \left[\frac{\mathbf{n}_i \cdot \mathbf{n}_j}{|\mathbf{r}_{ij} + \mathbf{v}|^3} - 3\frac{(\mathbf{n}_i \cdot (\mathbf{r}_{ij} + \mathbf{v}))(\mathbf{n}_j \cdot (\mathbf{r}_{ij} + \mathbf{v}))}{|\mathbf{r}_{ij} + \mathbf{v}|^5} \right], \qquad (6.1)$$

expressed in distance units of the lattice spacing between nearest neighbors, $r_{\rm lat}$, and where $u = dE/(hB)$ and $g = C_{\rm dd}/(4\pi hBr_{\rm lat}^3)$ as in 1D systems. Here, the sum over $\mathbf{v}$ is the sum over all vectors connecting the center of the main simulation box to the center of each of its periodic images. Explicitly evaluating such a slowly convergent periodic sum would be quite computationally costly during the course of a simulation and so it is necessary to take a smarter approach. A popular choice, especially for continuum simulations, is the Ewald sum approach, which can be modified for the dipole-dipole interaction [82]. In this method the slowly convergent sum is broken up into two portions, one in real space and a second in reciprocal space, both of which are relatively quickly convergent. This has the advantage of being tunable, with a cutoff parameter effectively determining the trade-off between accuracy and speed [53].

Utilizing the fact that the dipoles described by eq. (6.1) are at fixed positions throughout the entire simulation allows for further simplification. In this case the extended periodic sum

can effectively be precomputed by casting the interaction into the form

$$V_{\text{int}} = g \sum_{j<i} \mathbf{n}_i \cdot \mathbf{S}_{ij} \cdot \mathbf{n}_j, \tag{6.2}$$

where the tensor

$$\mathbf{S}_{ij} = \sum_{\mathbf{v}} \left(\frac{1}{|\mathbf{r}_{ij} + \mathbf{v}|^3} \mathbb{I} - 3 \frac{(\mathbf{r}_{ij} + \mathbf{v})^{\otimes 2}}{|\mathbf{r}_{ij} + \mathbf{v}|^5} \right) \tag{6.3}$$

can be computed before a simulation begins. This allows a much larger cutoff to be utilized such that the sum over images converges for a given system size. It should be emphasized that this extended periodic sum is not a replacement for a proper finite-sized scaling analysis. As stated in section 5.2, particles are necessarily perfectly correlated with their own periodic images, which can overemphasize long-ranged ordering. Nevertheless, explicitly treating interaction ranges beyond those contained in the nearest-image approximation becomes important in studying dipolar systems on triangular lattices, as will be discussed further in section 6.2.

6.1 Square lattices

Polar molecules confined to sites on a two-dimensional square lattice can be used as a model for dipolar molecules confined on a deep optical lattice at unit filling, a simple extension of the one-dimensional lattice work described in chapter 5. Just like the one-dimensional lattice systems it is instructive to first examine all of the limiting cases.

The limit of $g \ll 1$ and $u \ll 1$ and the limit of $g \ll 1$ and $u \gg 1$ are essentially the same as described in section 5.1, leading to a completely disordered phase and a phase with only non-vanishing polarization oriented along the same direction as the electric field, $\mathbf{E}$, respectively. The limit of $g \gg 1$ is not necessarily as straight-forward, however. In 1D it is rather obvious, given the nature of the dipole-dipole potential, that the dominant ordering is going to be alignment of all of the dipoles along the lattice axis, since this represents a global minimum of the potential energy, with only a single family of local minima represented by anti-ferromagnetic ordering perpendicular to the lattice axis. In 2D it is no longer possible to make all interactions purely attractive, since there are always next-nearest-neighbor repulsive interactions, although these are naturally weaker than the nearest-neighbor interactions because the dipole-dipole potential decays as $1/r^3$. The best possible arrangement is then likely to be to order things such that the nearest-neighbor interactions are attractive.

Pictured in figure 6.1 are the considered ordering patterns on 2D square lattices, found by considering what kinds of configurations on a square lattice will lead to attractive interactions. This is aided by examining figures 1, 1, and 1 and remembering that the most attractive interactions occur when dipoles are oriented tip-to-tail, figure 1 (b), while the anti-parallel orientations perpendicular to the intermolecular axis are also attractive, figure 1 (a).

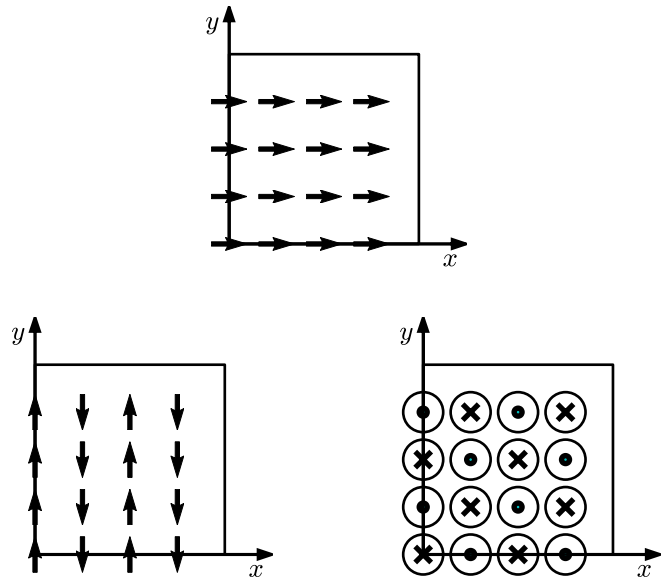

Figure 6.1: The considered orderings in the limit $g \gg 1$ and $u \ll 1$ for a system of 16 dipoles with the primary simulation box outlined for reference. The lattice is in the xy-plane with the z-axis coming out of the plane of the page. On top is one of the infinitely many fully polarized orderings, on the left is one of four degenerate striped orderings, and on the right is one of the two equivalent checkerboard orderings, where a dot ($\cdot$) represents a dipole oriented along the positive z-axis and a $\times$ represents a dipole oriented along the negative z-axis. Their properties are described in the text.

By calculating the classical potential energy of these classes of configurations it is possible to predict the relative stabilities of each: these are shown in figure 6.1 for several system sizes. Of the three, energetically the striped pattern (bottom left panel in figure 6.1) is the most energetically favorable. There are four such striped patterns, all related by a rotation about the z-axis by $n\pi/2$, where $n \in \mathbb{Z}$. In this ordering each of the nearest-neighbor interactions are attractive, although some of the next-nearest-neighbor interactions are repulsive. The next most energetically favorable configurations are the family of fully polarized configurations where all dipoles are polarized in the same direction in the lattice plane (top panel in figure 6.1). This is interesting because, as pictured, only half of the nearest-neighbor interactions are actually attractive, although the repulsive nearest-neighbor interactions are the weaker variety where the orientation of one of the dipoles (depicted as being along the x-axis in figure 6.1) is perpendicular to the inter-dipole axis between it and one of its repulsive

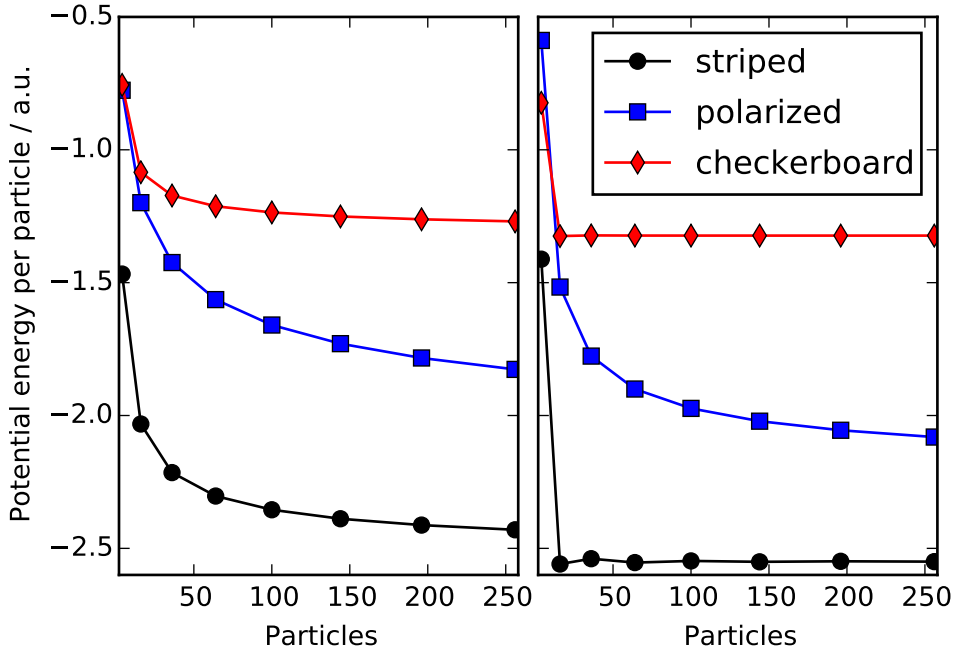

Figure 6.2: The potential energies per particle of the striped, polarized, and checkerboard orders as a function of system size with $C_{\text{dd}}/(4\pi r_{\text{lat}}^3) = 1$ a.u. and $u = 0$ under the extended periodic sum convention with a cutoff radius of 500 lattice sites (left) and the minimum image convention (a cutoff distance of half the side length of the square simulation box, right). Notice that although the cutoff distance for calculating the potential energies are different, the order of potential energies of the three classes of configuration remain the same except for the case of 2×2 lattices. In this case striped configurations have the lowest potential energy, polarized configurations slightly higher potential energy, and checkerboard configurations have the highest potential energy.

neighbors (depicted as being along the y-axis in figure 6.1). All of the infinitely many fully polarized configurations, related by an arbitrary rotation about the z-axis, are degenerate. Finally the least stable, based on potential energy, of the three candidate classes of orderings are the two checkerboard orderings (one is shown in the bottom right panel in figure 6.1), which are related by inversion through the origin.

One more thing is evident by looking at figure 6.1, namely that boundary conditions are very important. In particular, with the given simple periodic boundary conditions it is necessary for the number of lattice sites on any given side of the lattice to be even. This is because with an odd side length it becomes impossible to form a striped ordering or checkerboard ordering where all nearest-neighbor interactions are attractive at the boundaries of the simulation box, effectively introducing a degree of frustration as the dipoles struggle to

find a minimum energy configuration. This boundary induced frustration leads to spurious results; in an infinite system it should be possible to create striped and checkerboard orderings where all nearest-neighbor interactions are purely attractive, leading one to conclude that simulation boxes must contain an even number of rows and columns if one wishes to approximate infinite systems with a finite number of dipoles.

With square lattice systems, for all but the smallest system sizes, the nearest image convention predicts the same relative order of the potential energies of each of the candidate orderings as does the extended periodic sum, depicted in figure 6.1. Because of the simplicity of implementation of the nearest image convention simulations were therefore run using periodic boundary conditions with the nearest image convention rather than using an extended periodic sum.

Finding an order-disorder phase transition requires the definition of an order parameter and just as in the 1D case, it is necessary here to define an order parameter that takes on the same value for each of the (four) striped orderings. The order parameter

$$\phi_{xy} = \left\langle \sqrt{n^2_{x\text{-stripe}} + n^2_{y\text{-stripe}}} \right\rangle, \tag{6.4}$$

where the operators

$$n_{x\text{-stripe}} = \frac{1}{N} \left| \sum_{i=1}^{\sqrt{N}} \sum_{j=1}^{\sqrt{N}} (-1)^i n^x_{i\sqrt{N}+j} \right| \tag{6.5}$$

and

$$n_{y\text{-stripe}} = \frac{1}{N} \left| \sum_{i=1}^{\sqrt{N}} \sum_{j=1}^{\sqrt{N}} (-1)^j n^y_{i\sqrt{N}+j} \right| \tag{6.6}$$

pick out striped configurations with tip-to-tail interactions along the x- and y-axis, respectively, fulfills this requirement. Equations (6.5) and (6.6) assume that the molecule in the lattice site at the position $\mathbf{r}_i = j\hat{\mathbf{x}} + k\hat{\mathbf{y}}$, in units of r_{lat}, is identified by the particle index $i = k\sqrt{N} + j$. In principle, this order parameter vanishes for a phase without striped order and has a maximum value of 1 in the case that the system exhibits striped ordering. In practice, as with the absolute value order parameter defined for 1D lattice systems, eq. (5.16), ϕ_{xy} will never quite vanish for a finite-sized system since each configuration will likely possess a small, non-zero value of this particular order parameter. The two additional order parameters

$$\phi_{\text{checkerboard}} = \left\langle \frac{1}{N} \left| \sum_{i=1}^{\sqrt{N}} \sum_{j=1}^{\sqrt{N}} (-1)^{i+j} n^z_{i\sqrt{N}+j} \right| \right\rangle \tag{6.7}$$

and

$$\phi_{j\text{-polarization}} = \left\langle \frac{1}{N} \left| \sum_{i=1}^{N} n^j_i \right| \right\rangle, \tag{6.8}$$

with $j = x, y, z$, were used to probe for checkerboard ordering and j-axis polarization, respectively. With square lattice systems no evidence of these latter two orderings was found in any of the PIGS simulations performed.

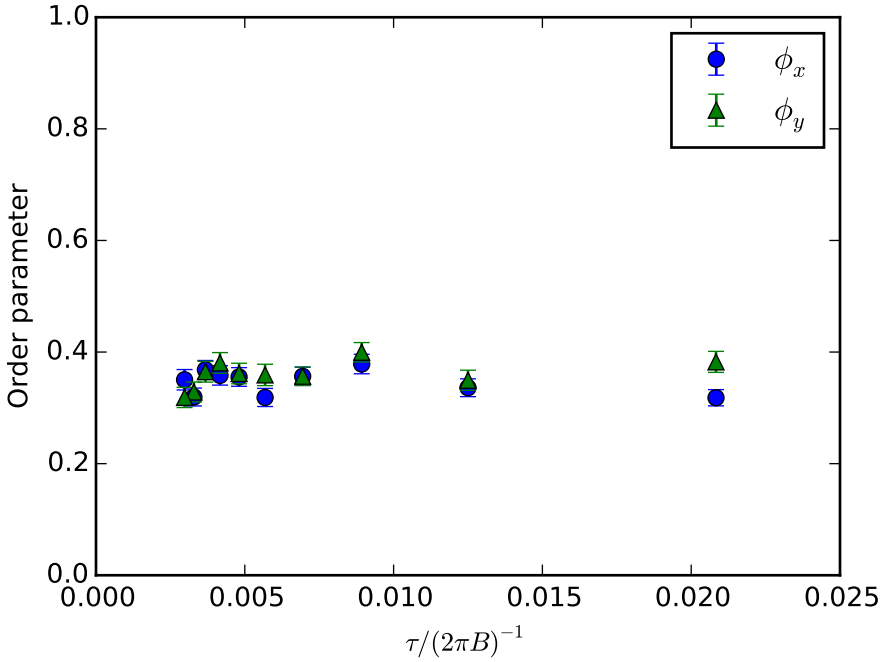

Figure 6.3: Demonstration of the convergence of the quantities $\phi_x = \langle n_{x\text{-stripe}} \rangle$ and $\phi_y = \langle n_{y\text{-stripe}} \rangle$ with respect to the imaginary time step, τ, for a 7×7 lattice of dipoles with $g = 100$. Having an odd number of rows and columns in the lattice explains the low values for ϕ_x and ϕ_y, which would be expected to be around $1/\sqrt{2}$ for a fully ordered system without boundary induced frustration.

Figures 6.1 and 6.1 demonstrate the convergence of the x- and y-stripe order parameters, $\phi_x = \langle n_{x\text{-stripe}} \rangle$ and $\phi_y = \langle n_{y\text{-stripe}} \rangle$, respectively, with respect to τ and β for a very strongly interacting system ($g = 100$) with no applied electric field. While both of these figures were generated with a 7×7 lattice, meaning the character of the order exhibited by these systems is different than is expected for systems with an even number of rows and columns due to the aforementioned frustration, this is unlikely to impact the convergence behavior of these simulations. This is because the convergence behavior at these interaction strengths is primarily impacted by the energy scales of the system which are not impacted by the boundary conditions.

The behavior of the combined ϕ_{xy} order parameter as the interaction strength g is increased at zero field is demonstrated in figure 6.1 for three different system sizes: 6×6, 8×8, and 9×9. Contrary to what was seen in 1D lattice systems for systems with 6 and 8 dipoles

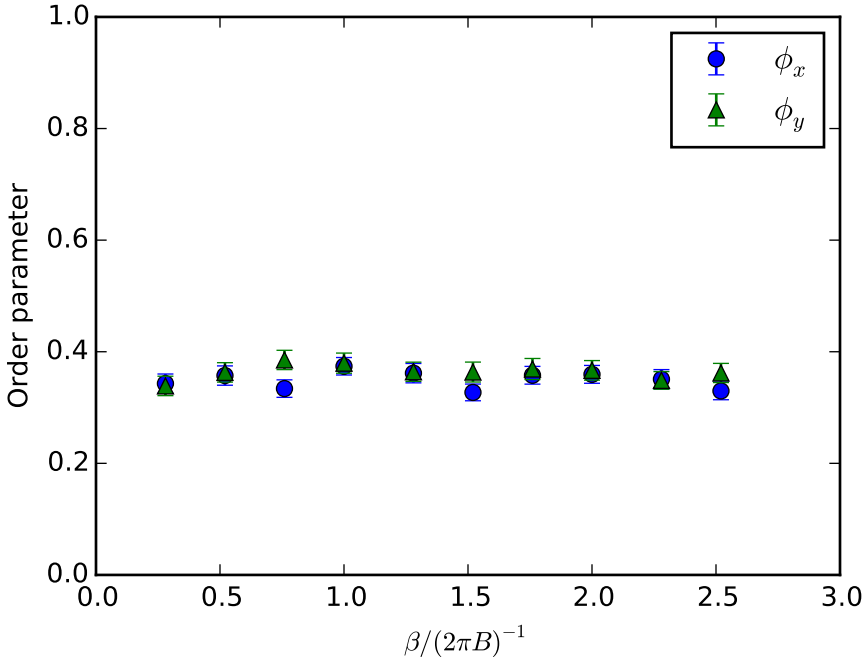

Figure 6.4: Demonstration of the convergence of the quantities $\phi_x = \langle n_{x\text{-stripe}} \rangle$ and $\phi_y = \langle n_{y\text{-stripe}} \rangle$ with respect to the imaginary time path length, β, for a 7×7 lattice of dipoles with $g = 100$. Again, having an odd number of rows and columns in the lattice explains the low values for ϕ_x and ϕ_y, which would be expected to be around $1/\sqrt{2}$ for a fully ordered system without boundary induced frustration.

(figure 5.2), here there appears to be very little difference between the 6×6 lattice and the 8×8 lattice. There could be for several reasons for this. One possibility is that it is possible that this system is simply converged, and does not exhibit strong finite sized effects. This being the case, it would appear that this is not actually an order-disorder phase transition but rather a gradual crossover from the non-interacting to the strongly interacting limit. The other possibility is that the system is poorly converged and exhibits strong finite-sized effects. This would not necessarily be surprising, since while the number of dipoles in the system almost doubles, the linear extent of the system increases only slightly. Since the dipole-dipole potential decays relatively slowly in two dimensions it is then possible that for all system sizes considered here, the furthest pair of molecules is still relatively strongly interacting. Without simulating significantly larger systems, which could be well beyond the current capacities of such PIGS simulations which are described below, trying to pin down the location of the transition, or indeed whether there is a phase transition at all or just a finite-sized crossover, is highly speculative. However, on the basis of these two data points it does appear that there is some sort of transition or crossover near $g = 2.5$.

Here it is instructive to briefly consider the computational demands of the PIGS method. Since the PIGS Monte Carlo method scales roughly quadratically with number of particles for systems with pairwise interactions, and doubling of the linear extent of the system requires quadrupling the system size, scaling up system size in two dimensions is already quite challenging, especially relative to one dimensional systems. One may be tempted to assume that this is no problem, since classical Monte Carlo simulations routinely simulate hundreds to thousands of classical particles [53], but there is a complication to PIGS that makes this comparison unfair. In addition to scaling with system size, it is also necessary to consider the number of time slices required for a PIGS calculation, especially for a strongly interacting system. For a strongly interacting system it is not uncommon to require on the order of 100 time slices. This means that for a system of 81 particles on the order of 8000 beads are being simulated, comparable to 8000 classical particles. A medium sized PIGS simulation is thus comparable to a relatively large classical simulation! Like classical Monte Carlo, PIGS is also quite parallelizable, and more sample configurations can be generated simply by running multiple copies of a simulation with different initial conditions in parallel. Nevertheless, the simulations in figures in this section took tens of thousands of CPU hours per data point to generate on a medium sized computational cluster.

One last thing to note is the behavior of the results for 9×9 lattices in figure 6.1. Despite the 9×9 system being only slightly larger than the 8×8 lattice in terms of linear extent, the maximum value of ϕ_{xy} actually *decreases* dramatically, the maximum value being essentially halved. This is a reflection of the fact that there is no simple way to form a striped phase where all nearest-neighbor interactions are purely attractive for this lattice size, highlighting the necessity of having an even number of rows and columns. Additionally, it would appear that in the case of the 9×9 lattice the system is not well characterized by any of the other simple orderings, *e.g.* the checkerboard ordering, or polarization along the x-, y-, or z-axes, *etc.*, as shown in figure 6.1; further study is required to determine if the system is ordered in another fashion not yet considered. Since this effect arises from inappropriate boundary conditions (because dipoles at the boundary are unable to achieve as many favorable nearest-neighbor interactions as molecules in the center of the simulation box, *i.e.* they experience frustration as discussed above) it is expected to diminish with system size. This is because the boundary length scales linearly with system extent, *i.e.* the number of rows and columns, and the area grows quadratically. Thus for larger system sizes the number of frustrated molecules will represent a smaller fraction of the total system.

6.2 Triangular lattices

Like square lattice systems, triangular lattice simulations can be used as a model for dipolar molecules confined to deep optical lattices, with dipoles still described by the Hamiltonian in eq. (6.1), with, again, $u = dE/(hB)$ and $g = C_{\mathrm{dd}}/(4\pi hBr_{\mathrm{lat}}^3)$ as in 1D systems. This geometry is particularly interesting since for completely polarized dipoles in two dimensions (with the polarization perpendicular to the plane of the system), or in quasi-2D geometries

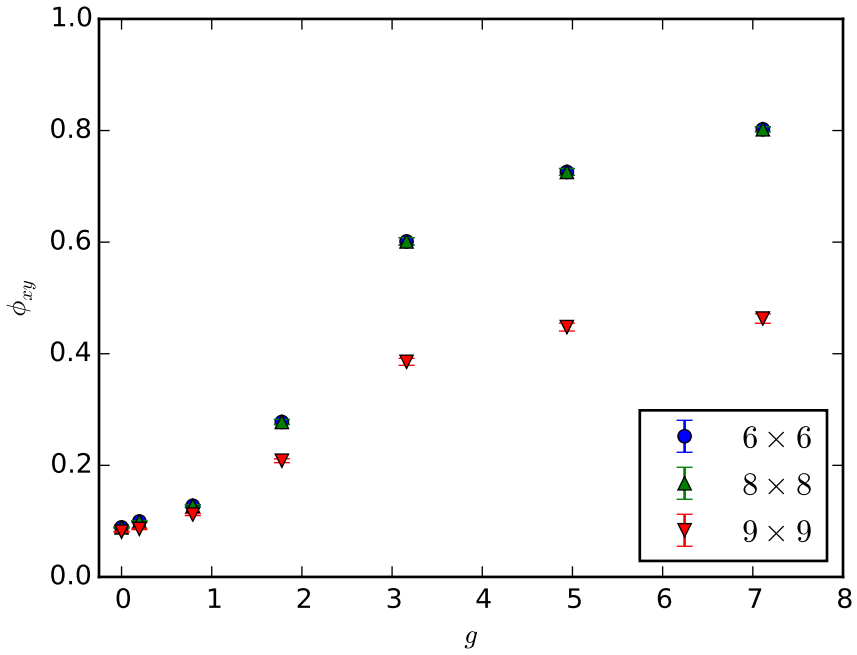

Figure 6.5: The order parameter, ϕ_{xy}, as a function of the interaction strength, g, with no applied field, *i.e.* $u = 0$, for 6×6, 8×8, and 9×9 lattices. From this plot it is evident that while going from a 6×6 to an 8×8 lattice represents almost a doubling in system size in terms of the number of particles, there is almost no difference in the behavior of ϕ_{xy}, due to strong finite size effects in 2D. Also of note is the fact that the effect of going from an 8×8 lattice to a 9×9 lattice actually results in a decrease in the polarization, a result of frustration due to an unphysical boundary condition (see text).

where there is tight confinement in the perpendicular direction, in the absence of an optical lattice potential the formation of a triangular crystalline phase is predicted [4, 74, 78]. In such systems, at densities typical of optical lattice experiments, where average nearest-neighbor intermolecular distances are on the order of ≈ 500 nm [25] and with non-vanishing static electric fields, *i.e.* for $g \ll 1$ and $u > 0$, it is reasonable to assume that the particles can be treated as perfectly polarized with some effective dipole moment that is related to an applied electric field, as previously discussed in the introduction of this chapter. However, as the density of such self-assembled crystals is increased, the validity of this assumption breaks down since the dipole-dipole potential energy scale for nearest-neighbor interactions becomes commensurate with the rotational energy scale, *i.e.* $g \approx 1$. Thus at a certain density the rotational degrees of freedom can no longer be neglected, and since the dipole-dipole potential energy can be attractive as well as repulsive it would seem that the stability of such systems then comes into question [73].

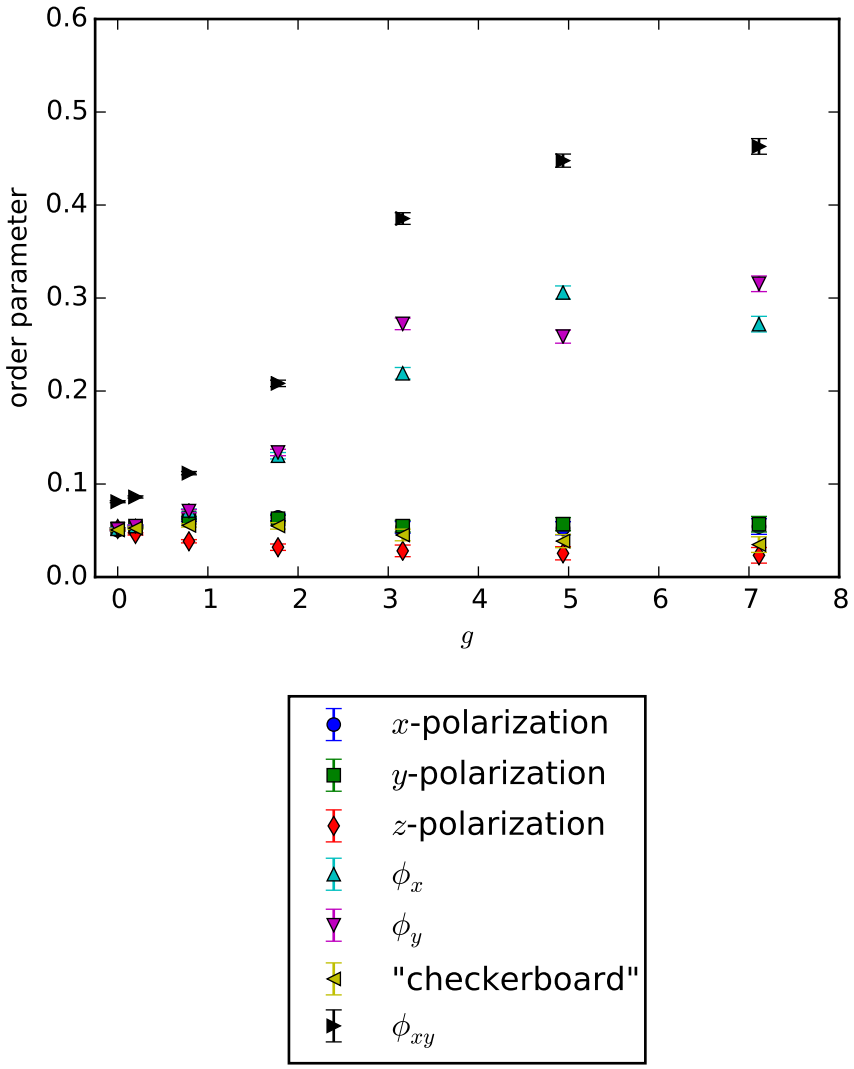

Figure 6.6: The checkerboard ($\phi_{\text{checkerboard}}$), fully polarized ($\phi_{j\text{-polarization}}$), and striped ($\phi_{xy}$) order parameters as a function of the interaction strength, g, with no applied field, *i.e.* $u = 0$, for a 9×9 square lattice system. The order parameters here are defined in equations (6.4) — (6.8).

Since the instability will arise from the dipolar molecules sampling the attractive portions of the dipole-dipole potential (see figures 1 and 1), which becomes favorable when $g \approx 1$ and $g > u$, dipoles held at fixed positions on a triangular lattice can be used as a simple model to probe the stability of self-assembled dipolar systems. Under this approximation, the onset of an ordered phase in which molecules are all polarized in the lattice plane would signal the collapse of the ensemble in the case that the dipoles were allowed to translate, since

the dipoles would then tend to stack up tip-to-tail in the direction of polarization, leading to an instability similar to that found in polarized ensembles with insufficient transverse trapping [73]. For a given dipole moment, the critical interaction strength, $g = g_c$, will be related to the lattice spacing and hence to a critical particle density; ensembles with densities above this density, ρ_c, will likely be unstable. It should be noted that because the dipoles are held fixed under the current model and in realistic systems they are free to translate, this estimate of ρ_c is likely an upper bound and to truly probe the instability in detail would require a careful study of simulations with both translations and rotations.

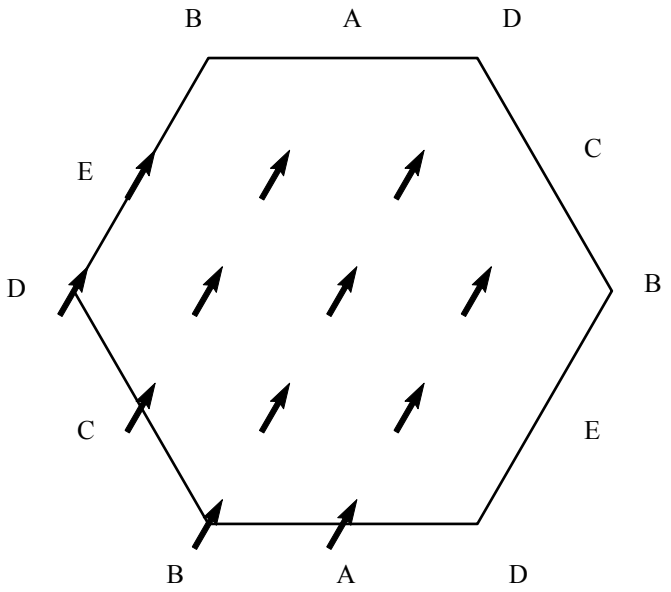

Figure 6.7: The geometry of the hexagonal periodic simulation box. Corresponding points on the boundary are labeled with the letters A – E.

More so than in the case of 2D square lattices, careful consideration must be given to the boundary conditions, to the extended periodic sums over lattice positions, and to what sorts of orderings are favored. Figure 6.2 shows the geometry of a hexagonal periodic simulation box, with corresponding points on the boundaries explicitly labeled. The proposed orderings, found by considering highly ordered and highly symmetric classical configurations, that are depicted in figure 6.2, include a possible striped and fully polarized ordering. Unlike in square lattices, there is no way to arrange a checkerboard pattern where all nearest-neighbor interactions are attractive on a triangular lattice.

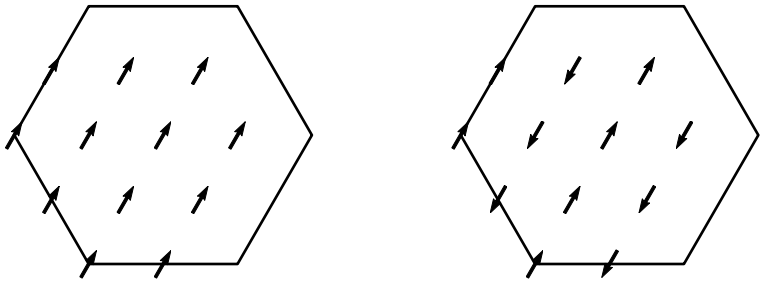

Figure 6.8: The considered orderings in the limit $g \gg 1$ and $u \ll 1$ for a system of 12 dipoles with the primary simulation box outlined for reference. On the left is a fully polarized ordering, which is degenerate with all other configurations that are fully polarized in the lattice plane, and on the right is one of six degenerate striped orderings, two along each of three triangular lattice axes. The dipoles not pictured on the right and top boundaries correspond to particles on the opposite boundary.

Shown in figure 6.2, utilizing the nearest image convention, are the energies of these proposed classical configurations. For the smallest system size, the striped configurations, two for each of three lattice directions, appear to be the lowest in energy. For larger systems and all systems with an extended periodic sum over periodic images, as described in the introduction of this chapter, using a sufficiently long cut-off, the lowest energy of the considered classical configurations are the fully polarized configurations, with all rotations about the (transverse) z-axis of the fully polarized configurations being degenerate as in the square lattice case.

In early simulations it was found that utilizing a rectangular simulation box with periodic boundaries to simulate the triangular lattice system led to breaking of the degeneracy of the fully polarized configurations pictured in figure 6.2, as well as a breaking of the degeneracy of the six equivalent striped configurations. Through experimentation it was found that utilizing a hexagonal periodic simulation box, the geometry of which is pictured in figure 6.2, was sufficient to restore these degeneracies. This highlights the fact that in two dimensional systems more than in one dimensional systems, because of the anisotropy of the dipole-dipole interaction and the rotational degrees of freedom, the effects of the geometry of a system must be taken into consideration when designing simulations.

Establishing that the lowest energy classical configurations are the fully polarized ones,

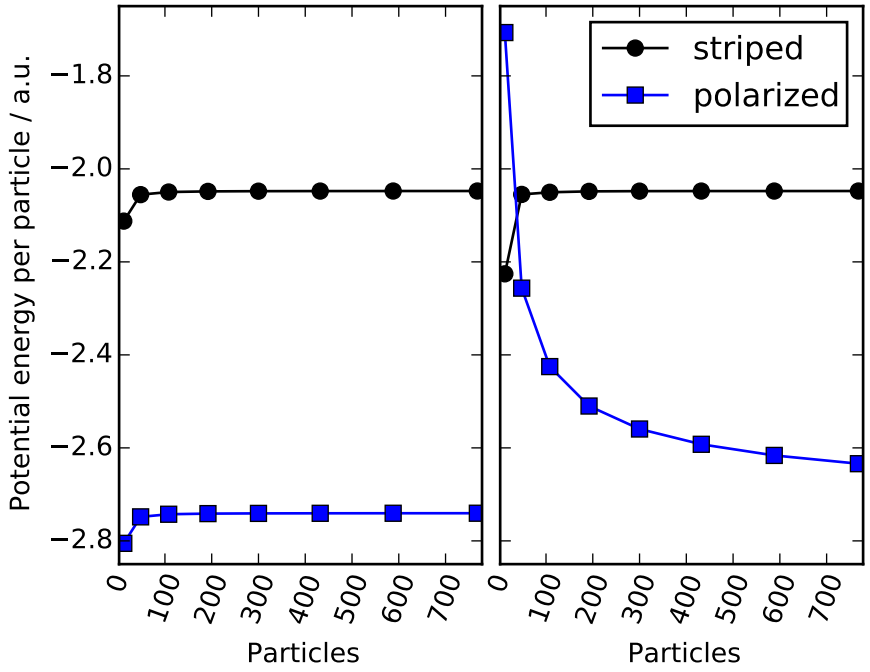

Figure 6.9: The classical potential energy per particle of striped and polarized configurations as a function of system size, with $C_{\mathrm{dd}}/(4\pi r_{\mathrm{lat}}^3) = 1$ a.u. and $u = 0$ in a hexagonal unit cell under the periodic sum convention with a cutoff radius of 100 lattice sites (left) and the minimum image convention (right). Notice that, as in the square lattice case (figure 6.1), the nearest image convention predicts erroneously that the striped configurations have lower potential energy than the fully polarized configurations for the smallest system size.

an order parameter which detects this ordering can be defined as

$$\phi_{\mathrm{pol}} = \left\langle \sqrt{\left(\frac{1}{N}\sum_{i=1}^{N} n_i^x\right)^2 + \left(\frac{1}{N}\sum_{i=1}^{N} n_i^y\right)^2} \right\rangle, \tag{6.9}$$

which measures the degree of total polarization of the system. Unlike the square lattice simulations an external electric field, applied along the z-axis (perpendicular to the lattice plane), is included. It is then interesting to track the degree of polarization in the z-direction with the signed order parameter

$$\phi_z = \left\langle \frac{1}{N}\sum_{i=1}^{N} n_i^z \right\rangle. \tag{6.10}$$

This does not require a root mean squared average since there is naturally a preferred direction.

As with our previous studies in chapter 5 as well as in section 6.1, it is necessary to establish convergence with respect to imaginary time step and imaginary time path length. This is demonstrated in figures 6.2 and 6.2, respectively. Convergence with respect to τ was tested for the case $u = 3$ and $g = 3$, depicted in figure 6.2. Convergence with respect to β was tested with $u = 3$ and a variety of values of g ranging from 0 to 3, and is summarized in figure 6.2. For both τ and β convergence a wave function formed by taking the product of single particle wave functions of the form described in eq. (5.13) was employed, with the single parameter, α, optimized for $u = 3$ as described in section 5.1. The behavior of $\phi_{\rm pol}$ as a function of τ shown in figure 6.2 is essentially as one would expect, varying roughly as $O(\tau^6)$ for small τ, consistent with the sixth-order propagator, eq (3.77), employed in these simulations. Also shown in figure 6.2 is the behavior of ϕ_z vs. τ. This shows that ϕ_z does not vary appreciably with τ, indicating that the behavior of this quantity is less dependent on the length of the small time step than is $\phi_{\rm pol}$.

Figure 6.2 (bottom panel) shows the behavior of ϕ_z as a function of β. When $g = 0$ (the non-interacting case) there is essentially no variation of ϕ_z with respect to β since the trial wave function employed, eq. (5.13), is a very good approximation to the exact ground state single particle wave function of the system, eq. (5.8). For all values of $g > 0$, ϕ_z decays roughly exponentially toward an asymptotic value which depends on the value of g, roughly as one expects based on the results of section 3.1. Also depicted in figure 6.2 (upper panel) is the behavior of $\phi_{\rm pol}$ as a function of β. This shows essentially the same sort of exponential decay toward and asymptotic value for $g = 0$ to 1 and from $g = 1.75$ to 3. The solid lines for $g = 1$ and $g = 1.75$ are drawn to guide the eye. At intermediate values there is more complicated behavior and especially at $g = 1.25$ it is not clear if $\phi_{\rm pol}$ has even converged at the longest β simulated. One possible explanation for this behavior is that for intermediate values of g the system is poorly described by a product of single particle wave functions, *e.g* if correlations between distant particles become important. This could indicate a greater correlation length for these values of g, a possible sign of a phase transition [68].

With suitable values for τ and β determined to ensure convergence of the quantities of interest (*i.e.* $\phi_{\rm pol}$ and ϕ_z), namely $\tau = 0.0375\ (2\pi B)^{-1}$ and $\beta = 5.1\ (2\pi B)^{-1}$, a series of simulations were run with variable g and u. First, examining the behavior of ϕ_z, shown in figure 6.2, it is seen that the transverse polarization decreases as the external field strength is decreased, and vanishes in the limit of no field. Also, as expected, the transverse polarization vanishes as the interaction strength is increased. The order parameter ϕ_z appears to decrease slowly, with no clear sharp transition from unpolarized to polarized, as will be seen in the behavior of $\phi_{\rm pol}$ over the same intervals, described below. This lack of a sharp transition for ϕ_z can be more easily seen in figure 6.2.

Turning to the behavior of $\phi_{\rm pol}$ in figure 6.2, it is seen that there does now appear to be a sharp crossover between a disordered regime at low interaction strengths and a regime characterized by a high degree of polarization in the lattice plane at higher interaction strengths. Examining figure 6.2 it appears that this crossover occurs near $g_c \approx 1$ for all field strengths. There does appear to be some variation of this crossover point with the external field strength but this variation appears to be only very weak. Interestingly, this transition

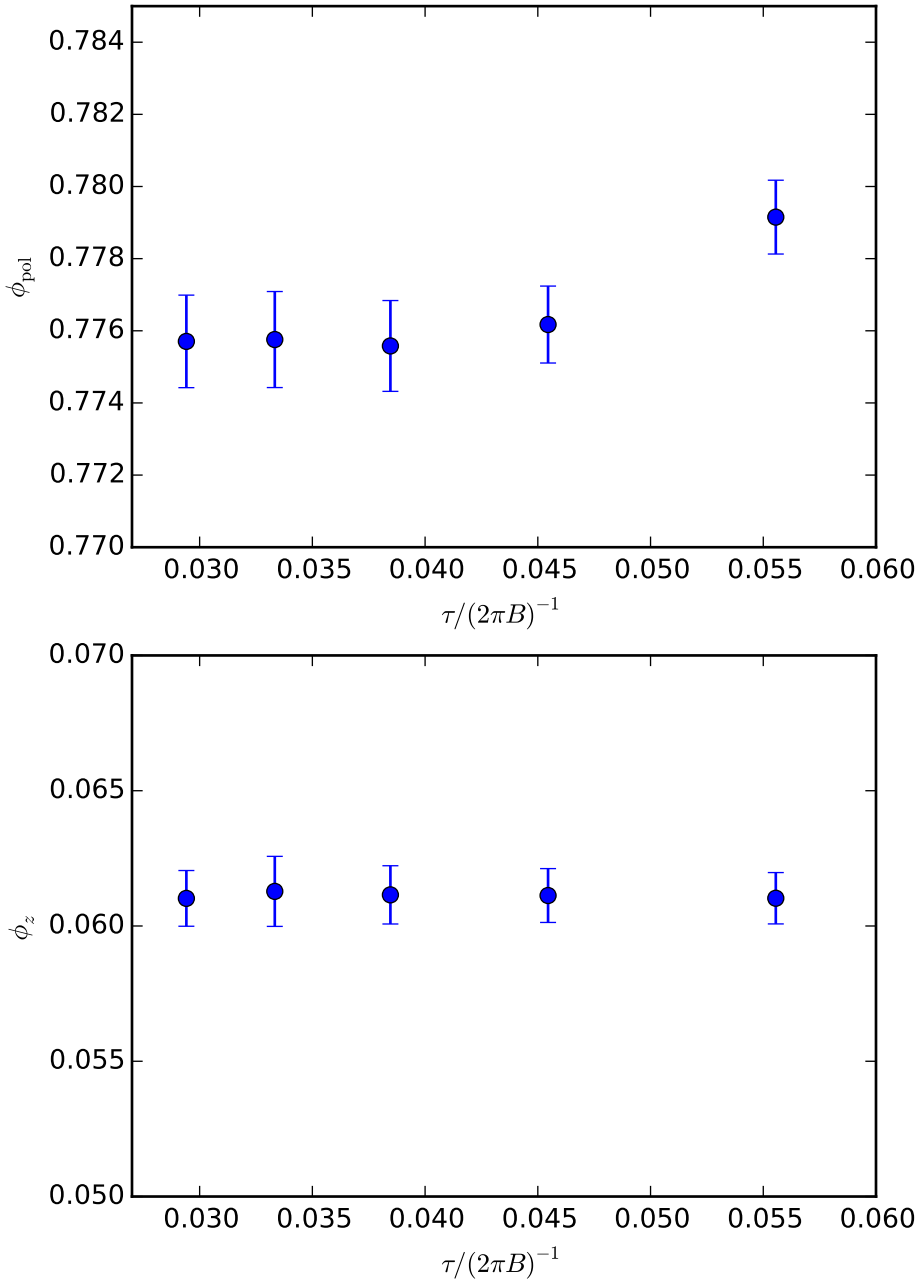

Figure 6.10: Convergence of the order parameters $\phi_{\rm pol}$ and ϕ_z with respect to τ for a system of 48 dipoles on a triangular lattice with $u = 3$ and $g = 3$, using a single particle trial wave function of the form in eq. (5.13).

from disorder to order occurs near the same value of g_c found for 1D lattice systems and is characterized by a similar type ordering in the ordered regime as was found in the case of

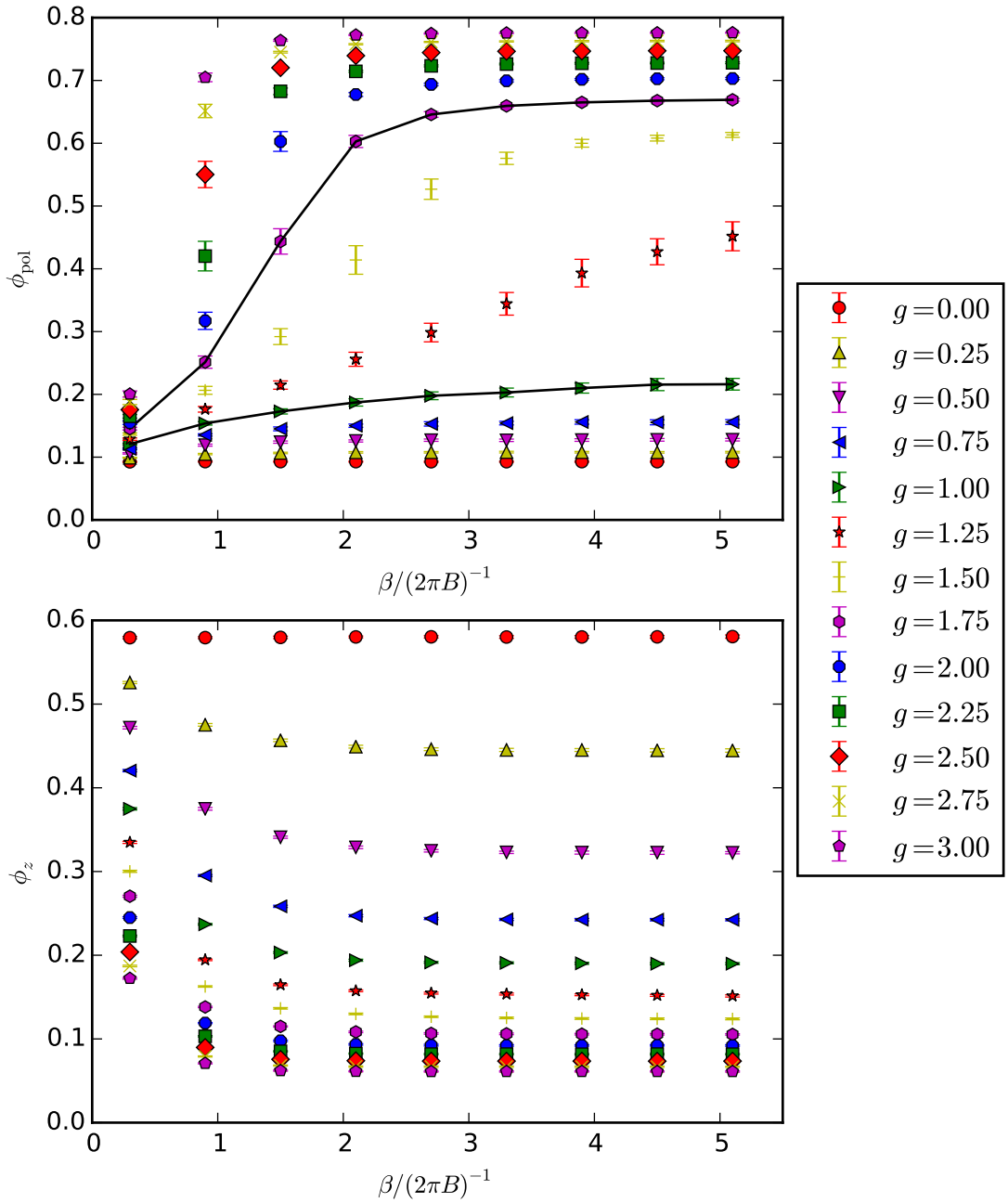

Figure 6.11: Convergence of the order parameters $\phi_{\rm pol}$ and ϕ_z with respect to β for a system of 48 dipoles on a triangular lattice with $u = 3$ and $\tau = 0.0375\ (2\pi B)^{-1}$, using a single particle trial wave function of the form in eq. (5.13). The lines highlight the limits of the transition region, see the text for a discussion of these result.

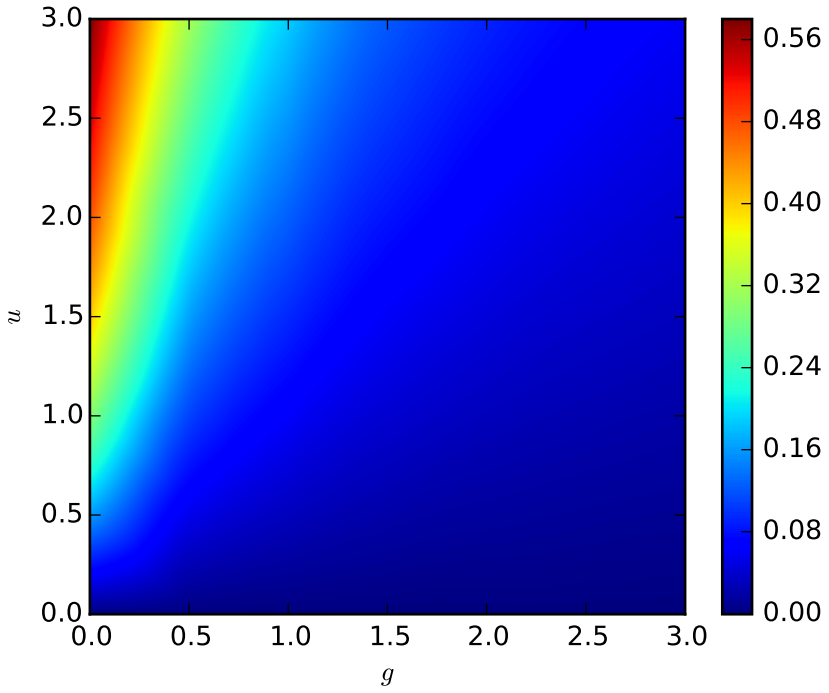

Figure 6.12: Transverse polarization, ϕ_z, vs. u and g for a system of 48 dipoles on a triangular lattice with $\beta = 5.1\ (2\pi B)^{-1}$ and $\tau = 0.0375\ (2\pi B)^{-1}$, using a trial wave function of the form in eq. (5.13). The quantity ϕ_z vanishes with vanishing electric field, $u = 0$, and also vanishes with increasing interaction strength, g.

1D lattice systems in the absence of external fields.

Of course it is necessary to perform simulations with larger system sizes to determine if this crossover is a phase transition or not, and to determine the precise value of g_c at which this transition occurs. Though it would be interesting to study the dependence of system size on this transition, at the very least these simulations demonstrate the existence of a crossover in a finite-sized system. It thus has applicability to finite clusters of molecules. In order to conclude anything more definitive it would be necessary to perform simulations of much larger system sizes. The allowable system sizes, based on the boundary conditions, are given by $N = 3K^2$, where K is an even integer. This means that after $N = 48$ particles, the next largest system size is $N = 108$ particles, more than a doubling of the number of particles, with the next system size larger than that being $N = 192$ particles. For the reasons outlined in section 6.1, this presents a challenge, computationally.

Nevertheless, because a crossover is observed, it strongly suggests that self-assembled dipolar crystals will exhibit the hypothesized instability, warranting further study including simulation of both rotations and translations simultaneously. It should be noted that for typical polar molecular species this crossover will occur at very small average intermolecular

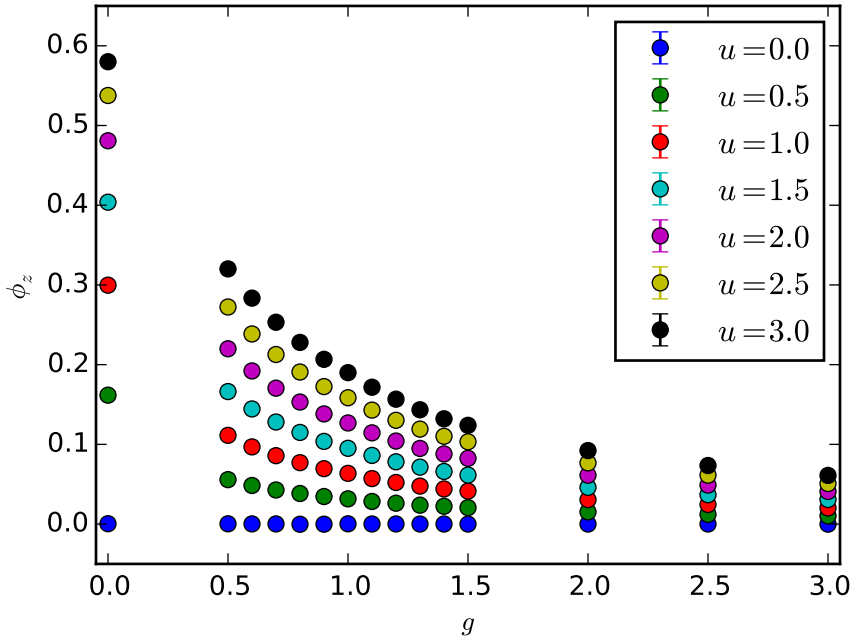

Figure 6.13: Transverse polarization, ϕ_z, vs. g for a system of 48 dipoles on a triangular lattice with $\beta = 5.1\ (2\pi B)^{-1}$ and $\tau = 0.0375\ (2\pi B)^{-1}$, using a trial wave function of the form in eq. (5.13). This shows the same data as in figure 6.2 but presented in a way to highlight the gradual decay of the z-polarization as the interaction strength is increased.

spacings, on the order of 10 nm, or equivalently, at very large densities. This suggests that for systems at experimentally relevant densities [25, 83], even with very weak external fields the crystalline phase will likely be quite stable.

6.3 PIGS simulations of dipolar molecular ensembles with translational degrees of freedom

Studying systems with both translational and rotational degrees of freedom to probe this stability, using PIGS simulations with both translational and rotational degrees of freedom, as described in chapter 3, has proven problematic thus far. A significant problem is that without a suitable trial wave function and short ranged repulsive potential, the simulations are often "trapped" in deep potential energy minima. This happens when an update translates or rotates a set of particles into a configuration where the dipole-dipole potential is attractive. Since the Metropolis algorithm on which the PIGS method relies always guarantees acceptance when transitioning from a less probable path to a more probable path (see

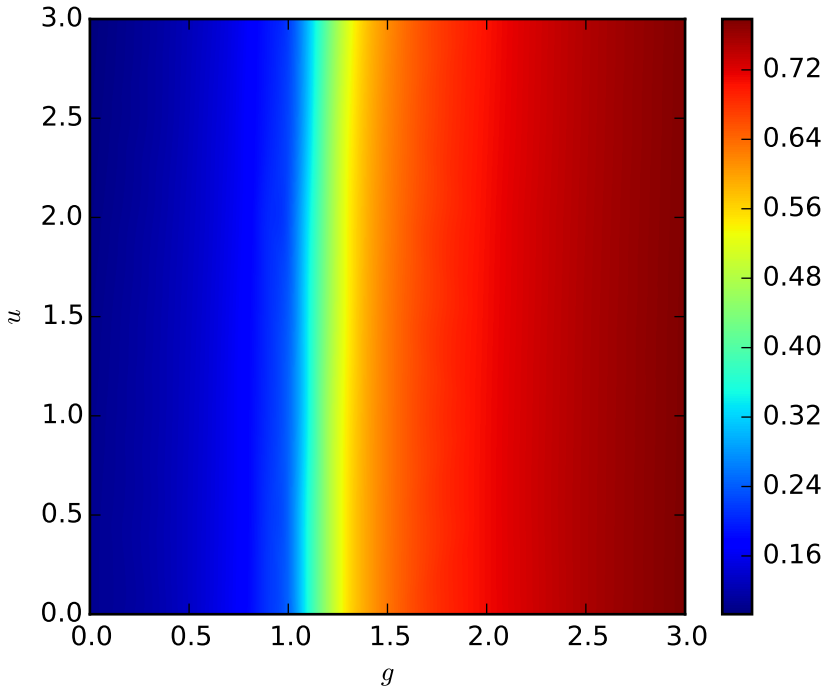

Figure 6.14: ϕ_{pol} vs. u and g for a system of 48 dipoles on a triangular lattice with $\beta = 5.1$ $(2\pi B)^{-1}$ and $\tau = 0.0375$ $(2\pi B)^{-1}$, using a trial wave function of the form in eq. (5.13). A sharp transition from $\phi_{\text{pol}} = 0$ to a finite value of ϕ_{pol} is found near $g \approx 1$ for all values of u.

section 3.2) and more probable paths tend to have lower potential energies because of the form of the propagator in eq. (3.72), such moves are likely to be accepted with near unit probability unless the particle has been moved a great distance and is rejected on the basis of the kinetic energy portion of the propagator. Once in one of these potential wells the odds of escape are slim, though not vanishing, assuming that the $1/r^3$ nature of the potential does not lead to a spurious floating point infinity value.

An example of this difficulty can be seen in simulations of the Hamiltonian for a system of two-dimensional translating and rotating dipoles in an external electric field and with a harmonic trapping potential confining them to the center of a harmonic trap,

$$H = \sum_{i=1}^{N} -\tilde{\lambda}\nabla_i^2 + \frac{\mathbf{L}_i^2}{\hbar^2} - un_i^z + \frac{w|\mathbf{r}_i|^2}{2} + g\sum_{j<i}\left[\frac{\mathbf{n}_i\cdot\mathbf{n}_j}{|\mathbf{r}_{ij}|^3} - 3\frac{(\mathbf{n}_i\cdot\mathbf{r}_{ij})(\mathbf{n}_j\cdot\mathbf{r}_{ij})}{|\mathbf{r}_{ij}|^5}\right], \tag{6.11}$$

where $\tilde{\lambda} = \hbar^2/(2mr_0^2hB)$, $w = m\omega^2 r_0^2/(hB)$, all distances are expressed in terms of r_0, and all energies expressed in terms of the rotational energy, hB. In this case, even for dilute systems with relatively strong transverse polarizing fields and relatively weak harmonic confinement, this collapse is observed when $g \approx 4.6 \times 10^{-4} \ll g_c \approx 1$.

Depicted in figure 6.3 is a plot of the radial pair distribution function for dipoles described by eq. (6.11) with $\tilde{\lambda} = 4.8 \times 10^{-5}$, $g = 4.6 \times 10^{-4}$, $w = 1.1 \times 10^{-10}$, and $u = 2.3$. In this case the trial wave function employed was of the form

$$\Psi(\mathbf{X}) = \prod_{i=1}^{N} e^{-\mathbf{r}_i^2/(2\sigma^2)+\alpha\cos\theta_i}, \tag{6.12}$$

where the variational parameter σ was optimized in the presence of dipole-dipole interactions between polarized dipoles and the parameter α was optimized considering only the interaction of a single dipole with an external field as described in section 5.1. This simulation was part of a series of simulations undertaken to determine suitable simulation lengths by computing simulation-time autocorrelation lengths for quantities of interest, in particular the radial distribution function, $g(r)$ [68], which is the probability, given a particle at the origin, of finding a particle a distance r away. Initially the simulation time autocorrelation time was found to be very long, especially for quantities that depend on the translational degrees of freedom and so larger magnitude moves were attempted to try to mitigate this effect. Over the course of these simulations it became apparent that the radial distribution function was being dominated by a feature at $r = 0$, the dominant peak in figure 6.3. This peak results from very many of the pairs of molecules being found at very small intermolecular separations, likely a result of the pairs being ensnared by the infinitely deep, attractive portion of the dipole-dipole interaction potential.

This can be somewhat mitigated, or at least the numerical issues fixed, by introducing either a suitable trial wave function which penalizes particles being very near one another, such as a Jastrow wave function [84], or a purely repulsive radially symmetric short range potential, perhaps of the form [75]

$$V_{\text{sr}}(r) = \frac{\sigma_{12}}{r^{12}}, \tag{6.13}$$

or both, since this would stabilize the system against collapse. In the latter case, which introduces a potential which is difficult to justify (or to simply parameterize) without microscopic calculations (see below), the system would naturally avoid pathological configurations where all dipoles are stuck on top of each other, thus avoiding the behavior demonstrated in figure 6.3. However, it would still be possible for the dipoles to all clump together at a new potential minimum, as shown schematically in figure 6.3 for a dipole-dipole potential with added short range repulsion. Without a trial wave function that explicitly penalizes this behavior, this tendency to form form clusters would certainly still exist. This would be a manifestation of the same collapse effect demonstrated in figure 6.3, albeit with much less risk of numerical stability issues during quantum Monte Carlo simulations.

There are many ways to design wave functions which discourage this sort of agglomeration of molecular dipoles. One popular trial wave function used to simulate molecular fluids is a variational Jastrow wave function with the McMillan pseudopotential [84],

$$\Psi_{\text{trial}}(\mathbf{X}) = \prod_{i=1}^{N}\prod_{j<i} e^{-\frac{1}{2}\left(\frac{b}{r_{ij}}\right)^a} \tag{6.14}$$

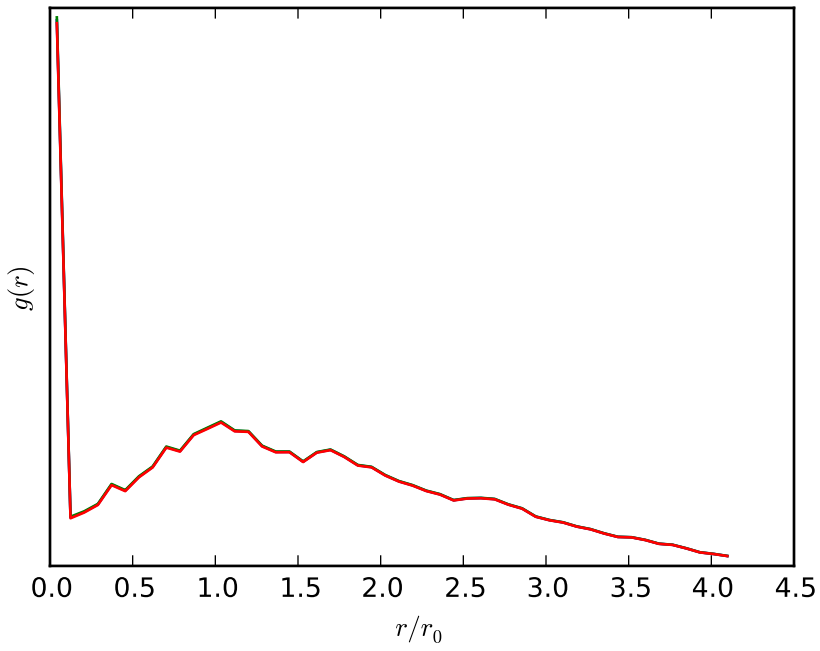

Figure 6.15: Plot of $g(r)$ for a system of 19 trapped polarized dipoles described by Hamiltonian (6.11) with $\tilde{\lambda} = 4.8 \times 10^{-5}$, $g = 4.6 \times 10^{-4}$, $w = 1.1 \times 10^{-10}$, and $u = 2.3$. Notice the peak at $r = 0$ indicating pairs of dipoles which lie directly on top of one another.

commonly used to simulate ultracold ^{4}He fluids [41] and clusters of molecular para-hydrogen [85]. This form of the wave function can be optimized variationally using variational Monte Carlo given a model potential to optimize the two parameters, b and a [84]. This form of the trial wave function discourages molecules from getting too close to one another, as desired, but, as written, does not account for any anisotropy in the interaction potential. Still, this form of the trial wave function may be useful, either in its own right or as a starting point for developing more complicated trial wave functions.

Optimization of a Jastrow trial wave function requires an accurate model potential, which can be accomplished by adding a carefully parameterized potential of the form in eq. (6.13) to the dipole-dipole interaction potential or by calculating the potential using *ab initio* quantum chemistry methods, as has been done for noble gas dimers [86]. The latter approach has the advantage of being somewhat easier to justify on the grounds of microscopic calculations at the expense of being more computationally demanding. To this end electronic structure calculations of the counterpoise-corrected [87] interaction potential energy of LiH–LiH, treating each of the two LiH units as rigid rotors, were performed using the quantum chemistry program Psi4 [88] using the CCSD(T)/aug-cc-pcVTZ method [89–91]. Under the interacting rigid rotor approximation with the intermolecular axis being defined to be along

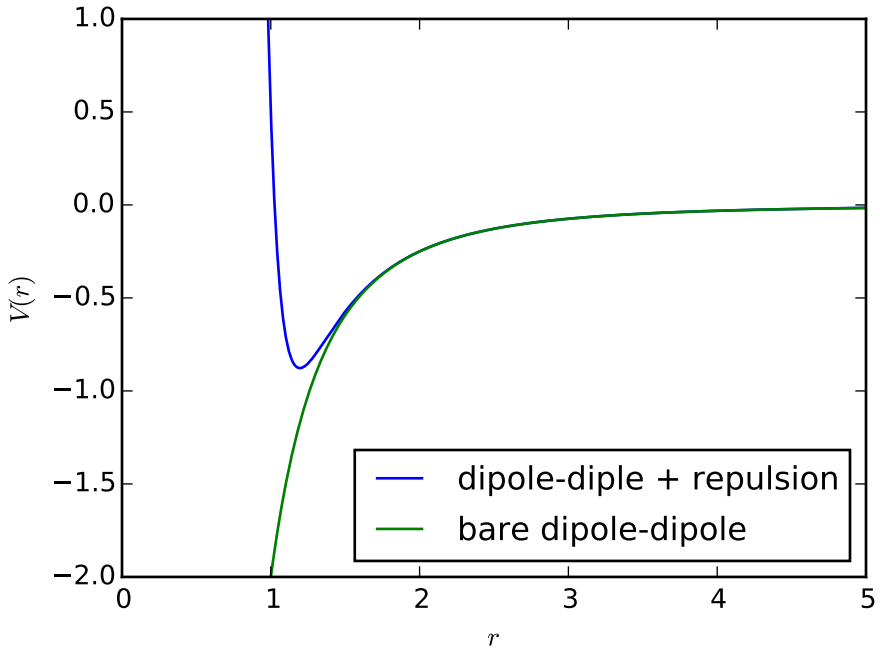

Figure 6.16: An example of how the dipole-dipole potential is modified by the addition of a short ranged repulsive potential of the form in eq. (6.13) for a configuration where both dipoles are parallel to the intermolecular axis, aligned tip-to-tail. Notice the potential minimum at some distance $r > 0$ replacing the infinite attraction at $r = 0$.

the z-axis the four internal coordinates of the system are the distance between the centers of mass of the two LiH molecules, r, the polar angle of the orientation of each of the molecules with respect to the intermolecular axis, $0 \leq \theta_A, \theta_B \leq \pi$, and the difference between the azimuthal angles of the orientations of the two molecules, $0 \leq \phi = \phi_A - \phi_B \leq \pi$. As described in reference [92] calculations of the interaction potential were carried out on an 11 point Gauss-Legendre grid in θ_A and θ_B, an 11 point Gauss-Chebyshev grid in ϕ, and a radial grid ranging from 4 to 15 Å in steps of 0.5 Å and from 15 to 30 Å in steps of 1 Å. After accounting for the cylindrical symmetry this grid contains 27,588 unique points.

To facilitate calculations with this potential it is necessary to have some method of interpolating between grid points. A function of the form [92]

$$V(r, \theta_A, \theta_B, \phi) = \sum_{L_A} \sum_{L_B} \sum_{L} v_{L_A L_B L}(r) A_{L_A L_B L}(\theta_A, \theta_B, \phi), \tag{6.15}$$

with

$$A_{L_A L_B L}(\theta_A, \theta_b, \phi) = \sum_{M=-\min(L_A, L_B)}^{\min(L_A, L_B)} \begin{pmatrix} L_A & L_B & L \\ M & -M & 0 \end{pmatrix} C_M^{L_A}(\theta_A, \phi) C_{-M}^{L_B}(\theta_B, 0), \tag{6.16}$$

where $C_M^L(\theta, \phi)$ are Racah normalized spherical harmonics, is used to describe the angular coordinates. The radial functions, $v_{L_A L_B L}(r)$, are constructed by first projecting the full potential energy function, $V(r, \theta_A, \theta_B, \phi)$, onto a particular angular function, $A_{L_A L_B L}(\theta_A, \theta_b, \phi)$, by evaluating the integral

$$v_{L_A L_B L}(r_i) = \int_0^\pi d\theta_A \int_0^\pi d\theta_B \int_0^\pi d\phi \, \sin(\theta_A) \sin(\theta_B) A^*_{L_A L_B L}(\theta_A, \theta_B, \phi) V(r_i, \theta_A, \theta_B, \phi) \quad (6.17)$$

at each of the radial quadrature points, r_i, using numerical integration of the potential $V(r, \theta_A, \theta_B, \phi)$. For each set of L_A, L_B, and L an interpolation between the points on the radial grid, r_i, is performed using the reproducing kernel Hilbert space method [92, 93]. To facilitate extrapolation of the potential energy at long ranges the radial potential energy functions were also fit to functions of the form [92]

$$v_{L_A L_B L}(r) = \sum_n - \frac{C_{L_A L_B L n}}{r^n}, \quad (6.18)$$

with the allowable values of n determined from physical considerations of the types of interactions that exist between pairs of molecules [92, 94], using a least squares fitting procedure. The short range and long range potentials can then be stitched together using a function which smoothly switches from the short range to the long range potential as described in reference [92]. A selection of the computed potential energy curves evaluated on the numerical grid is shown in figure 6.3.

The potential energy curves shown in figure 6.3 leave a bit to be desired, however. At the inner cutoff radius of 4 Å the interaction potential is still attractive for some configurations and there is no physically motivated way to extrapolate toward a separation of 0 Å in a way that yields a repulsive potential. Consequently the existing problems with purely attractive potentials remain. This suggests that current calculations should be extended to $r < 4$ Å where the potential should become repulsive due to Coulomb repulsion between the molecules.

Once the nature of the interaction potential at short range has been determined, then the potential may be used to variationally optimize a trial wave function of the form in eq. (6.14) as discussed above. While the pure Jastrow form of eq. (6.14) is not anisotropic, unlike the interaction potential, especially at intermediate ranges, this is expected to pose little problem as the repulsive potential at short ranges should be much less anisotropic than at intermediate ranges. Moreover, despite the lack of anisotropy this form of trial wave function should still discourage the unwanted clumping of dipoles by discouraging sampling of configurations where dipoles are very close to one another. If it turns out to be necessary, this form of trial wave function may be further reformed by changing the form to an anisotropic Jastrow wave function such as

$$\Psi_{\text{trial}}(\mathbf{X}) = \prod_{i=1}^{N} \prod_{j<i} e^{-\frac{1}{2} u(\mathbf{n}_i, \mathbf{n}_j, \mathbf{r}_{ij})} \quad (6.19)$$

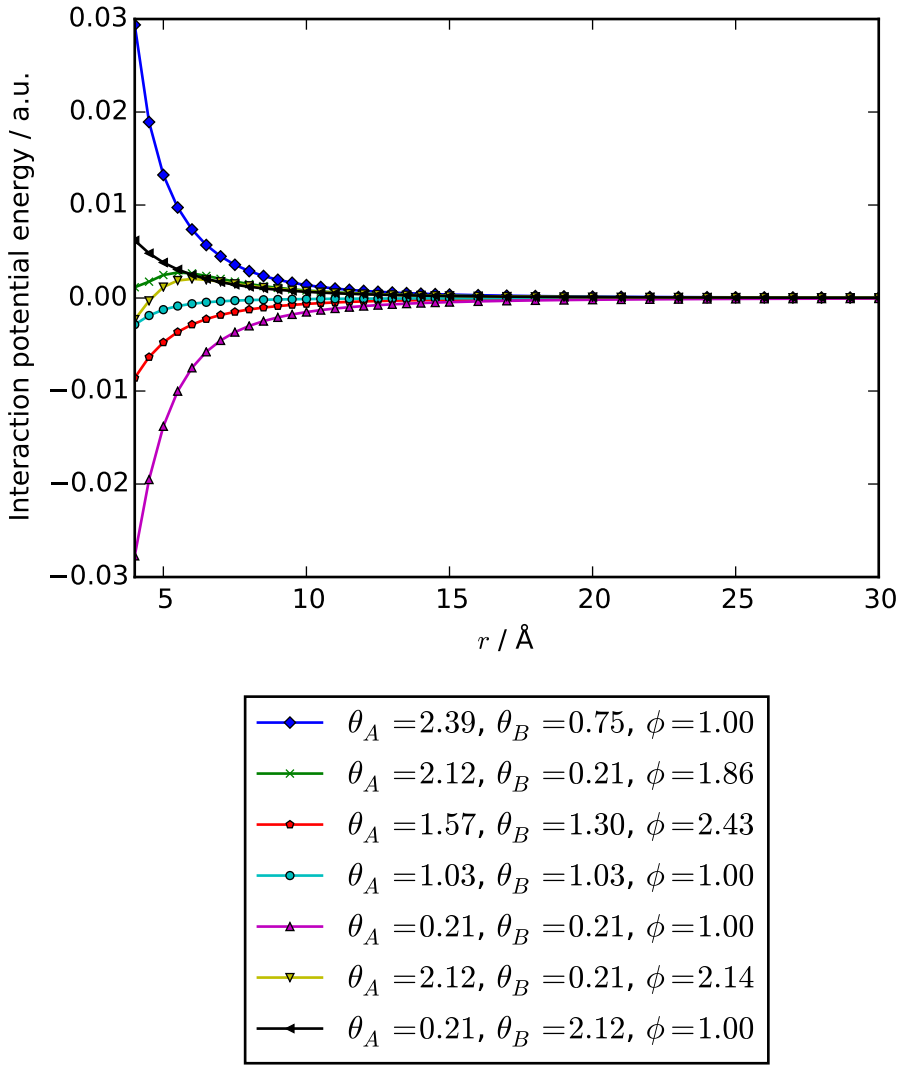

Figure 6.17: A sample of the counterpoise-corrected interaction potential for a pair of interacting LiH_2 molecules calculated at the CCSD(T)/aug-cc-pcVTZ level of theory. The angles describe the relative orientations of the pairs of molecules, with the coordinate system used described in the text. The inner cut off at 4 Å appears to be too large as there are still relative orientations where interactions are attractive.

with

$$u(\mathbf{n}_i, \mathbf{n}_j, \mathbf{r}_{ij}) = \frac{\alpha}{r_{ij}^{12}} + \beta \left(\frac{\mathbf{n}_i \cdot \mathbf{n}_j}{r_{ij}^3} - 3\frac{(\mathbf{n}_i \cdot \mathbf{r}_{ij})(\mathbf{n}_j \cdot \mathbf{r}_{ij})}{r_{ij}^5} \right), \tag{6.20}$$

where α and β are variational parameters to be optimized by using the variational Monte Carlo method, mentioned above. This form of trial wave function would introduce a degree of

anisotropy, building off the fact that the real interaction potential is expected to be roughly dipolar at intermediate distances.

Chapter 7

Engineering interactions with polar molecules

Because of the tunability and relatively long range of their interactions, ultracold polar molecules offer a route to controllably study a diverse set of phenomena. In contrast to ultracold atomic ensembles, which largely interact primarily through relatively short ranged van der Waals interactions that vary with distance as $1/r^6$, limiting the types of Hamiltonians that are realizable with atomic systems, polar molecules interact via the relatively long ranged dipole-dipole interaction potential. Furthermore, the nature and strength of this interaction can be modified through the careful application of external static and time-varying electric and magnetic fields. The anisotropy of the dipole-dipole interaction potential (see figures 1 and 1) may also conceivably be used to generate effective Hamiltonians which are not realizable with the isotropic van der Waals interactions of ultracold atoms. For these reasons, lattice confined cold and ultracold molecules have been proposed as an ideal platform to replace the more weakly interacting ultracold atomic ensembles in the study of models of condensed matter phenomena and quantum information processing [1, 95].

On the condensed matter phenomena side of things, there have been numerous proposals to study quantum magnetism, superfluidity, and exotic topological phases of matter [32] with dipolar molecules. Proposals have been made to simulate quantum spin models using open shell molecules, with a single unpaired valence electron, where the effective spin-spin interaction is mediated through a combination of the dipole-dipole interaction, modulated through the careful application of near-resonant microwave fields, and spin-rotational coupling [3, 96]. In these cases the nature of the interaction can be adjusted by changing both the tuning of the microwave field frequency as well as the polarization, allowing for the creation of a diverse set of spin textures [3]. Such interactions are naturally quite weak, although still stronger than those found in atomic systems, owing to the relatively large spacings between lattice sites in optical lattices (typically on the order of several hundred nanometers). However, the development of nanoplasmonic lattice technology [72] for polar molecules would pave the way for much stronger effective interactions with such open shell molecules.

In addition to utilizing an actual spin degree of freedom to realize effective lattice models,

there have been numerous other proposals to realize Hamiltonians important in solid state systems. For instance there are numerous proposals to generate effective Hubbard-type Hamiltonians using polar molecules [12–14], including models where a subset of the hyperfine states of closed shell molecules is used as the Hilbert space of an effective spin degree of freedom [15, 17]. Effective t-J type models have been proposed utilizing dressed rotational states of molecules confined to optical lattices [18, 19], which may offer an opportunity to study superconductivity on a highly tunable platform. Also utilizing these field dressed rotational states are models of quantum magnetism, including proposals to realize quantum XXZ models [21, 23, 24] and an actual experimental implementation of an effective XY model [25].

As well as providing an avenue towards realizing models of superconductivity or superfluidity and quantum magnetism, polar molecular ensembles confined to optical lattices have also been proposed as candidates for engineering tunable models of energy transfer in condensed matter systems. Optical lattice confined polar molecules have been the basis for a proposal for realizing a model of excitonic energy transfer with tunable impurity interactions using a dual species lattice of closed shell ($^1\Sigma$ ground state) polar molecules with the interactions being adjustable through application of static electric [97] and combined electric and magnetic fields [16]. Optical lattice confined molecules have also been proposed as platform for the realization of a system in which the interactions between excitons is tunable, also using optical lattice systems of $^1\Sigma$ ground state molecules with static electric fields [22]. The latter allows for the study of the role of exciton interactions in energy transfer in condensed matter systems. There have even been proposals to realize controllable models of energy transfer in the presence of a tunable phonon bath, where the bath arises naturally through the dipole-dipole interactions between molecules in adjacent optical lattice sites, effectively coupling the motion of molecules on different lattice sites [20].

Much of this work on quantum simulation with polar molecules goes hand-in-hand with proposals for quantum computation with trapped polar molecules. Again, as with quantum simulation, the chief advantage is the tunability of interactions between molecules. Lattice confined polar molecules in static electric fields with an appreciable gradient provide the oft-desired single-site addressability that allows for operations on single qubits, while the non-vanishing dipole-dipole interaction between polar molecules aligned in an external field provides a mechanism for generating entanglement [26, 27, 30]. Work has also been done on generating entanglement through the application of pulsed electromagnetic field interactions [29, 31] to entangle either pairs of molecules or molecules interacting with an auxiliary lattice filled with Rydberg atoms [28].

The uniting factor for all of these applications to the study of condensed matter phenomena and quantum information processing is that polar molecules can be utilized as a unique architecture for engineering interactions between particles at distance. This is due to their strong interactions with external electric fields and their relatively strong, long-ranged, and anisotropic interactions, compared to alternative platforms such as ultracold atomic ensembles.

This chapter begins with a proposal to realize a topological phase of matter in a system

of optical lattice confined polar molecules in section 7.1. Then in section 7.2 polar molecules confined to optical lattices are proposed as a platform to implement a a system possessing interesting spectroscopic behavior, with a phase transition from a phase exhibiting linear scaling of the single photon spontaneous emission for relatively weakly interacting systems to a phase exhibiting quadratic scaling of the single photon spontaneous emission rate for strongly interacting systems. Finally, a scheme for controllably generating entanglement in the rotational states of pairs of molecules is explored in section 7.3.

7.1 Hamiltonian engineering with $^2\Sigma$ ground state molecules

One of the most important considerations in the quantum information processing field is fault tolerance against environmental perturbations and against experimental imperfections. The introduction of minor errors due to the qubit states evolving under the influence of uncontrolled external factors such as stray electric or magnetic fields can lead to logical errors, leakage from the logical space, or decoherence of the qubit states, all of which result in the loss of information. The inability of real experiments to achieve perfect single qubit manipulations can also lead to incorrect operations being inadvertently performed. One theoretically promising avenue to deal with both of these problems at once is encoding the state of the system in a topological phase of matter [32]. A topological phase is characterized by a non-local order parameter and a finite gap between its (possibly degenerate) ground state(s) and all excited states and is naturally protected against local perturbations [32]. Excitations from the ground state in such systems are found to not necessarily be Bosons or Fermions but may be so-called "anyons" which possess fractional braiding statistics so that they make take on phases other than 1 or -1 under particle exchange; the braiding operation may even be used to enact universal quantum gate operations in the case of certain non-Abelian Anyons [32].

One particular example of a system that has a topological phase is the quantum dimer model on a triangular lattice at the RK point [98]. Such a quantum dimer model, though never found in nature, may describe the effective behavior of an extended Bose-Hubbard model, as described in refs. [99, 100]. This suggests a possible implementation with lattice confined dipolar molecules, since potential implementations of such models have been described previously in systems of dipolar molecules [1]. In this case the Hubbard model Hamiltonian is defined on a Kagome optical lattice [101] and is of the form [99, 100]

$$H = -\sum_{\langle i,j\rangle} t_{ij}\left(c_i^\dagger c_j + \text{h.c.}\right) + U_0\sum_i n_i^2 + U\sum_{i,j\in\hexagon} n_i n_j + V\sum_{i,j\in\bowtie,\notin\hexagon} n_i n_j, \tag{7.1}$$

with $V < U \ll U_0$, where the third term is a repulsive term due to two particles existing on the same "hexagon" and the fourth is a repulsive term due to two particles existing on the same "bow-tie" but on different "hexagons." The meaning of these two terms is illustrated

in figure 7.1. At 1/6th filling this model can be mapped onto a quantum dimer model on a triangular lattice such that the presence of a particle at a site represents a "bond" between the vertices at the centers of the two hexagons to which the site belongs [100].

The difficulty of implementing such a model in dipolar molecules is that while the interaction strength between all dipoles on the same hexagon must be the same, the distances are not. Furthermore, the bow-tie interaction must have a different interaction strength from all of the hexagon interactions, but the distance across the bow-tie is the same as the distance across the hexagon. Implementing such a set of interactions in a system where the effective interactions vary spatial as $1/r^3$ presents a challenge (this same challenge holds for implementations in systems dominated by bare Coulomb interactions, which vary with distance as $1/r$, or indeed with any interactions derived from such electrostatic interactions).

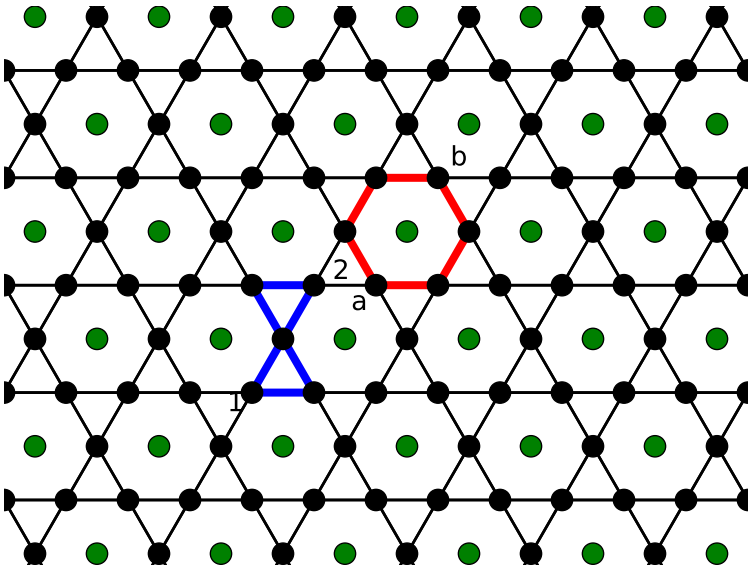

Figure 7.1: The Kagome lattice geometry with molecules at the black vertices. A "hexagon" is outlined in red, and a "bow-tie" is outlined in blue. The third term in eq. (7.1) is summed over all pairs of links like the segment beginning with point 1 and ending in point 2, which are the set of pairs of molecules located on the same bow-tie but on different hexagons. The challenge is in the fact that the distance from 1 to 2 is the same as the distance from a to b, and that the distance from a to b is different from the distances between a and its nearest neighbors on the same hexagon. Also pictured are the auxiliary lattice sites of the proposed emulation with dipolar molecules, colored green.

Implementing Hamiltonian (7.1) with systems of polar molecules can be done by trans-

lating the Hamiltonian into the language of spin-$\frac{1}{2}$ systems and then utilizing the approach outlined in reference [3]. Here, $^2\Sigma$ ground state molecules, possessing a single unpaired electron, are immersed in microwave fields which mix the field-free states, creating effective spin-spin Hamiltonians. Briefly, the Hamiltonian in ground vibronic state, and in the ground state of a deep optical lattice, can be written as

$$H_{\rm mol} = \sum_{i=1,2} \frac{\mathbf{N}_i^2}{2I} + \gamma \mathbf{N}_i \cdot \mathbf{S}_i + \frac{d^2}{r^3}(D_{11}^\dagger D_{2-1} + D_{1-1}^\dagger D_{21} - 2D_{10}^\dagger D_{20} + \text{h.c.}), \tag{7.2}$$

where the intermolecular axis has been taken to be the z-axis and $\mathbf{N}_i^2$ has been used to denote the rotational angular momentum operator (to emphasize that this is not the electronic orbital angular momentum) and γ is the spin-rotation coupling constant. Within the single molecule subspace of states $|(NS)JM_J\rangle$, with $N = 0$ and 1, the (dimensionless) dipole moment operator $\mathbf{D}^\dagger$ can be written as

$$\mathbf{D}^\dagger = \sum_{q=-1}^{1} (-1)^q |N=1 M_N = q\rangle\langle N=0 M_N = 0| \hat{\mathbf{e}}_q^*. \tag{7.3}$$

The ground four degenerate ground states of $H_{\rm mol}$ are the states $|g_i\rangle = |(0\frac{1}{2})\frac{1}{2}\pm\frac{1}{2}\rangle|(0\frac{1}{2})\frac{1}{2}\pm\frac{1}{2}\rangle$, with energy $E_g = 0$ and $N_1+N_2 = 0$ and the excited states with $N_1+N_2 = 1$ are $H_{\rm mol}|\lambda; r\rangle = E(\lambda; r)|\lambda; r\rangle$. By subjecting the pairs of molecules in the $N_1 + N_2 = 0, 1$ subspace to a continuous wave microwave field, it is possible to define an effective Hamiltonian through the use of second-order degenerate perturbation theory

$$H_{\rm eff}(r) = \sum_{i,j}\sum_{\lambda} |g_i\rangle\langle g_j| \frac{\langle g_i|H_{\rm mf}|\lambda; r\rangle\langle\lambda; r|H_{\rm mf}|g_j\rangle}{\hbar\omega - E(\lambda; r)} = \frac{\hbar|\Omega|}{8}\sum_{\alpha=0}^{3}\sum_{\beta=0}^{3} \sigma_1^\alpha A_{\alpha\beta}(r)\sigma_2^\beta, \tag{7.4}$$

where σ_i^α is the αth Pauli matrix acting on the ith spin ($\sigma^0 = \mathbb{I}$, $\sigma^1 = \sigma^x$, *etc.*) and the rotating wave approximation has been invoked. Here $H_{\rm mf}$ is the molecule-field interaction with a microwave field of frequency ω and $\hbar\Omega = d|\mathbf{E}|$,

$$H_{\rm mf} = \sum_{i=1,2}\left(\frac{\hbar\Omega}{2}\mathbf{D}_i^\dagger \cdot \boldsymbol{\epsilon} e^{-i\omega t} + \text{h.c.}\right). \tag{7.5}$$

Realizing a given spin-spin Hamiltonian is reduced to tuning microwave radiation of a particular polarization to a particular transition between $|g_i\rangle$ and $|\lambda; r\rangle$ for a given distance, the recipes for which are found in reference [3].

The term in eq. (7.1) proportional to U_0 can be naturally realized for very large U_0, *i.e.* $U_0 \to \infty$, enforcing no more than a single particle per site, by establishing the mapping between angular momentum projection, $|M_J| = \frac{1}{2}$ in the ground state, and particle number, with angular momentum projection $+\frac{1}{2}$ denoting the presence of a particle and angular momentum projection $-\frac{1}{2}$ denoting the absence of a particle. This effectively restricts the

model to the "hard-core" regime characterized by at most a single particle on each lattice site. Taking the lattice to lie in the xy-plane, the z-axis to be the quantization axis, and the x-axis to be the intermolecular axis, the hopping term can then be written as

$$-t\left(c_1^\dagger c_2 + c_2^\dagger c_1\right) = -\frac{t}{2}\left(\sigma_1^x\sigma_2^x + \sigma_1^y\sigma_2^y\right). \tag{7.6}$$

This hopping term can be realized using the methods in reference [3]. Terms of the form $n_i n_j$ can be expressed as

$$V_{12}n_1n_2 = \frac{V_{12}}{4}\left(\sigma_1^z + \mathbb{I}\right)\left(\sigma_2^z + \mathbb{I}\right) \approx \frac{V_{12}}{4}\left(\sigma_1^z\sigma_2^z + \sigma_1^z + \sigma_2^z\right), \tag{7.7}$$

where a constant shift has been neglected. Terms of this form are also amenable to the methods of reference [3] which allow the simulation of the term $\sigma_1^z\sigma_2^z$, while application of a weak constant magnetic field along the z-axis naturally provides a term

$$H_{\mathrm{m}} = g_S\mu_B B_0 S_z \propto \sigma^z, \tag{7.8}$$

with μ_B the Bohr magneton and $g_S \approx 2$ the electron g-factor. However, because the interactions described above are purely distance dependent, for the reasons outlined above, this method is unsatisfactory for realizing all of the interactions in eq. (7.1). It may nevertheless be used to generate the bow-tie interactions, since all bow-tie interactions occur at the same distance. The hexagon interactions are then left to be generated by another method.

One method of introducing hexagon interactions of the proper form is to introduce an auxiliary triangular optical lattice, the sites of which are near the center of each hexagon on the primary lattice, but which sits slightly out of the plane of the primary lattice. It is through the polar molecules on this auxiliary lattice that the hexagon interactions will be mediated [102].These auxiliary lattice sites are pictured as green dots in figure 7.1. The effect of the hexagon interaction is to create an energy penalty for multiple particles (multiple molecules with angular momentum projection $M_J = +\frac{1}{2}$ in the underlying physical implementation) on the same hexagon: this can be accomplished through a term of the form

$$\frac{V_A}{2}(\sigma_1^z + \mathbb{I})\sigma_A^x = \frac{V_A}{2}\left(\sigma_1^z\sigma_A^x + \sigma_A^x\right) \approx \frac{V_A}{2}\sigma_1^z\sigma_A^x, \tag{7.9}$$

where the A label refers to a molecule on the *auxiliary* lattice site. Since the central site is the same distance to all of the sites on the hexagon this will naturally produce a uniform hexagon interaction. The strategy then becomes one of implementing this Hamiltonian to create the dominant hexagon terms and then ensuring that all other interactions, namely the bow-tie interaction, are weaker.

Unfortunately terms like $\sigma_1^z\sigma_A^x$ present a challenge for the method in reference [3] if all of the molecules employed are the same species, since that method naturally produces interactions which are symmetric with respect to the swapping of particle indices. It was found previously that using molecules of a different species and using isotopomers of the molecules

on the primary lattice breaks this symmetry but produces insufficient energetic differentiation between hexagons and bow-tie interactions [102]. One possibility to get around this would be to differentially shift the rotational levels of the molecules on the auxiliary lattice using the AC Stark effect, through application of a far detuned laser field that illuminates only the auxiliary molecules. As described in chapter 2 the AC Stark effect Hamiltonian, neglecting the scalar light shift, is

$$H_{\mathrm{AC}} = -\frac{1}{6}\left|\mathcal{E}_0\right|^2 \Delta\alpha(\omega) C_0^2(\theta,\phi), \tag{7.10}$$

and the resulting shifts of the coupled states $|\,(NS)\,JM_J\rangle$ are

$$\langle (NS)JM_J|H_{\mathrm{AC}}|(NS)JM_J\rangle = \\ -\frac{\left|\mathcal{E}_0\right|^2 \Delta\alpha(\omega)}{6}\sum_{M_N}\sum_{M_S}\left|\langle N\,M_N, S\,M_S|J\,M_J\rangle\right|^2 \frac{N(N+1)-3M_N^2}{(2N-1)(2N+3)}. \tag{7.11}$$

The $|J=\frac{1}{2}M_J=\pm\frac{1}{2}\rangle$ states are unshifted and only the states with $J=\frac{3}{2}$ are shifted. The shift in these energy levels depends only on the magnitude of the projection M_J, with states with $|M_J|=\frac{1}{2}$ being shifted down in energy and states with $|M_J|=\frac{3}{2}$ being shifted up. It should be noted that while the two-body states consisting of a shifted molecule at the auxiliary site and a molecule on the regular lattice are no longer symmetric with respect to the swapping of particle indices, the total angular momentum projection along the intermolecular axis remains a good quantum number, since the cylindrical symmetry of the system is unchanged. So while the recipes contained in reference [3] no longer apply, the general approach of finding only states of a given angular momentum projection $Y = M_{N_1} + M_{N_2} + M_{S_1} + M_{S_2}$ and diagonalizing Hamiltonian (7.2) in this subspace to find the states $|\lambda;r\rangle$, which are then used in eq. (7.4) to generate the effective spin-spin interaction through second order perturbation theory still holds.

This effect can produce the asymmetry needed to engineer interactions of the form in eq. (7.9), with a degree of tunability given by modulating the strength of the applied far off-resonant field. In practice the strength of the interactions produced by this approach appears to be limited. It was discovered that by using laser fields with polarization in the lab frame of $\mathbf{e}_F = \mathbf{e}_+ - i\mathbf{e}_0 - \mathbf{e}_-$ tuned near the resonance between the ground state and the states $|\lambda;r\rangle$ with $|Y|=1$ that interactions of the form in eq. (7.9) could be obtained [103] using eq. (7.4). Preliminary calculations suggest that this method of generating hexagon interactions results in strengths on the order of 10 Hz or so for optical lattice spacings on the order of 500 nm with CaCl molecules [103] (the bow-tie interactions can be made to be much smaller than this). This is roughly the same order of magnitude interaction strength as can be achieved by established methods to simulate eq. (7.1) using Josephson junction arrays [104].

7.2 Condensed matter simulations with ultracold polar molecules

Another interesting potential application of ultracold ensembles of dipolar molecules is for the simulation of Hamiltonians relevant to intermolecular charge transfer in molecular aggregates [105]. A regular 1D array of N 2-level molecules coupled to their nearest neighbors through a dipole-dipole interaction is described by the Hamiltonian [106]

$$H_{\mathrm{KMM}} = \sum_{i=1}^{N} \varepsilon P_i^\dagger P_i + b\left(P_i^\dagger + P_i\right)\left(P_{i+1}^\dagger + P_{i+1}\right) \tag{7.12}$$

$$= \sum_{i=1}^{N} \frac{\varepsilon}{2}\left(\sigma_i^z + \mathbb{I}\right) + b\sigma_i^x\sigma_{i+1}^x, \tag{7.13}$$

where $P_i^\dagger$ is the Fermionic creation operator for an excitation on site i, ε is the gap between the ground and first excited state for a single molecule, b is the strength of the dipole-dipole coupling. The creation and annihilation operators in eq. (7.12) obey the following commutation relations:

$$[P_i, P_j] = [P_i^\dagger, P_j^\dagger] = 0, \tag{7.14}$$

$$[P_i, P_j^\dagger] = [P_i^\dagger, P_j] = 0, \tag{7.15}$$

$$\{P_i^\dagger, P_i\} \equiv P_i^\dagger P_i + P_i P_i^\dagger = \mathbb{I}, \tag{7.16}$$

with $i \neq j$. Using the Pauli matrices to define the operators [36]

$$\sigma_j^+ = \frac{1}{2}\left(\sigma_j^x + i\sigma_j^y\right), \tag{7.17}$$

$$\sigma_j^- = \frac{1}{2}\left(\sigma_j^x - i\sigma_j^y\right), \tag{7.18}$$

which obey the commutation relations

$$[\sigma_i^-, \sigma_j^-] = [\sigma_i^+, \sigma_j^+] = 0, \tag{7.19}$$

$$[\sigma_i^-, \sigma_j^+] = [\sigma_i^+, \sigma_j^-] = 0, \tag{7.20}$$

$$\{\sigma_i^+, \sigma_i^-\} = \mathbb{I}, \tag{7.21}$$

the connection between eq. (7.12) and a transverse field quantum Ising model, eq. (7.13), is obtained by identifying $P_i = \sigma_i^-$ and $P_i^\dagger = \sigma_i^+$ and using the relations

$$\sigma_i^- + \sigma_i^+ = \sigma_i^x, \tag{7.22}$$

$$\sigma_i^+\sigma_i^- = \frac{1}{2}\left(\sigma_i^z + \mathbb{I}\right). \tag{7.23}$$

Eq. (7.12) is found to have a phase transition from a phase with a disordered ground state to a phase with ferroelectric or antiferroelectric ordering of the transition dipoles in the ground state at $B \equiv 2|b|/\varepsilon = 1$ for infinite system sizes [106] analogous to the well known quantum phase transition found in the transverse field quantum Ising model [64]. Furthermore this model, which constitutes an extension of the commonly used Heitler-London approximation, in which the terms proportional to $P_i^\dagger P_{i+1}^\dagger$ and its Hermitian conjugate are ignored, exhibits novel spectroscopic behavior such as coupling between the ground state and all states of opposite parity, including multi-exciton states, through single photon transitions as well as linear (quadratic) scaling of the single photon spontaneous emission rate with system size for $B < 1$ ($B > 1$), termed superradiance [105], with a quantum phase transition between the two at the critical point $B_c = 1$. Because of the spectroscopic properties of a system governed by Hamiltonian (7.12), such systems could have applications as sensitive light sensors or harvesters, efficiently absorbing photons at very low levels [105].

Polar molecules, with their tunable interactions, seem a natural choice in which to study this model Hamiltonian, potentially allowing access to the strong coupling regime ($B > 1$) which is inaccessible with dipole coupled electronic states of molecular aggregates [107]. The form of eq. (7.13) suggests an implementation in $^2\Sigma$ ground state molecules using the methods of reference [3] with the addition of an extra magnetic field, as described in section 7.1. Hamiltonian (7.12) can also be simulated with $^2\Sigma$ ground state molecules in an intense far off-resonant continuous wave (CW) laser field and a static magnetic field [31]. The latter is described here.

In the presence of a strong far off-resonant CW laser field and static magnetic field $^2\Sigma$ ground state molecules evolve according to the Hamiltonian

$$H_{\rm mol} = \sum_{i=1}^{N} \frac{\mathbf{N}_i^2}{2I} + \gamma \mathbf{N}_i \cdot \mathbf{S}_i + g_S \mu_B B_0 S_i^z - \frac{|\mathcal{E}_0|^2 \Delta\alpha(\omega)}{6} C_0^2(\theta_i, \phi_i) + \sum_{j<i} V_{\rm dd}(\mathbf{r}_{ij}, \mathbf{n}_i, \mathbf{n}_j), \quad (7.24)$$

in which all the terms have been previously defined and the scalar light shift has been neglected as it shifts all states uniformly. Defining the states

$$|g\rangle = |N = 0 M_N = 0\rangle |S = \frac{1}{2} M_S = \frac{1}{2}\rangle \quad (7.25)$$

$$|g'\rangle = |00\rangle |\frac{1}{2} - \frac{1}{2}\rangle \quad (7.26)$$

the states

$$|D\rangle = \cos\phi |g\rangle - \cos\phi |g'\rangle \quad (7.27)$$

$$|e\rangle = \sqrt{1-a}|10\rangle|\frac{1}{2} - \frac{1}{2}\rangle - \sqrt{a}|1-1\rangle|\frac{1}{2}\frac{1}{2}\rangle, \quad (7.28)$$

with $a \approx \eta^2/2$, $\eta = \gamma/(g_s \mu_B B_0)$, and ϕ is a mixing angle in the absence of any of the applied CW fields, can be prepared via STIRAP as described in reference [31]. Within the

subspace of states $\{|D\rangle, |e\rangle\}$ when the gap between the states $E_e - E_D = \epsilon_e$ is very small the dipole-dipole interaction can be approximately expressed as

$$V_{\rm dd}(\mathbf{r}_{ij}, \mathbf{n}_i, \mathbf{n}_j) = b_{ij} \left(|e_i e_j\rangle\langle D_i D_j| + |e_i D_j\rangle\langle D_i e_j| + \text{h.c.}\right) \tag{7.29}$$

with

$$b_{ij} = \frac{1}{3}\frac{d^2}{r_{ij}^3}(1 - 3\cos^2\Theta)(1 - \eta^2)(1 - \delta^2), \tag{7.30}$$

where $\delta = |\pi/2 - \phi|$ and Θ is the angle between $\mathbf{r}_{ij}$ and the z-axis. The resulting Hamiltonian within this subspace is clearly of the same form as eq. (7.12) and as described in reference [31] the single-site energy $\varepsilon \equiv \epsilon_e$ can be reduced to zero with only modest magnetic and dressing laser fields, so that achieving arbitrary B (identifying $b \equiv b_{ij}$) is possible.

In order to detect superradiant emission from such a system it is necessary to overcome the long excited state lifetimes of rotational levels (for ^{7}LiH the spontaneous radiative lifetime of the first rotationally excited state is longer than 80 seconds [108]) by mixing state $|e\rangle$ with a vibrationally or electronically excited state with a much shorter radiative lifetime. This short-lived excited state, $|f\rangle$, can be coupled to state $|e\rangle$ via a weak CW laser near resonant with the transition frequency $\omega_{fe} = (E_f - E_e)/\hbar$ to form the superposition $|\psi\rangle = \sqrt{1-x}|e\rangle - \sqrt{x}|f\rangle$, with $x \ll 1$. If this state can quickly decay to state $|D\rangle$ and assuming the transition between states $|e\rangle$ is $|f\rangle$ is only weakly dipole allowed, then the effective spontaneous emission rate will be $\propto x\gamma_f$, where γ_f is the spontaneous emission rate of state $|f\rangle$. For alkaline earth monohalides the spontaneous emission rates for electronically excited states are on the order of 10 — 50 MHz [109], meaning that (utilizing the results of reference [105]) an array of 200 molecules with $x = 0.1$ and $B = 0.98$ (in the weak coupling regime, $B < 1$) will have a radiative lifetime on around 5×10^{-2} — 25×10^{-2} ns, which is further decreased to about 5×10^{-3} — 30×10^{-3} ns for $B = 1.4$ (in the strong coupling regime, $B > 1$), with the same number of molecules and mixing coefficient, x.

One caveat is that clearly in such a system the dipolar couplings extend past nearest-neighbors, unlike in eq. (7.12), decaying as $1/r^3$. In 1D the next nearest neighbor distance is twice the nearest neighbor distance, resulting in a reduction in the value of b_{ii+2} to $b_{ii+1}/8$ and quickly dropping off for further couplings. For smaller systems this may significantly impact the behavior of eq. (7.12) but for larger ensembles the behavior is expected to be unaffected qualitatively, since couplings decaying as $1/r^\alpha$ ($\alpha > 0$) in 1D transverse field Ising models, such as eq. (7.13), exhibit the same qualitative phase behavior as nearest neighbor and other short ranged couplings, a fact which has been demonstrated both theoretically [65, 110] as well as experimentally [111]. For dipolar couplings $\alpha = 3$, theoretical work has shown that the effect of non-nearest neighbor couplings is to shift the location of the critical point to $B_c \approx 1.2$ [110], where in this case B has been defined in terms of the nearest neighbor coupling, $B \equiv 2|b_{ii+1}|/\varepsilon$. In the case of variable longer ranged couplings (going as $r^{-\alpha}$, with $\alpha = 0.35$ — 3), experimentally the location of the critical point has been also been found to occur at $B_c \approx 1$ just as in the nearest neighbor transverse quantum Ising model, where

$B \equiv 2|b_{\rm avg}|/\varepsilon$ has in this case been defined in terms of the average coupling strength [111],

$$b_{\rm avg} = \langle b \rangle = \frac{1}{N-1} \sum_{j=2}^{N} b_{1j}. \tag{7.31}$$

7.3 Quantum information applications with ultracold polar molecules

In addition to being a potential platform for simulation of models of condensed matter phenomena, as discussed in the previous two sections, another field where the tunability of the interactions comes in handy is in the quantum information field. There exist numerous proposals to use polar molecules as qubits for either quantum memories or qubits in quantum computers, see, for example, refs. [26–31]. The chief advantage to polar molecule based quantum information schemes, aside from the tunability of their interactions, which allows molecules to selectively interact with one another at typical optical lattice distances through careful application of external fields, is the range of their interactions. This allows molecules in nearby optical lattice sites to be entangled without need to move them closer together. The only systems with comparable tunability and interaction range are highly excited Rydberg states of neutral atoms [112].

Recently a proposal was put forth to controllably generate entanglement in the rotational degrees of freedom of pairs of closed shell ($^1\Sigma$ ground state) polar molecules confined in deep optical lattices and subjected to intense pulsed laser fields [113]. In units of the rotational energy scale, hB, the Hamiltonian governing a pair of polar molecules in intense laser fields is

$$H = \sum_{i=1}^{2} \left(\frac{\mathbf{N}_i^2}{\hbar^2} - \frac{2}{3}\Omega_I(t) C_0^2(\theta_i, \phi_i) \right) + V_{\rm dd}(\mathbf{r}_{12}, \mathbf{n}_1, \mathbf{n}_2), \tag{7.32}$$

with $\Omega_I(t) = |\mathcal{E}_0(t)|^2 \Delta\alpha(\omega)/(4hB)$. The external field has the effect of aligning the molecules with the field polarization, in this case along the z-axis, meaning at typical optical lattice spacings, on the order of 500 nm, pairs of molecules are effectively non-interacting in the absence of an applied field. This is because the AC stark effect Hamiltonian, $H_{\rm AC} \propto C_0^2(\theta, \phi)$, mixes only states of the same parity and preserves the rotational angular momentum projection along the quantization (z-)axis, and so the induced dipole moment in the field field vanishes. The eigenstates of the single-particle portion of the Hamiltonian

$$H_{\rm mf} = \frac{\mathbf{N}^2}{\hbar^2} - \frac{2}{3}\Omega_I(t) C_0^2(\theta, \phi) \tag{7.33}$$

tend, at large intensities, toward nearly degenerate pairs of states separated from each other energetically and corresponding in the field-free limit to the rotational angular momentum states, $|NM_N\rangle$.

Identifying the states which correspond to $|00\rangle \equiv |g\rangle$ and $|10\rangle \equiv |e\rangle$ when $\Omega_I(t) = 0$, the dipole-dipole operator in the presence of an intense laser field in the two-particle subspace $\{|g_1g_2\rangle, |g_1e_2\rangle, |e_1g_2\rangle, |e_1e_2\rangle\}$ may be written as

$$V_{\rm dd}(\mathbf{r}_{12}, \mathbf{n}_1, \mathbf{n}_2) = \frac{\gamma(t)d^2}{4\pi\epsilon_0 r_{12}^3}(1 - 3\cos^2\Theta)\left(|g_1g_2\rangle\langle e_1e_2| + |g_1e_2\rangle\langle e_1g_2| + \text{h.c.}\right), \tag{7.34}$$

where $\gamma(t) = \left(\langle g|C_0^1(\theta,\phi)|e\rangle\right)^2$ (noting that the time dependence of $\gamma(t)$ comes from the time dependence of the states $|g\rangle$ and $|e\rangle$) and Θ is the angle between the z-axis and the direction of the intermolecular separation vector. From this it is clear that eq. (7.32) behaves an effective transverse field quantum Ising model

$$H_{\rm Ising} = \frac{\epsilon_e(t)}{2}(\sigma_1^z + \mathbb{I}) + \frac{\epsilon_e(t)}{2}(\sigma_2^z + \mathbb{I}) + J_{12}(t)\sigma_1^x\sigma_2^x, \tag{7.35}$$

with $\epsilon_e(t) = E_e(t) - E_g(t)$ and $J_{12}(t) = \gamma(t)d^2(1 - 3\cos^2\Theta)/(4\pi\epsilon_0 r_{12}^3)$ in intense laser fields. Hamiltonian (7.35) naturally decomposes into two 2×2 blocks with no matrix elements connecting them to one another, one for the subspace $\mathcal{S}_{2A} = \{|g_1g_2\rangle, |e_1e_2\rangle\}$ and another for the subspace $\mathcal{S}_{2B} = \{|g_1e_2\rangle, |e_1g_2\rangle\}$, both of which are easily diagonalizable. Since the objective is to create a pair of entangled molecules starting from two molecules in their ground rotational state, the relevant subspace happens to be $\mathcal{S}_{2A}$, the ground state of which is

$$|\psi_-(t)\rangle = \cos(\theta(t)/2)|g_1g_2\rangle - \sin(\theta(t)/2)|e_1e_2\rangle, \tag{7.36}$$

where $\tan\theta(t) = J_{12}(t)/\epsilon_e(t)$, with energy $E_-(t) = \epsilon_e(t) - \sqrt{(\epsilon_e(t))^2 + (J_{12}(t))^2}$. As ϵ_e(t) and J_{12}(t), and as a consequence θ(t), depend on the applied laser intensity it is possible to create arbitrary two-body entangled states of the form

$$|\psi(t)\rangle = a(t)|g_1g_2\rangle + b(t)|e_1e_2\rangle \tag{7.37}$$

by starting from a pair of molecules in their ground state and adiabatically increasing the intensity of the applied laser field. These two-body entangled states may then be probed spectroscopically for violations of Bell's inequality [113], an important test of the foundations of quantum mechanics [114].

The laser intensities required to form Bell pairs in typical polar molecules at optical lattice spacings are, however, quite intense, generally $> 10^8$ W/cm^2, exceeding the limits of what is possible to generate with continuous wave lasers. Reference [113] demonstrates that generation of maximally entangled pairs of molecules is also possible with pulsed lasers, in which much greater peak intensities are possible, though, in this case care must be taken to switch the laser on adiabatically, generally meaning that the pulse duration must be $\gg t_{\rm rotation} = (2\pi B)^{-1}$. For typical molecules, this is on the order of 10 — 100 ps. However, it was also shown that generation of Bell pairs generally requires that the pulse duration be on the order of the dipole-dipole interaction time-scale, $t_{\rm dd} = 4\pi\hbar\epsilon_0 r_{12}^3/d^2$, and this quantity is generally still 10s of nanoseconds at intermolecular separations on the order of

10 — 100 nm, with peak pulse intensities on the order of 10^9 — 10^{10} W/cm^2. This poses a problem, since optical lattice spacings are on the order of several hundred nanometers [25]. Even the spacings between wells in double well optical lattice are much greater than the $\approx$ 10 nm intermolecular separations required for this scheme to generate Bell pairs with reasonable laser intensities [115]. This issue might be mitigated through the development of nanoplasmonic lattices [72] for polar molecular species, since in that case intermolecular spacings on the order of 10 nm are predicted to be achievable, but this has not yet been realized.

Another potential solution to the problem of too large intermolecular separations is to simply move the particles closer to one another. Instead of confining each individual molecule in its own optical lattice site or its own site in a double well optical lattice to generate entangled pairs of molecules, it may be possible to start with two separate, parallel 1D optical lattices filled with the same species of polar molecules, then merge them into a single 1D lattice such that there are two molecules per lattice site, by displacing one of the two lattices. After the two lattices have been merged one of the lattices would then be turned off and a strong dressing laser turned on, causing the molecules to strongly interact with one another and become entangled. After the molecules have interacted for a sufficiently long time, the pairs of molecules, now entangled, may then be separated again into separate optical lattices and probed spectroscopically. Assuming that the initially separated molecules are each in the ground state of a roughly harmonic deep optical lattice site, it is possible to quickly move one of the two lattices without exciting the motions of the molecules in individual lattice sites (*i.e.* they will still be in the ground state of the trapping potential) at the end of the transport [116]. This assumes a transport protocol with linear acceleration of the trap minimum, $a_c(t)$, along the direction of motion given by

$$a_c(t) = \begin{cases} a_0 & \text{if } 0 \leq t < T/2 \\ -a_0 & \text{if } T/2 \leq t \leq T \\ 0 & \text{otherwise} \end{cases}, \tag{7.38}$$

with a total transport total transport time of $T = 4\pi n/\omega$, where ω is the harmonic trapping frequency and n is an integer [116].

Once both (translationally, rotationally, vibrationally, and electronically) ground state molecules occupy the same lattice site they will undergo inelastic collisions at the same time as they are being entangled. In this situation it is necessary only to ensure that the finite-width of the molecular wave packet representing the relative motion of a pair of molecules does not adversely affect the degree of entanglement generated. In fact, even if it were possible to generate an optical lattice with spacings on the order of 10 — 100 nm, it would still be necessary to ensure that the finite width of the single molecule translational wave function in the presence of the optical lattice potential does not adversely affect the degree of entanglement, which is sensitive to the distribution of distances between pairs of molecules.

In either case, the dynamics of the relative motion of the two molecules can be modeled

by a two-channel Hamiltonian of the form [117]

$$H_{\rm col} = -\frac{\hbar^2}{2\mu}\frac{d}{dR^2} - \frac{C_6}{R^6} + U_{\rm SR}(R) + \frac{1}{2}\mu\omega^2 R^2 + 2\epsilon_e(t)|e_1e_2\rangle\langle e_1e_2| + J_{12}(R,t)\left(|g_1g_2\rangle\langle e_1e_2| + \text{h.c.}\right), \tag{7.39}$$

where C_6 is the molecular van der Waals coefficient, μ is the reduced mass, $U_{\rm SR}(R)$ is a short ranged potential to model repulsion at short distances, taken to be an infinite potential step at $R = 0$, and ω is the harmonic trapping frequency. Here it has been assumed that collision energies are low enough that only s-wave scattering contributes to the collision dynamics. The state of the system is assumed to be of the form

$$|\Psi(t)\rangle = \int_0^\infty dR\left[\Phi_{gg}(R,t)|g_1g_2\rangle + \Phi_{ee}(R,t)|e_1e_2\rangle\right]|R\rangle, \tag{7.40}$$

where initially the $|e_1e_2\rangle$ channel is unpopulated. Both molecules are assumed initially to be in the ground states of their respective (approximately harmonic) potential energy wells before the collision begins so that their individual wave functions are Gaussian functions with width $\sigma_{\rm HO} = \sqrt{\hbar/(m\omega)}$ and initial positions r_a and r_b for particles 1 and 2, respectively. Under this assumption the initial form of $\Phi_{gg}(R,t)$ may also be assumed to be a Gaussian wave packet in $R = r_1 - r_2$ [117],

$$\Phi_{gg}(R, t=0) = (2\pi\sigma^2)^{-1/4} e^{-(R-R_0)^2/(2\sigma^2)+ik_0R}, \tag{7.41}$$

with width $\sigma = \sqrt{2}\sigma_{\rm HO}$ in the case of identical molecules, initial displacement $R_0 = r_a - r_b$, and initial velocity $v_0 = \hbar k_0/\mu$. The strong external field, which determines the variation of $J(t)$ and $\epsilon_e(t)$ with time, is assumed to have a Gaussian temporal profile, so that

$$\Omega_I(t) = \Omega_0 e^{-2(t/t_0)^2}, \tag{7.42}$$

where t_0 is related to the full-width at half-maximum of the pulse, $\tau_{\rm p}$, through $\tau_{\rm p} = 2t_0\sqrt{\ln 2}$. Additionally the intensity is assumed to be uniform over both molecules. The state $|\Psi(t)\rangle$ can then be propagated through time using standard wave packet propagation methods, such as the split-operator Fourier transform method as described in references [117, 118], which can be extended to handle time-dependent potentials [119]. Schematically this process is depicted in figure 7.3.

A key feature of these simulations is that, generally speaking, the initial wave packet width can be of the same order of magnitude as the other length scales involved in this problem. Such a broad distribution of intermolecular distances is expected to impact the degree of entanglement that will be possible to generate. The relevant length scales in this system, aside from the initial wave packet width, are the characteristic dipole radius,

$$R_{\rm dd} = \left(\frac{d^2}{4\pi\epsilon_0 hB}\right)^{1/3}, \tag{7.43}$$

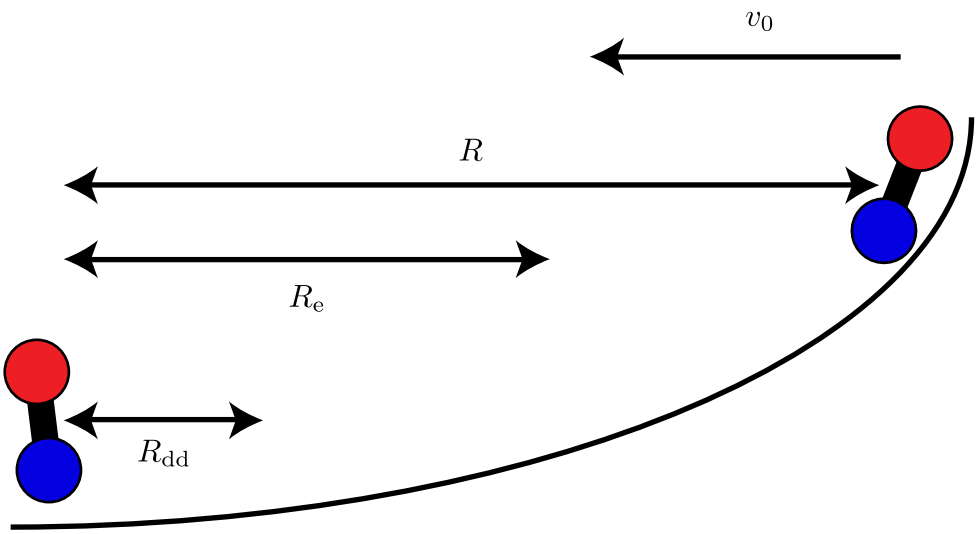

Figure 7.2: A cartoon depicting the process of two molecules now occupying the same optical lattice site and in the process of colliding. Overlaid are the relevant length scales, the characteristic dipole radius, R_{dd}, and the entanglement radius, R_{e}, described in the text.

and the entanglement radius,

$$R_{\mathrm{e}} = \left(\frac{d^2}{8\pi\epsilon_0\epsilon_e}\right)^{1/3}, \tag{7.44}$$

with the energy gap ϵ_e taken to be the minimum energy gap for a given pulse. The dipole radius is the length at which the timescales associated with the dipole-dipole interaction and rotation of the molecules is the same, so that at greater distances the two level approximation is valid. The entanglement radius is the distance at which the dipole-dipole potential energy is the same as the transition between $|e_1e_2\rangle$ and $|g_1g_2\rangle$, so that pairs of molecules closer than this radius will become appreciably entangled in the presence of the strong dressing field [113]. As a concrete example, for KRb ($d = 0.615$ D, $\tilde{B} = B/c = 0.0386$ cm^{-1} [120]) $R_{\mathrm{dd}} \approx 5$ nm and $R_{\mathrm{e}} \approx 127$ nm when the strong dressing field reaches an intensity corresponding to $\Omega_I = 75$. If KRb is confined in an optical lattice created with 1064 nm light with a depth of 40 E_r [25], as described in section 2.4, the width of the initial wave packet would be $\sigma \approx 80$ nm, about 60% of the entanglement radius. It should be noted that the energy gap, ϵ_e, decreases with Ω_I, so that at $\Omega_I = 150$ the entanglement radius increases to $R_{\mathrm{e}} \approx 1089$ nm, increasing even further for more intense fields.

Figure 7.3 demonstrates the result of a simulation of a wave packet representing the relative motion of two KRb molecules separated by $R_0 \approx 550$ nm in an intense pulsed laser field. In this case the wave packet is stationary, *i.e.* the trapping potential has been turned off so that the two dipoles remain stationary, or alternatively it could be viewed as a

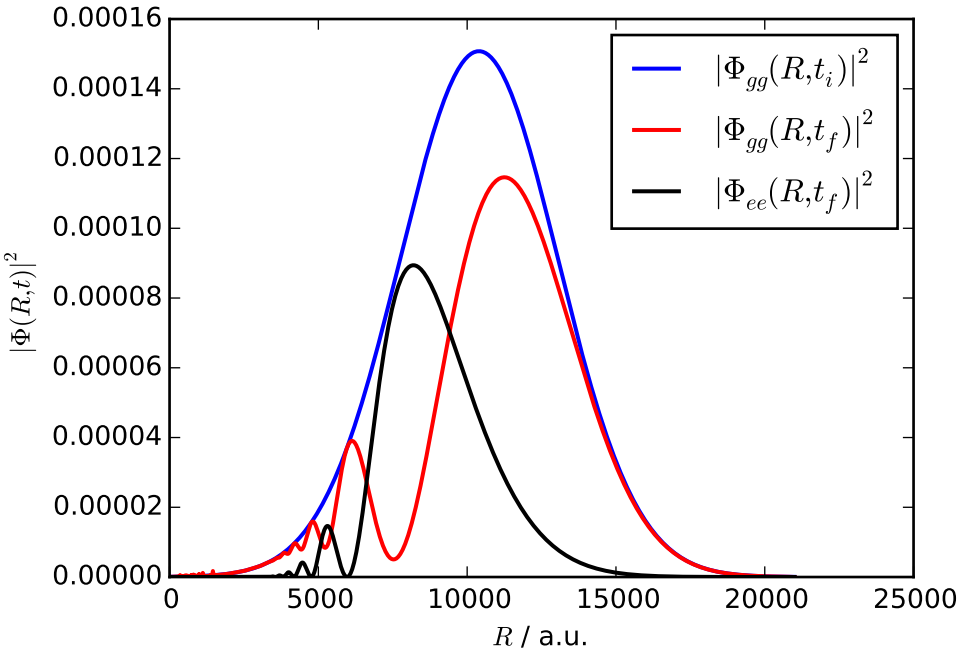

Figure 7.3: Initial and final wave packets in the channels $|g_1g_2\rangle$ and $|e_1e_2\rangle$ for a system of two stationary KRb molecules separated by $R_0 \approx 550$ nm. The initial wave packet is a stationary Gaussian wave packet, $\Phi_{gg}(R, t_i)$, with width of $\sigma \approx 198$ nm. The applied pulse has a Gaussian temporal profile with full width at half maximum of $\tau_{\rm p} = t_{\rm dd} \approx 3.375 \times 10^6\ t_{\rm rotation}$, with a peak intensity corresponding to $\Omega_0 = 180$.

simulation of two dipoles each in the ground state of their own optical lattice sites (neglecting the negligible spread of the initial wave packet over the time scale of the simulation). For KRb with a peak laser intensity corresponding to $\Omega_0 = 180$ the entanglement radius is $R_{\rm e} \approx 1276$ nm, so that the probability of finding the pair of molecules within the entanglement radius $P(R \leq R_{\rm e}) \approx 1$. This simulation performed with a 21000 a_0 spatial grid with 4096 points and the wave packet was propagated through a time of $1.35 \times 10^7\ (2\pi B)^{-1}$ in 1.35×10^7 time steps, taking approximately 120 CPU hours. It is apparent from this that the final wave packet, which was initially a Gaussian wave packet centered at $R_0 \approx 550$ nm with only population in the channel $|g_1g_2\rangle$, has evolved to a state where there is roughly equal population in both channels.

Throughout the course of the simulation the two-body density matrix, after taking the partial trace over the external degrees of freedom, will be of the form

$$\rho(t) = \rho_{aa}(t)|g_1g_2\rangle\langle g_1g_2| + \rho_{bb}(t)|e_1e_2\rangle\langle e_1e_2| + (\rho_{ab}(t)|g_1g_2\rangle\langle e_1e_2| + \text{h.c.})\,, \tag{7.45}$$

where

$$\rho_{aa}(t) = \int_0^\infty dR\, |\Phi_{gg}(R,t)|^2, \tag{7.46}$$

$$\rho_{bb}(t) = \int_0^\infty dR\, |\Phi_{ee}(R,t)|^2, \tag{7.47}$$

$$\rho_{ab}(t) = \int_0^\infty dR\, \Phi_{gg}(R,t)\Phi^*_{ee}(R,t) = \rho^*_{ba}(t). \tag{7.48}$$

Since the goal is to find maximally entangled states, to verify and quantify the degree of entanglement in the rotational degrees of freedom it is necessary to use some measure of the entanglement of the final state of the system, after the entangling pulse has been turned off. One possible measure is the concurrence [121, 122],

$$C(\rho) = \max(0, \lambda_1 - \lambda_2 - \lambda_3 - \lambda_4), \tag{7.49}$$

where $\{\lambda_1, \lambda_2, \lambda_3, \lambda_4\}$ are the square roots of the eigenvalues, in decreasing order, of the matrix $\rho\tilde{\rho}$ with

$$\tilde{\rho} = (\sigma_1^y \sigma_2^y)\rho^*(\sigma_1^y \sigma_2^y). \tag{7.50}$$

This measure has the property that it is 1 for a maximally entangled state, and 0 for a purely mixed state.

In figure 7.3 the concurrence as a function of time is shown for the same system of two static KRb molecules as in figure 7.3 (separation of $R_0 \approx 550$ nm, $\sigma \approx 198$ nm, $\Omega_0 = 180$, and $\tau_{\rm p} = 3.375 \times 10^6\, t_{\rm rotation}$). Plotted on the same axes is the result of a simulation where the two KRb molecules are assumed to be completely localized, which is to say that throughout the entire simulation $\Phi_{gg}(R,t) = a(t)\delta(R - R_0)$ and $\Phi_{ee}(R,t) = b(t)\delta(R - R_0)$. In neither the Gaussian wave packet nor the delta function case is the final concurrence 1, which is not surprising as even without the effect of having a finite width wave packet, the degree of entanglement is sensitive to many factors, including the separation of the molecules, the maximum intensity of the laser pulse, and the duration of the laser pulse. All of these factors impact the resulting asymptotic concurrence in non-trivial ways (for more details, see reference [113]).

The further reduction in concurrence obtained with a finite width initial wave packet relative to the completely localized case results from both the fact that the reduced density matrix, after tracing over R, is no longer a pure state, and from the variation of the dipole-dipole interaction time-scale, $t_{\rm dd}$, with distance. The latter means that portions of the wave packet far from the center, R_0, will experience a pulse with a temporal width either significantly longer or shorter than the local $t_{\rm dd}$. It should be noted that for even a four-fold reduction in the wave packet width results in almost the same behavior as a when the spatial wave function is assumed to be a delta function, making the results of these simulations promising.

Numerically, this problem is quite demanding. The relatively broad width of the initial wave packets, corresponding to an extremely narrow momentum space wave packet, necessitates a fine spatial grid in order to accurately represent the wave packet during propagation.

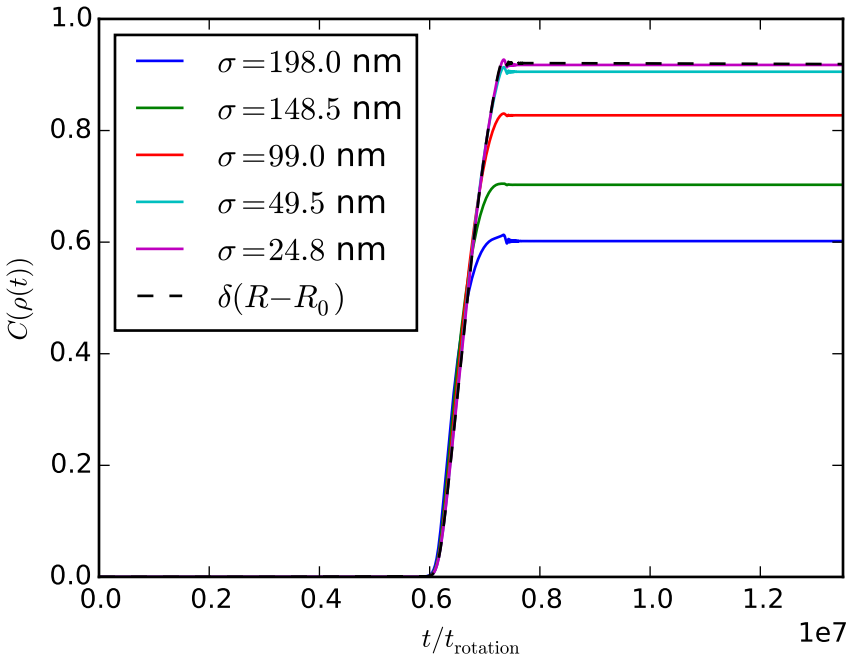

Figure 7.4: Concurrence, eq. (7.49), of the reduced density matrix, eq. (7.45), as a function of time for two KRb molecules in an intense laser field for a variety of initial wave packet widths, σ, from $\sigma = 198.0$ nm down to $\sigma = 24.8$ nm, corresponding to roughly a 64-fold increase in the trapping depth from the broadest wave packet to the narrowest. The simulation parameters, aside from the wave packet width, were the same as those used to generated the data in figure 7.3. The top (dashed) line is a simulation, with the same molecular parameters, using the simplified model of reference [113], which assumes that $\Phi_{gg}(R,t) = a(t)\delta(R - R_0)$ and $\Phi_{ee}(R,t) = b(t)\delta(R - R_0)$ for all time, t.

The distances involved also require quite a large simulation box, so the number spatial grid points required is often quite large, on the order of $N = 10^3$ — 10^5 spatial grid points. In addition, numerical testing suggests that in order to faithfully propagate the wave packet the time steps must also be quite short relative to the pulse duration of the applied dressing field, requiring on the order of $M = 10^6$ — 10^7 time steps. This is quite costly, numerically, as each step requires four discrete Fourier transforms of length N (one forward and one back for both channels) for the free-particle propagation step and N 2×2 matrix-vector multiplications for the potential energy propagation step. For future studies it may be beneficial to adopt more modern methods of wave packet propagation, such as methods involving adaptive grids [123], which do not require the representation of the entire spatial grid for all propagation steps. Such methods could prove useful as the wave packets remain relatively localized throughout the entire propagation meaning that much of the spatial grid, while

required for the fast Fourier transform step, is superfluous.

While it remains to be seen if a process in which molecules collide while interacting in the presence of a strong pulsed laser field can be reliably entangled in a controllable way, the results of this section are encouraging. It appears that for moderate trapping potential depths it is possible to create pairs of entangled molecules even at currently realizable optical lattice spacings, provided it is possible to generate a pulse of the appropriate duration and intensity. This suggests the finite translational width of the states of real molecules confined to optical lattices poses no problem in this respect.

Chapter 8

Conclusion

As has been seen throughout this dissertation, ultracold polar molecules confined to optical lattices can be utilized to study a diverse set of physical phenomena. Such molecules interact with one another at long ranges via the dipole-dipole interaction, which is highly anisotropic and relatively long ranged, compared to the isotropic and short ranged van der Waals interaction which dominates the interactions in comparable ensembles of ultracold atoms confined to optical lattices. The permanent electric dipole moment of polar molecules allows interactions between pairs of molecules to be tuned, in ways which are not possible with ultracold atomic systems, via the application of static and time-varying electric fields [1]. This combination of properties is precisely what makes dipolar molecules a rich target of study.

In chapter 5 it was the anisotropy of the dipole-dipole interaction that made the observation of an order-disorder transition possible in a one dimensional system of dipolar molecules using path integral ground state quantum Monte Carlo (PIGS) simulations. In section 5.2 a straightforward comparison between optical lattice confined polar molecules and the well known quantum rotor model (QRM) was developed. As a consequence of the Mermin-Wagner theorem [67], in one dimensional lattice systems the quantum rotor model is known not to possess an order-disorder quantum phase transition with either nearest neighbor interactions [64] or interactions scaling as $1/r^3$ [65]. The dipole-dipole interaction potential can be seen as an extension of the Heisenberg interaction of the O(3) QRM which breaks the O(3) symmetry possessed by this interaction potential. Because the Mermin-Wagner theorem only applies to low dimensional systems with short ranged interactions and continuous symmetries [67], it is the anisotropy of the dipole-dipole interaction potential, which breaks the continuous O(3) symmetry, that enables the observation of a $T = 0$ K order-disorder quantum phase transition.

The anisotropy of the dipole-dipole potential also played an important role in chapter 6. In section 6.1 two dimensional square lattice systems of polar molecules were studied. In two dimensions the Mermin-Wagner theorem no longer forbids an order-disorder phase transition in systems with continuous symmetries, such as the O(3) QRM [64]. However, the anisotropy of the interaction potential was shown to be important in determining appropriate boundary

conditions for PIGS simulations. The dipole-dipole potential also influenced the types of orderings exhibited by lattice confined polar molecules. Using PIGS simulations, a crossover between an disordered phase and an ordered phase which was characterized by a striped ordering, illustrated in figure 6.1 (bottom left), was found.

In section 6.2, the range of the dipole-dipole interaction, in addition to its anisotropy, was found to influence the behavior of polarized dipolar molecules confined to triangular lattices. In contrast to the case of square lattices, the ordered phase exhibited by dipolar molecules on triangular lattices was found to be characterized by a net polarization in the lattice plane. The discovery of an order-disorder crossover as the strength of the dipole-dipole interaction is increased has potential ramifications for self-assembled crystalline systems of polarized dipolar molecules in two dimensional and quasi-2D geometries [4, 74, 78]. Such systems rely on the application of a strong electric field along the direction perpendicular to the plane of the system to ensure that the dipole-dipole potential is purely repulsive in order to form stable crystals. In section 6.2 it was demonstrated using PIGS simulations that, especially at higher molecular densities, this assumption, *i.e.* that molecular dipoles will be perfectly aligned with a static electric field, is not entirely justified. Self-assembled triangular lattices of dipolar molecules are thus expected to experience instabilities at high densities as the polar molecules will tend to exhibit a net polarization in the lattice plane. In these types of configurations, the dipole-dipole interaction becomes attractive which can lead to collapse [73].

In chapter 7 the tunability of the interactions between polar molecules was the main theme. Through the application of external fields it was demonstrated that models relevant to a condensed matter physics and quantum information processing could be realized. In section 7.1 a potential implementation of Hamiltonian exhibiting topological ordering [99, 100] was described in $^2\Sigma$ ground state polar molecules confined to a Kagome optical lattice and exposed to near-resonant microwave fields [3]. If realized, such a system could potentially be used to implement a quantum memory which is robust to local perturbations [32].

In section 7.2 a theoretical implementation of a model exhibiting novel spectroscopic behavior [105, 106] using polar molecules confined to optical lattices was described. In addition to being of interest for possessing a quantum phase transition, if implemented experimentally, such a system could potentially be used as a sensitive photon detector, detecting light in the microwave regime at very low levels [105]. Once again, the controllability of $^2\Sigma$ ground state dipolar molecules with external fields, this time far off-resonant laser fields and static magnetic fields, is what makes this possible. It was shown that through judicious tuning of the system parameters it should be possible to observe a phase transition between a phase exhibiting linear scaling of the single photon spontaneous emission rate with system size to a phase exhibiting quadratic scaling of the single photon spontaneous emission rate.

Finally, in section 7.3 a method of controllably generating quantum mechanical entanglement of the rotational degrees of freedom in pairs of closed-shell polar molecules [113] was further developed. Here it was shown that pairs of polar molecules, initially confined to optical lattice potentials, could be made to interact in a controllable fashion using intense far off-resonant laser fields. It was found that under realistic conditions, the rotational degrees

of freedom of pairs of molecules could become entangled to an appreciably degree. Since such entanglement can be measured spectroscopically, this has potential applications not only in quantum information, where entanglement is of central importance [124], but could also be used as a test of the foundations of quantum mechanics [113].

8.1 Future directions

There are many open questions left by the work presented in this dissertation. The PIGS simulation method of chapter 3, adapted to sample rotations as well as translations, is quite general, and a natural starting place would be to refine the results of chapters 5 and 6 by including translational degrees of freedom and a realistic trapping potential. Because of the nature of the orderings found, it is highly likely that the phase diagrams of one and two dimensional lattice systems of dipoles will be impacted by including lattice motion in addition to rotation. However, it remains to be seen whether the nature of the phase diagram is fundamentally changed by the inclusion of translations or if the phase diagram remains qualitatively similar to what was found without the inclusion of translations. In any case, further development of the work presented in section 6.3, namely the calculation of high quality interaction potentials and suitable trial wave functions, would facilitate not only more careful calculations of lattice systems but also of homogeneous systems. This has the potential to make connections to current experiments [25, 83] as well as guide further investigations in the field of molecular physics.

Chapter 7 also exposes many interesting research directions. For instance, one natural direction would be to further develop the results of section 7.2 to explore the possibility of developing a photon detector in the microwave regime with single-photon sensitivity. There are a couple of interesting future research questions opened by the results of section 7.3. For one, it remains to be seen what the effect of harmonic motion of the pair of molecules within a single trapping site has on the degree of entanglement generated. Furthermore it would be interesting to explore the application of pulse shaping or coherent control schemes to maximize the degree of entanglement generated through the interaction of a pair of molecules evolving under the influence of an intense laser pulse or pulses. This could be beneficial, especially for wider initial wave packets (corresponding to weaker trapping potentials), which exhibit less asymptotic entanglement than narrower wave packets when illuminated by only a single Gaussian laser pulse. In any case it is clear that there is a lot of potential for ultracold trapped dipolar molecules to be utilized as a platform for quantum information processing and quantum simulation of condensed matter phenomena.

Bibliography

[1] L. Carr, D. DeMille, R. Krems, and J. Ye. "Cold and ultracold molecules: science, technology and applications". *New J. Phys.* **11**, 055049 (2009).

[2] J. Bohn. "Electric Dipoles at Ultralow Temperatures". *Cold Molecules: Theory, Experiment, Applications.* Ed. by R. Krems, W. Stwalley, and B. Friedrich. (CRC Press, Boca Raton, 2009). Chap. 1, 3.

[3] A. Micheli, G. Brennen, and P. Zoller. "A toolbox for lattice-spin models with polar molecules". *Nat. Phys.* **2**, 341 (2006).

[4] H. Büchler, E. Demler, M. Lukin, A. Micheli, N. Prokof'ev, G. Pupillo, and P. Zoller. "Strongly Correlated 2D Quantum Phases with Cold Polar Molecules: Controlling the Shape of the Interaction Potential". *Phys. Rev. Lett.* **98**, 060404 (2007).

[5] M. Tarbutt, B. Sauer, J. Hudson, and E. Hinds. "Design for a fountain of YbF molecules to measure the electron's electric dipole moment". *New J. Phys.* **15**, 053034 (2013).

[6] S. Eckel, P. Hamilton, E. Kirilov, H. Smith, and D. DeMille. "Search for the electron electric dipole moment using Ω-doublet levels in PbO". *Phys. Rev. A* **87**, 052130 (2013).

[7] T. A. Collaboration, J. Baron, W. Campbell, D. DeMille, J. Doyle, G. Gabrielse, V. Gurevich, P. Hess, N. Hutzler, E. Kirilov, I. Kozyryev, B. O'Leary, C. Panda, M. Parsons, E. Petrik, B. Spaun, A. Vutha, and A. West. "Order of Magnitude Smaller Limit on the Electric Dipole Moment of the Electron". *Science* **343**, 269 (2014).

[8] E. Shuman, J. Barry, and D. DeMille. "Laser cooling of a diatomic molecule". *Nature* **467**, 820 (2010).

[9] J. Barry, D. McCarron, E. Norrgard, M. Steinecker, and D. DeMille. "Magneto-optical trapping of a diatomic molecule". *Nature* **512**, 286 (2014).

[10] C. Chin, V. Flambaum, and M. Kozlov. "Ultracold molecules: new probes on the variation of fundamental constants". *New J. Phys.* **11**, 055048 (2009).

[11] M. Kajita. "Sensitive measurements of $m_{\mathrm{p}}/m_{\mathrm{e}}$ variance using vibrational transition frequencies of cold molecules". *New J. Phys.* **11**, 055010 (2009).

[12] K. Góral, L. Santos, and M. Lewenstein. "Quantum Phases of Dipolar Bosons in Optical Lattices". *Phys. Rev. Lett.* **88**, 170406 (2002).

[13] C. Trefzger, M. Alloing, C. Menotti, F. Dubin, and M. Lewenstein. "Quantum magnetism and counterflow supersolidity of up-down bosonic dipoles". *New J. Phys.* **12**, 093008 (2010).

[14] B. Capogrosso-Sansone, C. Trefzger, M. Lewenstein, P. Zoller, and G. Pupillo. "Quantum Phases of Cold Polar Molecules in 2D Optical Lattices". *Phys. Rev. Lett.* **104**, 125301 (2010).

[15] M. Wall and L. Carr. "Hyperfine molecular Hubbard Hamiltonian". *Phys. Rev. A* **82**, 013611 (2010).

[16] J. Pérez-Ríos, F. Herrera, and R. Krems. "External field control of collective spin excitations in an optical lattice of $^2\Sigma$ molecules". *New J. Phys.* **12**, 103007 (2010).

[17] J. Kestner, B. Wang, J. Sau, and S. Sarma. "Prediction of a gapless topological Haldane liquid phase in a one-dimensional cold polar molecule lattice". *Phys. Rev. B* **83**, 174409 (2011).

[18] A. Gorshkov, S. Manmana, G. Chen, J. Ye, E. Demler, M. Lukin, and A. Rey. "Tunable Superfluidity and Quantum Magnetism with Ultracold Polar Molecules". *Phys. Rev. Lett.* **107**, 115301 (2011).

[19] A. Gorshkov, S. Manmana, G. Chen, E. Demler, M. Lukin, and A. Rey. "Quantum magnetism with polar alkali-metal dimers". *Phys. Rev. A* **84**, 033619 (2011).

[20] F. Herrera and R. Krems. "Tunable Holstein model with cold polar molecules". *Phys. Rev. A* **84**, 051401(R) (2011).

[21] D. Peter, S. Müller, S. Wessel, and H. Büchler. "Anomalous Behavior of Spin Systems with Dipolar Interactions". *Phys. Rev. Lett.* **109**, 025303 (2012).

[22] P. Xiang, M. Litinskaya, and R. Krems. "Tunable exciton interactions in optical lattices with polar molecules". *Phys. Rev. A* **85**, 061401(R) (2012).

[23] K. Hazzard, S. Manmana, M. Foss-Feig, and A. Rey. "Far-from-Equilibrium Quantum Magnetism with Ultracold Polar Molecules". *Phys. Rev. Lett.* **110**, 075301 (2013).

[24] S. Manmana, E. Stoudenmire, K. Hazzard, A. Rey, and A. Gorshkov. "Topological phases in ultracold polar-molecule quantum magnets". *Phys. Rev. B* **87**, 081106(R) (2013).

[25] B. Yan, S. Moses, B. Gadway, J. Covey, K. Hazzard, A. Rey, D. Jin, and J. Ye. "Observation of dipolar spin-exchange interactions with lattice-confined polar molecules". *Nature* **501**, 521 (2013).

[26] D. DeMille. "Quantum Computation with Trapped Polar Molecules". *Phys. Rev. Lett.* **88**, 067901 (2002).

[27] Q. Wei, S. Kais, B. Friedrich, and D. Herschbach. "Entanglement of polar molecules in pendular states". *J. Chem. Phys.* **134**, 124107 (2011).

[28] E. Kuznetsova, S. Rittenhouse, H. Sadeghpour, and S. Yelin. "Rydberg atom mediated polar molecule interactions: a tool for molecular-state conditional quantum gates and individual addressability". *Phys. Chem. Chem. Phys.* **13**, 17115 (2011).

[29] E. Kuznetsova, T. Bragdon, R. Côté, and S. Yelin. "Cluster-state generation using van der Waals and dipole-dipole interactions in optical lattices". *Phys. Rev. A* **85**, 012328 (2012).

[30] J. Zhu, S. Kais, Q. Wei, D. Herschbach, and B. Friedrich. "Implementation of quantum logic gates using polar molecules in pendular states". *J. Chem. Phys.* **138**, 024104 (2013).

[31] F. Herrera, Y. Cao, S. Kais, and K. Whaley. "Infrared-dressed entanglement of cold open-shell polar molecules for universal matchgate quantum computing". *New J. Phys.* **16**, 075001 (2014).

[32] C. Nayak, S. Simon, A. Stern, M. Freedman, and S. Sarma. "Non-Abelian anyons and topological quantum computation". *Rev. Mod. Phys.* **80**, 1083 (2008).

[33] A. Bijl. "The lowest wave function of the symmetrical many particles system". *Physica* **7**, 869 (1940).

[34] R. Feynman. "Atomic Theory of the Two-Fluid Model of Liquid Helium". *Phys. Rev.* **94**, 262 (1954).

[35] E. Merzbacher. *Quantum Mechanics*. 3rd Ed. (Wiley, New York, 1998).

[36] R. Zare. *Angular Momentum: Understanding Spatial Aspects in Chemistry and Physics*. (Wiley-Interscience, New York, 1988).

[37] H. Lefebvre-Brion and R. Field. *The Spectra and Dynamics of Diatomic Molecules*. (Elsevier, San Diego, 2004).

[38] B. Sussman. "Five ways to the nonresonant dynamic Stark effect". *Am. J. Phys.* **79**, 477 (2011).

[39] I. Bloch. "Ultracold quantum gases in optical lattices". *Nat. Phys.* **1**, 23 (2005).

[40] A. Sarsa, K. Schmidt, and W. Magro. "A path integral ground state method". *J. Chem. Phys.* **113**, 1366 (2000).

[41] M. Rossi, M. Nava, L. Reatto, and D. Galli. "Exact ground state Monte Carlo method for Bosons without importance sampling". *J. Chem. Phys.* **131**, 154108 (2009).

[42] A. Macia, D. Hufnagl, F. Mazzanti, J. Boronat, and R. Zillich. "Excitations and Stripe Phase Formation in a Two-Dimensional Dipolar Bose Gas with Tilted Polarization". *Phys. Rev. Lett.* **109**, 235307 (2012).

[43] A. Macia, J. Boronat, and F. Mazzanti. "Phase diagram of dipolar bosons in 2D with tilted polarization", arXiv:1407.6960v1 [cond–mat.quant–gas] (2014).

[44] P. Cazzato, S. Paolini, S. Moroni, and S. Baroni. "Rotational dynamics of CO solvated in small He clusters: A quantum Monte Carlo study". *J. Chem. Phys.* **120**, 9071 (2004).

[45] F. Paesani, R. Zillich, and K. Whaley. "OCS in small para-hydrogen clusters: Energetics and structure with N=1–8 complexed hydrogen molecules". *J. Chem. Phys.* **119**, 11682 (2003).

[46] R. Zillich and K. Whaley. "Solvation Structure and Rotational Dynamics of LiH in ^{4}He Clusters". *J. Phys. Chem. A* **111**, 7489 (2007).

[47] D. Ceperley. "Path integrals in the theory of condensed helium". *Rev. Mod. Phys.* **67**, 279 (1995).

[48] M. Boninsegni, N. Prokof'ev, and B. Svistunov. "Worm Algorithm for Continuous-Space Path Integral Monte Carlo Simulations". *Phys. Rev. Lett.* **96**, 070601 (2006).

[49] M. Boninsegni, N. Prokof'ev, and B. Svistunov. "Worm algorithm and diagrammatic Monte Carlo: A new approach to continuous-space path integral Monte Carlo simulations". *Phys. Rev. E* **74**, 036701 (2006).

[50] N. Metropolis, A. Rosenbluth, M. Rosenbluth, A. Teller, and E. Teller. "Equation of State Calculations by Fast Computing Machines". *J. Chem. Phys.* **21**, 1087 (1953).

[51] S. Chib and E. Greenberg. "Understanding the Metropolis-Hastings Algorithm". *Am. Stat.* **49**, 327 (1995).

[52] V. Amebaokar and M. Troyer. "Estimating errors reliably in Monte Carlo simulations of the Ehrenfest model". *Am. J. Phys.* **78**, 150 (2010).

[53] D. Frenkel and B. Smit. *Understanding Molecular Simulation.* (Academic Press, San Diego, 2002).

[54] D. Benoit and D. Clary. "Quaternion formulation of diffusion quantum Monte Carlo for the rotation of rigid molecules in clusters". *J. Chem. Phys.* **113**, 5193 (2000).

[55] R. Zillich, J. Mayrhofer, and S. Chin. "Extrapolated high-order propagators for path integral Monte Carlo simulations". *J. Chem. Phys.* **132**, 044103 (2010).

[56] M. Suzuki. "Hybrid exponential product formulas for unbounded operators with possible applications to Monte Carlo simulations". *Phys. Lett. A* **201**, 425 (1995).

[57] S. Chin. "Symplectic integrators from composite operator factorizations". *Phys. Lett. A* **226**, 344 (1997).

[58] R. Feynman, A. Hibbs, and D. Styer. *Quantum Mechanics and Path Integrals.* Emended Edition. (Dover Publications Inc., Mineola, 2005).

[59] D. Marx and M. Müser. "Path integral simulations of rotors: theory and applications". *J. Phys.: Condens. Matter* **11**, R117 (1999).

[60] F. Byron Jr. and R. Fuller. *Mathematics of Classical and Quantum Physics.* (Dover Publications Inc., New York, 1992).

[61] E. Weisstein. *CRC Concise Encyclopedia of Mathematics*. 2nd ed. (CRC Press, Boca Raton, 2002).

[62] J.-P. Hansen and I. McDonald. *Theory of Simple Liquids*. 3rd Ed. (Academic Press, London, 2006).

[63] B. Abolins, R. Zillich, and K. Whaley. "A Ground State Monte Carlo Approach for Studies of Dipolar Systems with Rotational Degrees of Freedom". *J. Low Temp. Phys.* **165**, 249 (2011).

[64] S. Sachdev. *Quantum Phase Transitions*. (Cambridge University Press, New York, 1999).

[65] A. Dutta and J. Bhattacharjee. "Phase transitions in the quantum Ising and rotor models with a long-range interaction". *Phys. Rev. B* **64**, 184106 (2001).

[66] M. Suzuki. "Relationship between d-Dimensional Quantal Spin Systems and $(d+1)$-Dimensional Ising Systems". *Prog. Theor. Phys.* **56**, 1454 (1976).

[67] N. Mermin and H. Wagner. "Absence of Ferromagnetism or Antiferromagnetism in One- or Two-Dimensional Isotropic Heisenberg Models". *Phys. Rev. Lett.* **17**, 1133 (1966).

[68] D. Chandler. *Introduction to Modern Statistical Mechanics*. (Oxford University Press, New York, 1987).

[69] L. Wasserman. *All of Statistics: A Concise Course in Statistical Inference*. (Springer, New York, 2004).

[70] R. Honerjäger and R. Tischer. "High temperature-microwave spectrometer for Zeeman-effect measurements involving diamagnetic molecules". *Z. Naturforsch.* **28a**, 458 (1973).

[71] T. Story Jr. and A. Hebert. "Dipole moments of KI, RbBr, RbI, CsBr, and CsI by the electric deflection method". *J. Chem. Phys.* **64**, 855 (1976).

[72] M. Gullans, T. Tiecke, D. Chang, J. Feist, J. Thompson, J. Cirac, P. Zoller, and M. Lukin. "Nanoplasmonic Lattices for Ultracold Atoms". *Phys. Rev. Lett.* **109**, 235309 (2012).

[73] S. Ronen, D. Bortolotti, and J. Bohn. "Radial and Angular Rotons in Trapped Dipolar Gases". *Phys. Rev. Lett.* **98**, 030406 (2007).

[74] G. Astrakharchik, J. Boronat, I. Kurbakov, and Y. Lozovik. "Quantum Phase Transition in a Two-Dimensional System of Dipoles". *Phys. Rev. Lett.* **98**, 060405 (2007).

[75] D. Hufnagl, E. Krotscheck, and R. Zillich. "Polarized Dipolar Bose Gas with Strong Interactions". *J. Low Temp. Phys.* **158**, 85 (2010).

[76] A. Golomedov, G. Astrakharchik, and Y. Lozovik. "Mesoscopic supersolid of dipoles in a trap". *Phys. Rev. A* **84**, 033615 (2011).

[77] P. Jain, F. Cinti, and M. Boninsegni. "Structure, Bose-Einstein condensation, and superfluidity of two-dimensional confined dipolar assemblies". *Phys. Rev. B* **84**, 014534 (2011).

[78] M. Boninsegni. "Mesoscopic dipolar quantum crystals". *Phys. Rev. A* **87**, 063604 (2013).

[79] F. Mazzanti, R. Zillich, G. Astrakharchik, and J. Boronat. "Dynamics of a Two-Dimensional System of Quantum Dipoles". *Phys. Rev. Lett.* **102**, 110405 (2009).

[80] L. Pollet, J. Picon, H. Büchler, and M. Troyer. "Supersolid Phase with Cold Polar Molecules on a Triangular Lattice". *Phys. Rev. Lett.* **104**, 125302 (2010).

[81] D. Yamamoto, I. Danshita, and C. Sá de Melo. "Dipolar bosons in triangular optical lattices: Quantum phase transitions and anomalous hysteresis". *Phys. Rev. A* **85**, 021601(R) (2012).

[82] J.-J. Weis. "Simulation of quasi-two-dimensional dipolar systems". *J. Phys.: Condens. Matter* **15**, S1471 (2003).

[83] K.-K. Ni, S. Ospelkaus, M. de Miranda, A. Pe'er, B. Neyenhuis, J. Zirbel, S. Kotochigova, P. Julienne, D. Jin, and J. Ye. "A High Phase-Space-Density Gas of Polar Molecules". *Science* **322**, 231 (2008).

[84] W. McMillan. "Ground State of Liquid He^4". *Phys. Rev.* **138**, A442 (1965).

[85] J. Cuervo and P.-N. Roy. "Path integral ground state study of finite-size systems: Application to small $(\text{parahydrogen})_N$ ($N = 2$ — 20) clusters". *J. Chem. Phys.* **125**, 124314 (2006).

[86] R. Ahlrichs, R. Penco, and G. Scoles. "Intermolecular Forces in Simple Systems". *Chem. Phys.* **19**, 119 (1977).

[87] S. Boys and F. Bernardi. "The calculation of small molecular interactions by the differences of separate total energies. Some procedures with reduced errors". *Mol. Phys.* **19**, 553 (1970).

[88] J. Turney, A. Simmonett, R. Parrish, E. Hohenstein, F. Evangelista, J. Fermann, B. Mintz, L. Burns, J. Wilke, M. Abrams, N. Russ, M. Leininger, C. Janssen, E. Seidl, W. Allen, H. Schaefer, R. King, E. Valeev, C. Sherrill, and T. Crawford. "Psi4: an open-source ab initio electronic structure program". *Wiley Interdisciplinary Reviews: Computational Molecular Science* **2**, 556 (2012).

[89] K. Raghavachari, G. Trucks, J. Pople, and M. Head-Gordon. "A fifth-order perturbation comparison of electron correlation theories". *Chem. Phys. Lett.* **157**, 479 (1989).

[90] T. Dunning Jr. "Gaussian basis sets for use in correlated molecular calculations. I. The atoms boron through neon and hydrogen". *J. Chem. Phys.* **90**, 1007 (1989).

[91] D. Woon and T. Dunning Jr. "Gaussian basis sets for use in correlated molecular calculations. V. Corevalence basis sets for boron through neon". *J. Chem. Phys.* **103**, 4572 (1995).

[92] L. Janssen, G. Groenenboom, and A. van der Avoird. "*Ab initio* potential energy surfaces for NH($^3\Sigma^-$)–NH($^3\Sigma^-$) with analytical long range". *J. Chem. Phys.* **131**, 224314 (2009).

[93] T. Ho and H. Rabitz. "A general method for constructing multidimensional molecular potential energy surfaces from *ab initio* calculations". *J. Chem. Phys.* **104**, 2584 (1996).

[94] A. van der Avoird, P. Wormer, F. Mulder, and R. Berns. "Ab initio studies of the interactions in Van der Waals molecules". *Top. Curr. Chem.* **93**, 1 (1980).

[95] M. Baranov, M. Dalmonte, G. Pupillo, and P. Zoller. "Condensed Matter Theory of Dipolar Quantum Gases". *Chem. Rev.* **112**, 5012 (2012).

[96] G. Brennen, A. Micheli, and P. Zoller. "Designing spin-1 lattice models using polar molecules". *New J. Phys.* **9**, 138 (2007).

[97] F. Herrera, M. Litinskaya, and R. Krems. "Tunable disorder in a crystal of cold polar molecules". *Phys. Rev. A* **82**, 033428 (2010).

[98] R. Moessner and S. Sondhi. "Resonating Valence Bond Phase in the Triangular Lattice Quantum Dimer Model". *Phys. Rev. Lett.* **86**, 1881 (2001).

[99] M. Freedman, C. Nayak, and K. Shtengel. "Non-Abelian topological phases in an extended Hubbard model", arXiv:cond–mat/0309120v2 [cond–mat.str–el] (2003).

[100] M. Freedman, C. Nayak, and K. Shtengel. "Extended Hubbard Model with Ring Exchange: A Route to a Non-Abelian Topological Phase". *Phys. Rev. Lett.* **94**, 066401 (2005).

[101] G.-B. Jo, J. Guzman, C. Thomas, P. Hosur, A. Vishwanath, and D. Stamper-Kurn. "Ultracold Atoms in a Tunable Optical Kagome Lattice". *Phys. Rev. Lett.* **108**, 045305 (2012).

[102] J. Korsbakken. *Private correspondence*. 2008.

[103] S. V. Alyabyshev. *Private correspondence*. 2012.

[104] L. Ioffe, M. Feigel'man, A. Ioselevich, D. Ivanov, M. Troyer, and G. Blatter. "Topologically protected quantum bits using Josephson junction arrays". *Nature* **415**, 503 (2002).

[105] A. Kocherzhenko, J. Dawlaty, B. Abolins, F. Herrera, D. Abraham, and K. Whaley. "Collective effects in linear spectroscopy of dipole-coupled molecular arrays". *Phys. Rev. A* **90**, 062502 (2014).

[106] J. Krugler, M. C.G., and H. McConnell. "Collective Electronic States in Molecular Crystals". *J. Chem. Phys.* **41**, 2421 (1964).

[107] L. Bakalis and J. Knoester. "Optical properties of one-dimensional exciton systems: Beyond the Heitler-London approximation". *J. Chem. Phys.* **106**, 6964 (1997).

[108] W. Zemke and W. Stwalley. "Radiative transition probabilities, lifetimes, and dipole moments for all vibrational levels in the $X\,^1\Sigma^+$ state of ^{7}LiH". *J. Chem. Phys.* **73**, 5584 (1980).

[109] P. Dagdigian, H. Cruse, and R. Zare. "Radiative lifetimes of the alkaline earth monohalides". *J. Chem. Phys.* **60**, 2330 (1974).

[110] X.-L. Deng, D. Porras, and J. Cirac. "Effective spin quantum phases in systems of trapped ions". *Phys. Rev. A* **72**, 063407 (2005).

[111] R. Islam, E. Edwards, K. Kim, S. Korenblit, C. Noh, H. Carmichael, G.-D. Lin, L.-M. Duan, C.-C. Wang, J. Freericks, and C. Monroe. "Onset of a quantum phase transition with a trapped ion quantum simulator". *Nat. Commun.* **2**, 377 (2011).

[112] T. Wilk, A. Gaëtan, C. Evellin, J. Wolters, Y. Miroshnychenko, P. Grangier, and A. Browaeys. "Entanglement of Two Individual Neutral Atoms Using Rydberg Blockade". *Phys. Rev. Lett.* **104**, 010502 (2010).

[113] F. Herrera, S. Kais, and K. Whaley. "Entanglement creation in cold molecular gases using strong laser pulses", arXiv:1302.6444 [physics.atom–ph] (2013).

[114] N. Brunner, D. Cavalcanti, S. Pironio, V. Scarani, and S. Wehner. "Bell nonlocality". *Rev. Mod. Phys.* **86**, 419 (2014).

[115] J. Sebby-Strabley, M. Anderlini, P. Jessen, and J. Porto. "Lattice of double wells for manipulating pairs of cold atoms". *Phys. Rev. A* **73**, 033605 (2006).

[116] A. Couvert, T. Kawalec, G. Reinaudi, and D. Guéry-Odelin. "Optimal transport of ultracold atoms in the non-adiabatic regime". *EPL* **83**, 13001 (2008).

[117] B. Garraway and K.-A. Suominen. "Wave-packet dynamics: new physics and chemistry in femto-time". *Rep. Prog. Phys.* **58**, 365 (1995).

[118] G. Billing and K. Mikkelsen. *Advanced Molecular Dynamics and Chemical Kinetics.* (Wiley-Interscience, New York, 1997).

[119] J. Huyghebaert and H. De Raedt. "Product formula methods for time-dependent Schrödinger problems". *J. Phys. A: Math. Gen.* **23**, 5777 (1990).

[120] J. Deiglmayr, M. Aymar, R. Wester, M. Weidemüller, and O. Dulieu. "Calculations of static dipole polarizabilities of alkali dimers: Prospects for alignment of ultracold molecules". *J. Chem. Phys.* **129**, 064309 (2008).

[121] W. Wootters. "Entanglement of Formation of an Arbitrary State of Two Qubits". *Phys. Rev. Lett.* **80**, 2245 (1998).

[122] R. Horodecki, P. Horodecki, M. Horodecki, and K. Horodecki. "Quantum entanglement". *Rev. Mod. Phys.* **81**, 865 (2009).

[123] K. Hughes and R. Wyatt. "Wavepacket dynamics on arbitrary Lagrangian-Eulerian grids: Application to an Eckart barrier". *Phys. Chem. Chem. Phys.* **5**, 3905 (2003).

[124] M. Nielsen and I. Chuang. *Quantum Computation and Quantum Information*. (Cambridge University Press, New York, 2000).